A Nested-LES Approach for Computation of High-Reynolds Number, Equilibrium and Non-Equilibrium Turbulent Wall-Bounded Flows

by

Yifeng Tang

A dissertation submitted in partial fulfillment
of the requirements for the degree of
Doctor of Philosophy
(Mechanical Engineering)
in the University of Michigan
2016

Doctoral Committee:

Associate Professor Rayhaneh Akhavan, Chair
Professor John P. Boyd
Professor David R. Dowling
Professor Gregory M. Hulbert

TABLE OF CONTENTS

LIST OF FIGURES iv

LIST OF TABLES x

ABSTRACT xi

CHAPTER

I. Introduction 1

1.1 Existing LES Wall-Modelling Approaches 2
1.1.1 Off-wall Boundary Conditions 2
1.1.2 Alternative, Simplified Dynamical Equations 3
1.1.3 Multi-Domain Approaches 6
1.2 Objectives of the Present Study 7

II. The Nested-LES Approach 9

2.1 Overview 9
2.2 Implementation 11
2.3 Computational Savings 15

III. Application to Equilibrium and Non-equilibrium Turbulent Channel Flows 18

3.1 Numerical Methods 18
3.1.1 Spatial Discretization 19
3.1.2 Temporal Discretization 21
3.1.3 Internal Interface Boundary Conditions 22
3.1.4 Direct Solver 23
3.1.5 Iterative Solver 25
3.2 Subgrid-scale Model 27
3.3 Simulation Parameters 29

IV. Results in Equilibrium Turbulent Channel Flow 38

4.1 Mean statistics 38
4.2 High-order moments 41
4.3 Two-point Statistics 43
4.4 Effect of z^* 47
4.5 Renormalization functions 47
4.6 Comparison to non-nested LES 49

V. Results in Non-Equilibrium, Strained Turbulent Channel Flow 75

5.1 Evolution of Skin-friction Coefficients 76
5.2 Evolution of Turbulence Statistics in the Straining Zone . . . 78
5.3 Evolution of Turbulence Statistics in the Recovery Zone . . . 79
5.4 Renormalization Factors in Nested-LES 82

VI. Summary and Conclusions 99

VII. Future Work 102

APPENDICES 104
A.1 Overview 106
A.2 1D Energy Spectra in Wall-Bounded Turbulence 107
A.2.1 Universal Representation of the 1D Energy Spectra 107
A.2.2 An Analytical Formulation for the 1D Energy Spectra 110
A.3 Filtered 1D Energy Spectra in Wall-Bounded Turbulence . . . 113
A.3.1 An Analytical Formulation for the Filtered 1D Energy Spectra 113
A.3.2 Evaluation of C_K, α_1, and ϵ_α in LES 118
A.4 Application to Filtered DNS and LES Databases 121
A.4.1 Application to a Filtered DNS Database 121
A.4.2 Results in LES Database 123
A.5 Summary 125

BIBLIOGRAPHY 143

LIST OF FIGURES

Figure

3.1 The computational domain and coordinate system used in nested-LES of equilibrium and non-equilibrium turbulent channel flow. . . 35

3.2 The wall-normal grid distribution in the patching collocation spectral domain-decomposition method used in both the full domain and minimal flow unit of nested-LES. 36

3.3 Schematic of experimental setup of shear-driven, three-dimensional turbulent boundary layer of *Driver and Hebbar* (1987, 1991) and schematic of simulations of non-equilibrium, strained turbulent channel flow. 37

4.1 Profiles of mean velocity, turbulence intensities, and Reynolds shear stresses predicted by nested-LES in equilibrium turbulent channel flow at $Re_\tau \approx 1000$, compared to DNS data. 53

4.2 Profiles of mean velocity, turbulence intensities, and Reynolds shear stresses predicted by nested-LES in equilibrium turbulent channel flow at $Re_\tau \approx 2000$, compared to DNS data. 54

4.3 Profiles of mean velocity, turbulence intensities, and Reynolds shear stresses predicted by nested-LES in equilibrium turbulent channel flow at $Re_\tau \approx 5000$, compared to DNS, LES and experimental data. 55

4.4 Profiles of mean velocity, turbulence intensities, and Reynolds shear stresses predicted by nested-LES in equilibrium turbulent channel flow at $Re_\tau \approx 10000$, compared to DNS and experimental data. . . . 56

4.5 Moments of order $2p$ of streamwise velocity fluctuations, and coefficients A_p in the logarithmic law for moments as a function of the moment order $2p$, predicted by nested-LES at $1000 \leq Re_\tau \leq 10000$. 57

4.6 Skewness of streamwise, spanwise, and wall-normal velocity fluctuations as functions of z^+ and z/h. 58

4.7 Flatness of streamwise, spanwise, and wall-normal velocity fluctuations as functions of z^+ and z/h. 59

4.8 Streamwise and spanwise sections of the correlation maps predicted by nested-LES in equilibrium turbulent channel flow at $1000 \leq Re_\tau \leq 10000$ at $z/h = 0.1$. 60

4.9 Streamwise and spanwise sections of the correlation maps predicted by nested-LES in equilibrium turbulent channel flow at $1000 \leq Re_\tau \leq 10000$ at $z/h = 0.6$. 61

4.10 Inclination angles predicted by nested-LES in equilibrium turbulent channel flow at $1000 \leq Re_\tau \leq 10000$, compared to DNS data at $Re_\tau \approx 950$. 62

4.11 One-dimensional two-point correlations predicted by nested-LES in equilibrium turbulent channel flow at $1000 \leq Re_\tau \leq 10000$ in the outer region and the near-wall region. 63

4.12 Integral scales as a function z/h predicted by nested-LES in equilibrium turbulent channel flow at $1000 \leq Re_\tau \leq 10000$. 64

4.13 Profiles of mean velocity, turbulence intensities, and Reynolds shear stresses predicted by nested-LES in equilibrium turbulent channel flow at $Re_\tau \approx 2000$ with z^* placed at $0.025 \leq z^*/h \leq 0.20$. 65

4.14 Streamwise and spanwise sections of the correlation maps at $z/h = 0.1$ predicted by nested-LES in equilibrium turbulent channel flow at $Re_\tau \approx 2000$ with z^* placed at $z^*/h = 0.025$, 0.04, 0.05, and 0.07. . . 66

4.15 Streamwise and spanwise sections of the correlation maps at $z/h = 0.6$ predicted by nested-LES in equilibrium turbulent channel flow at $Re_\tau \approx 2000$ with z^* placed at $z^*/h = 0.025$, 0.04, 0.05, and 0.07. . . 67

4.16 Time-history of the renormalization functions from nested-LES in equilibrium turbulent channel flow at $Re_\tau \approx 1000$. 68

4.17 Time-history of the renormalization functions from nested-LES in equilibrium turbulent channel flow at $Re_\tau \approx 2000$. 69

4.18 Time-history of the renormalization functions from nested-LES in equilibrium turbulent channel flow at $Re_\tau \approx 5000$. 70

4.19 Time-history of the renormalization functions from nested-LES in equilibrium turbulent channel flow at $Re_\tau \approx 10000$. 71

4.20 Time-averaged renormalization functions, deviation from unity, and standard deviations in time from nested-LES in equilibrium turbulent channel flow at $Re_\tau \approx 1000$ and 2000. 72

4.21 Time-averaged renormalization functions, deviation from unity, and standard deviations in time from nested-LES in equilibrium turbulent channel flow at $Re_\tau \approx 5000$ and 10000. 73

4.22 Profiles of mean velocity, turbulence intensities, and Reynolds shear stresses predicted by nested-LES and non-nested LES in equilibrium turbulent channel flow at $Re_\tau \approx 2000$. 74

5.1 Evolution of streamwise and spanwise skin-friction coefficients, and surface-flow angle predicted by nested-LES and non-nested LES in non-equilibrium, strained turbulent channel flow. 83

5.2 Profiles of mean velocities and turbulent stresses near the end of the straining zone predicted by nested-LES in non-equilibrium, strained turbulent channel flow, compared to experimental measurements in shear-driven, three-dimensional TBL at $x^* = t^* \approx -10.9$. 84

5.3 Profiles of mean velocities and turbulent stresses near the end of the straining zone predicted by nested-LES in non-equilibrium, strained turbulent channel flow, compared to experimental measurements in shear-driven, three-dimensional TBL at $x^* = t^* \approx -5.4$. 85

5.4 Profiles of mean velocities and turbulent stresses near the end of the straining zone predicted by nested-LES in non-equilibrium, strained turbulent channel flow, compared to experimental measurements in shear-driven, three-dimensional TBL at $x^* = t^* \approx -0.11$. 86

5.5 Hodograph of the mean streamwise and spanwise velocities near the end of the straining zone predicted by nested-LES and non-nested LES. 87

5.6 Profiles of mean velocities and turbulent stresses in the initial recovery zone predicted by nested-LES in non-equilibrium, strained turbulent channel flow, compared to experimental measurements in shear-driven, three-dimensional TBL at $x^* = t^* \approx 0.11$. 88

5.7 Profiles of mean velocities and turbulent stresses in the initial recovery zone predicted by nested-LES in non-equilibrium, strained turbulent channel flow, compared to experimental measurements in shear-driven, three-dimensional TBL at $x^* = t^* \approx 0.23$. 89

5.8 Profiles of mean velocities and turbulent stresses in the initial recovery zone predicted by nested-LES in non-equilibrium, strained turbulent channel flow, compared to experimental measurements in shear-driven, three-dimensional TBL at $x^* = t^* \approx 0.45$. 90

5.9 Profiles of mean velocities and turbulent stresses in the mid-recovery zone predicted by nested-LES in non-equilibrium, strained turbulent channel flow, compared to experimental measurements in shear-driven, three-dimensional TBL at $x^* = t^* \approx 0.91$. 91

5.10 Profiles of mean velocities and turbulent stresses in the mid-recovery zone predicted by nested-LES in non-equilibrium, strained turbulent channel flow, compared to experimental measurements in shear-driven, three-dimensional TBL at $x^* = t^* \approx 1.81$. 92

5.11 Profiles of mean velocities and turbulent stresses in the mid-recovery zone predicted by nested-LES in non-equilibrium, strained turbulent channel flow, compared to experimental measurements in shear-driven, three-dimensional TBL at $x^* = t^* \approx 3.6$. 93

5.12 Profiles of mean velocities and turbulent stresses in the final recovery zone predicted by nested-LES in non-equilibrium, strained turbulent channel flow, compared to experimental measurements in shear-driven, three-dimensional TBL at $x^* = t^* \approx 5.4$. 94

5.13 Profiles of mean velocities and turbulent stresses in the final recovery zone predicted by nested-LES in non-equilibrium, strained turbulent channel flow, compared to experimental measurements in shear-driven, three-dimensional TBL at $x^* = t^* \approx 10.9$. 95

5.14 Profiles of mean velocities and turbulent stresses in the final recovery zone predicted by nested-LES in non-equilibrium, strained turbulent channel flow, compared to experimental measurements in shear-driven, three-dimensional TBL at $x^* = t^* \approx 16.3$. 96

5.15 Time-history of the renormalization functions from nested-LES in non-equilibrium, strained turbulent channel flow. 97

5.16 Time-averaged renormalization functions, deviation from unity, and standard deviations in time from nested-LES in non-equilibrium, strained turbulent channel flow in the straining zone and the recovery zone. 98

A.1 Normalized one-dimensional energy spectra, $\tilde{E}^{1D}(\tilde{k}_\alpha)$, in the streamwise and spanwise directions as a function of the normalized wavenumber, $\tilde{k}_\alpha$, from DNS of turbulent channel flow in the outer region and the near-wall region. 130

A.2 Profiles of $\langle\epsilon\rangle^+$ and $\langle 3\epsilon_\alpha\rangle^+$ from DNS of turbulent channel flow at $180 \leq Re_\tau \leq 950$. 131

A.3 Normalized one-dimensional energy spectra, $\hat{E}^{1D}(\hat{k}_\alpha)$, in the streamwise and spanwise directions as a function of the normalized wavenumber, $\hat{k}_\alpha$, from DNS of turbulent channel flow in the outer region and the near-wall region. 132

A.4 Model parameters C_K and α_1 for Pao's and Meyers & Meneveau's spectra obtained from DNS databases of turbulent channel flow with $180 \leq Re_\tau \leq 2000$ as a function of z^+ and z/h. 133

A.5 Geometric interpretation of the relation between 3D spectrum and 1D spectrum. 134

A.6 Effect of spectral cut-off filter in the $\hat{k}_\beta$-direction on the spectral energy contained in the 1D spectrum in the $\hat{k}_\alpha$ direction. 135

A.7 Partitioning of the spectral space when the flow field is filtered and the effect of filtering on the 1D energy spectrum. 136

A.8 Profiles of $\langle 3\epsilon_\alpha\rangle/\langle\epsilon\rangle$ as a function of z^+ and z/h, and centerline values of $\langle 3\epsilon_\alpha\rangle/\langle\epsilon\rangle$ as a function of Re_τ. 137

A.9 Modelled filtered 1D energy spectra, compared to filtered DNS spectra in turbulent channel flow in the outer region and the near-wall region. 138

A.10 Total recovered SGS TKE and its breakdown in regions B_x, B_y, and C_{xy}, compared to exact values from DNS of turbulent channel flow at $Re_\tau \approx 550$. 139

A.11 Profiles of RANS turbulence intensities recovered from filtered DNS database of turbulent channel flow at $Re_\tau \approx 550$, compared to full DNS statistics. 140

A.12 Profiles of mean velocity, filtered turbulence intensities, and recovered turbulence intensities from LES of turbulent channel flow at $Re_\tau \approx 550$ and 1000, compared to DNS at $Re_\tau \approx 550$ and 950. 141

A.13 Modelled filtered 1D energy spectra from LES of turbulent channel flow at $Re_\tau \approx 550$ and $Re_\tau \approx 1000$ extended into subgrid scales, compared to filtered DNS. 142

LIST OF TABLES

Table

3.1 Computational domain sizes, grid resolutions, grid spacings and mapping parameters employed in nested-LES and non-nested LES of equilibrium and non-equilibrium turbulent channel flow in the present study. 33

3.2 Wall-normal grid distribution employed in nested-LES and non-nested LES of equilibrium and non-equilibrium turbulent channel flow at $Re_\tau \approx 1000$, 2000, 5000, and 10000 at 'standard' resolution. 34

4.1 The skin friction coefficients predicted in nested-LES and non-nested LES of equilibrium turbulent channel flow compared to Dean's correlation. 51

4.2 The skin friction coefficient predicted in nested-LES of equilibrium turbulent channel flow at $Re_\tau \approx 2000$ with different locations of z^*/h. 52

A.1 Model parameters C_K and α_1 for Pao's and Meyers & Meneveau's spectra as a function of z^+. 127

A.2 Model parameters C_K and α_1 for Pao's and Meyers & Meneveau's spectra as a function of z/h. 128

A.3 Universal profiles of $\langle 3\epsilon_\alpha \rangle / \langle \epsilon \rangle$ in the inner layer, as a function of z^+. 129

ABSTRACT

A Nested-LES Approach for Computation of High-Reynolds Number, Equilibrium and Non-Equilibrium Turbulent Wall-Bounded Flows

by

Yifeng Tang

Chair: Rayhaneh Akhavan

Computation of high Reynolds number, complex, non-equilibrium wall-bounded turbulent flows presents a major challenge for large-eddy simulation (LES), due to the stringent resolution requirements in the near-wall region in conventional LES, and the inability of existing wall models to accurately capture the near-wall dynamics in flows involving complex physics in the near-wall region. In this study, a novel nested-LES approach for computation of high Reynolds number, equilibrium and non-equilibrium, wall-bounded turbulent flows is proposed. The method couples well-resolved LES in a minimal flow unit with coarse-resolution LES in the full domain to provide high-fidelity simulations of the flow physics in both the inner and outer layers. The coupling between the two domains of nested-LES is achieved by dynamically renormalizing the velocity fields in each domain at each time-step during the course of the simulation to match the wall-normal profiles of the single-time ensemble-averaged kinetic energies of the components of mean and fluctuating velocities in both domains to those of the minimal flow unit in the inner layer, and to those of the full domain in the outer

layer. The proposed nested-LES approach can be applied to any flows with at least one direction of local or global homogeneity, while reducing the required number of grid points from $O(Re_\tau^2)$ of conventional LES to $O(\log Re_\tau)$ and $O(Re_\tau^1)$ in flows with two or one directions of homogeneity, respectively.

The proposed nested-LES approach has been applied to LES of equilibrium turbulent channel flow at $Re_\tau \approx 1000$, 2000, 5000, and 10000, and non-equilibrium, strained turbulent channel flow at $Re_\tau \approx 2000$. All the simulations were performed in full domains of size $L_x \times L_y \times L_z = 2\pi h \times \pi h \times 2h$ with minimal flow units of size $l_x^+ \approx 3200 - 3900$, $l_y^+ \approx 1600 - 1950$ wall units, and $l_z = 2h$, and employed grid resolutions of $64 \times 64 \times 17/33/17$ in both the full domain and the minimal flow unit, independent of Reynolds number. In application to equilibrium turbulent channel flow, the nested-LES approach predicts the skin-friction coefficient, first-order turbulence statistics, higher-order moments, two-point correlations, correlation maps, and structural features of the flow in agreement with available direct numerical simulation (DNS) and experimental data. In application to non-equilibrium, strained turbulent channel flow, nested-LES predicts the evolution of skin-friction coefficients and one-point turbulence statistics in good agreement with experimental data in shear-driven, three-dimensional turbulent boundary-layer (TBL). The performance of the nested-LES approach is rooted in the ideas of energy cascade, which forms the basis of nested-LES. These principles result in correction of the turbulence kinetic energy (TKE) for all components of velocity in nested-LES, while retaining the inherent non-linear dynamics of turbulence.

CHAPTER I

Introduction

Large eddy simulation (LES) is a method for predicting turbulent flows based on direct computation of the large, energy-containing scales of motion and modelling of the effects of small scales on the resolved scales. With the growth of computer power, LES has attracted greater interest and effort from both the commercial CFD industry and scientific research community, and the recent years have witnessed many advances in LES techniques (*Sagaut and Deck*, 2009; *Georgiadis et al.*, 2010). Nevertheless, computation of high Reynolds number, complex, wall-bounded turbulent flows continues to remain a challenge for LES. The bottleneck arises from the stringent resolution requirements of LES in the near-wall region, where the energy-containing eddies have a size proportional to their distance from the wall. Resolving these eddies in LES requires $O(Re_x^{1.8})$ grid points in turbulent boundary layers (*Chapman*, 1979) or $O(Re_\tau^2)$ grid points in general wall-bounded flows (*Jimenez*, 2003), where $Re_\tau \equiv u_\tau \delta/\nu$ denotes the friction Reynolds number with u_τ denoting the friction velocity, δ denoting the boundary layer thickness, channel half-height, or pipe radius, and ν denoting the kinematic viscosity. These grid point requirements are not that different from the $O(Re_\tau^{9/4})$ grid points required in direct numerical simulation (DNS) (*Jimenez*, 2003), and make the computation of high Reynolds number turbulent wall-bounded flows typical of engineering applications prohibitive.

The purpose of the present study is to develop an approach to address the issue of high resolution requirement of the near-wall region in LES. To this end, a nested-LES approach is proposed and its performance in equilibrium turbulent channel flow and non-equilibrium, strained turbulent channel flow is evaluated.

1.1 Existing LES Wall-Modelling Approaches

A number of wall-modelling approaches have been proposed over the years to bypass the stringent resolution requirements of LES in the near-wall region. These approaches can be classified into three categories: approaches based on formulation of off-wall boundary conditions, those based on numerical solution of alternative, simplified dynamical equations in the inner layer, and those based on multi-domain techniques.

1.1.1 Off-wall Boundary Conditions

In the first category, a set of approximate boundary conditions is specified at the first grid point away from the wall. In earlier studies, these approximate boundary conditions were derived from simple algebraic equations which satisfy the law-of-the-wall. *Deardorff* (1970) and *Schumann* (1975) applied the equilibrium law-of-wall to generate the velocity and shear-stresses, respectively, at the first off-wall grid point. *Mason and Callen* (1986) required the local, instantaneous velocity filed at the first off-wall grid pint to satisfy the equilibrium law-of-the-wall. *Piomelli et al.* (1989) proposed a tunable expression for the shear stresses in addition to the equilibrium law-of-the-wall, to represent the sweep-ejection events near the wall. All these early studies, rely on the assumption of equilibrium law-of-the-wall, and as such give poor results in non-equilibrium flow conditions, such as separated flow downstream of a backward-facing step, separated flow downstream of two-dimensional bump, and flat-

plate boundary layer forced by oscillating pressure gradient (*Piomelli and Balaras*, 2002; *Piomelli et al.*, 2007; *Piomelli*, 2008).

In attempts to get away from the assumption of equilibrium law-of-the-wall, *Hoffmann and Benocci* (1995) integrated the boundary layer equations in the near-wall region and proposed a simplified formulation that contains the unsteady and pressure gradient terms, but applied it only to equilibrium turbulent channel flow. *Chung and Pullin* (2009) and *Inoue and Pullin* (2011) proposed an approximate off-wall boundary condition model under the framework of stretched-vortex subgrid-scale model and explicitly accounts for the pressure-induced non-equilibrium effects. However, this method prescribes zero values for the spanwise and wall-normal instantaneous velocities at the first off-wall grid point, which precludes its application in complex flow conditions.

More recently, based on recent experimental observation on the inner-outer layer interactions, *Mathis et al.* (2011) and *Mathis et al.* (2013) proposed a wall model based on the empirical correlations between the fluctuating velocities in the inner and outer layers, or the interaction between the fluctuating velocities in the outer layer and the shear stresses in the inner layer. These models based on inner-outer layer interactions have been applied to reconstruct inner-layer statistics from experimental measurements in the outer layer, while their applicability as LES wall-modelling approach is yet to be demonstrated.

1.1.2 Alternative, Simplified Dynamical Equations

In the second category of existing wall-modelling approaches, the flow in the inner layer is computed using simplified, less-expensive, dynamical equations, and the solution is matched to the LES solution away from the wall. Commonly used examples of such equations are thin boundary layer Reynolds-Averaged Navier–Stokes

(RANS) equations, unsteady RANS equations, and certain lower-order forms of LES equations.

Methods which use RANS equations as the alternative dynamical equations, known as 'hybrid RANS/LES methods', are mainly motivated by the superior performance of LES in complex flow conditions and the low cost of RANS in the near-wall region. In hybrid RANS/LES methods, the RANS equation is solved either on a pre-defined near-wall mesh, called 'zonal RANS/LES method' (*Balaras et al.*, 1996; *Cabot and Moin*, 1999; *Wang and Moin*, 2002; *Temmerman et al.*, 2005; *Hamba*, 2006; *Frohlich and von Terzi*, 2008), or on the same mesh for LES together with certain criteria to transition between RANS and LES, which includes Detached-Eddy Simulation (DES) *Spalart et al.* (1997) and Scale-Adaptive Simulation (SAS) (*Menter et al.*, 2003).

Despite its recent popularity, the hybrid RANS/LES methods often face the difficulty of exchanging information between two solutions with disparate spectral content, such as RANS and LES (*Sagaut and Deck*, 2009). One well-known manifestation of this difficulty is the 'logarithmic layer mismatch' observed in many RANS/LES based models in equilibrium wall flows. Attempts have been made to remedy this problem by introducing stochastic forcing near the interface (*Keating and Piomelli*, 2006; *Menter et al.*, 2010b), but so far little improvement has been observed using this technique (*Piomelli et al.*, 2007; *Menter et al.*, 2010b) and the physical significance of such artificial forcing cannot be clearly justified. One curious observation in application of the hybrid RANS/LES method is that the aforementioned RANS/LES interface mismatch could be partially compensated when the near-wall region experiences non-equilibrium effects, which is believed to generate unsteady information in the RANS region and lead to better development of LES contents near the RANS/LES interface (*Radhakrishnan et al.*, 2006). This 'fortunate accident' reflects both the need of further theoretical justification of the present hybrid RANS/LES methods and the

incompatibility between the RANS and the LES methodology.

DES proposed by *Spalart et al.* (1997) applies RANS in the attached boundary layer and LES in the massively separated region, and switches between RANS and LES formulation based on the distance from the wall-boundary and local grid sizes. DES has been performed with reasonable computational load for complex engineering problems, but it consistently exhibits mismatch of the mean velocity profiles between the RANS region and the LES region (*Spalart*, 2009). The mismatch leads to large errors in the skin-friction coefficient, the magnitude of which, interestingly, increases as the near-wall mesh is refined enough for LES mode to be turned on near the wall. A more recent, revised version of DES, named Delayed Detached-Eddy Simulation (DDES) (*Spalart et al.*, 2006), aims at delaying the transition to LES in presence of fine mesh near the wall, but the solution can be non-unique and branch into either LES-like or RANS-like depending on the initial flow condition (*Spalart*, 2009).

SAS (*Menter et al.*, 2003; *Menter and Egorov*, 2005) behaves similar to DES in many situations, while the transition between LES and RANS modes is based on local turbulence kinetic energy and length scales. SAS has been applied to a wide range of test cases and has obtained reasonable results with manageable computational cost (*Egorov et al.*, 2010). One major weakness of SAS at this stage, however, is that the model tends to be too dissipative and behaves overly RANS-like when the flow is moderately unstable. For equilibrium flows, for example two-dimensional (2D) channels, SAS fails to produce unsteady structures and yields only steady-state RANS solution (*Menter et al.*, 2003, 2010a; *Menter and Egorov*, 2010).

Besides the RANS equations, simulations of simplified one-dimensional turbulence equations have been used in the so-called 'Two Level Simulations' (TLS) to compute the small scales on a refined 1D grid embedded inside the LES grid in the near wall region (*Kemenov and Menon*, 2003; *Gungor and Menon*, 2006, 2010). Although TLS

predicts the mean velocity and rms velocity fluctuations reasonably well in equilibrium turbulent channel flow, it has been found to predict inaccurate energy spectra in turbulent channel flow and over-predict the mean velocity by nearly 40% in simulations of flow over a hill (*Gungor and Menon*, 2006, 2010).

1.1.3 Multi-Domain Approaches

In the third category of existing wall-modelling approaches, the same set of LES equations are solved in the inner and outer layers, but the computational domain is structured with different sizes and/or resolutions in the inner and outer layers to reduce the computational load. The multi-domain approaches can be divided into two types.

The first type, known as grid-embedding methods, solves LES equation in the near-wall region on a refined mesh and obtains cost-savings from alleviating the resolution requirement in the outer region. A number of different formulations of this approach have been proposed with different numerical methods (*Kallinderis*, 1992; *Kravchenko et al.*, 1996; *Kang*, 1996; *Shariff and Moser*, 1998; *Blackburn and Schmidt*, 2003). However, in all of these methods, the resolution requirements in the inner layer still scale as $O(Re_\tau^2)$, which prohibits the application of such methods to to high Reynolds number flows.

In the second type of multi-domain methods, the well-resolved near-wall domain spans only part of the full domain, and cost-savings are achieved by computing the near-wall region in a smaller domain (*Pascarelli et al.*, 2000; *Haliloglu*, 2007). This approach, by explicitly computing much of the near-wall physics, has the potential of favorable performance in complex flow conditions. However, in the approaches adopted to date, the off-wall boundary conditions for the outer-layer domain produced by the near-wall domain lack the information on the large-scale motions and

can introduce artificial periodicity into the outer layer. In the present approach, which also employs a well-resolved domain for the near-wall region, we resolve this shortcoming by coupling the smaller, well-resolved domain for the near-wall region with the coarse, full domain for the outer layer only through the single-time-averaged turbulence statistics of the two domains, thus allowing the outer, large structures to be preserved in the full domain.

1.2 Objectives of the Present Study

The objective of the present study is to develop a new wall-modelling approach for overcoming the high resolution requirements of LES in the inner layer, while retaining in the accuracy of well-resolved LES in both the inner and outer layers. To this end, a nested-LES approach is proposed. In this approach, two simultaneous, nested, large eddy simulations are performed; one in the full computational domain at coarse resolution, the other in a minimal flow unit at fine resolution. The LES solution in the minimal flow unit is used to dynamically 'correct' the full-domain LES in the inner layer, while the LES solution in the full domain is used to dynamically 'correct' the minimal-flow-unit LES in the outer layer. The method can be applied to any flows with at least one direction of 'global' or 'local' homogeneity, and retains the accuracy of well-resolved LES in both the near-wall and outer regions, while reducing the required number of grid points from $O(Re_\tau^2)$ of conventional LES to $O(\log Re_\tau)$ or $O(Re_\tau)$ in flows with two or one locally or globally homogeneous directions, respectively.

The organization of the dissertation is as follows. In Chapter II, the nested-LES approach is detailed, and the computational savings offered by nested-LES are discussed. Chapter III reviews the subgrid-scale model, the numerical methods, and simulation parameters, employed in the present study. In Chapter IV, the perfor-

mance of nested-LES approach in equilibrium turbulent channel flow at $Re_\tau \approx 1000$, 2000, 5000, and 10000 is discussed. In Chapter V, the performance of nested-LES is assessed in non-equilibrium, strained turbulent channel flow at $Re_\tau \approx 2000$. A summary and conclusions are given in Chapter VI. Recommendations for future work are presented in Chapter VII.

CHAPTER II

The Nested-LES Approach

2.1 Overview

It has been recognized, since the pioneering work of *Townsend* (1958, 1976), that two classes of organized structures play a role in the dynamics of wall turbulence: small-scale, near-wall structures, whose size scales with the inner length scale, ν/u_τ; and large-scale, outer-layer structures, whose size scales with the outer length scale, δ. Earlier studies considered the outer-layer structures to be passive, with no substantial influence on the near-wall dynamics (*Robinson*, 1991). This view has been challenged by more recent studies, which have shown an active role for both classes of structures (*Guala et al.*, 2006; *Adrian*, 2007; *Balakumar and Adrian*, 2007), as well as a strong coupling between the two (*Marusic et al.*, 2010a; *Smits et al.*, 2011). The outer-layer structures have been shown to strongly influence both the fluctuating velocity and pressure fields in the near-wall region (*Hoyas and Jimenez*, 2006; *Hutchins and Marusic*, 2007a,b; *Jimenez and Hoyas*, 2008; *Mathis et al.*, 2009), and the Reynolds and wall shear stresses (*Hutchins and Marusic*, 2007a; *Marusic and Heuer*, 2007). These interactions have been shown to become more pronounced as the Reynolds number increases (*Marusic et al.*, 2010a; *Smits et al.*, 2011). More recently, it has been proposed that the influence of large-scale structures on the near-wall structures

is in the form of an amplitude modulation (*Talluru et al.*, 2014). These results all point to a strong coupling between the near-wall and outer-layer structures.

From an LES standpoint, the turbulence dynamics in the outer layer can be computed using LES with a coarse-resolution, Reynolds-number-independent grid. This grid, however, becomes inadequate in the inner layer. The approach adopted in the present study to overcome this limitation is to perform two nested large eddy simulations: one in the full domain at coarse resolution, and the other in a minimal flow unit at fine resolution. The LES solution in the well-resolved minimal flow unit is then used to dynamically 'correct' the coarse-resolution, full-domain LES solution in the inner layer. A minimal flow unit is known to accurately predict the normalized turbulence statistics in the inner layer (*Jimenez and Moin*, 1991; *Jimenez and Pinelli*, 1999; *Flores and Jimenez*, 2010). However, it cannot accurately predict the wall-shear stresses in the absence of proper outer-layer structures (*Flores and Jimenez*, 2010; *Hwang*, 2013). To remedy this problem, the outer-layer solution in the minimal flow unit also needs to be 'corrected' based on the solution in the full-domain LES. Thus, a two-way coupling between the two domains is required, in which the LES solution in the minimal flow unit is used to dynamically 'correct' the full-domain LES in the inner layer, while the LES solution in the full domain is used to dynamically 'correct' the minimal-flow-unit LES in the outer layer.

In the nested-LES approach, this 'correction' and coupling between the two domains is achieved by renormalizing the instantaneous LES velocity fields in both domains dynamically during the course of the simulation to match the wall-normal profiles of single-time, ensemble-averaged kinetic energies of components of the 'mean' and fluctuating velocities in both domains to those of the minimal flow unit in the inner layer, and to those of the full domain in the outer layer. It will be shown in Sections 4.5–4.6 that this simple renormalization is sufficient to correct the wall-shear

stresses in both domains, thus leading to accurate turbulence statistics.

Given the construction of the nested-LES approach, application of the method requires flows which are 'locally' or 'globally' homogeneous in at least one wall-parallel direction. A wide variety of practical as well as canonical laboratory flows, including separating turbulent boundary layer, flow around any two-dimensional object, and flow in the mid-section of an airplane wing, fall within such a classification, and can be handled with nested-LES with significant computational savings compared to conventional LES, as discussed in Section 2.3.

2.2 Implementation

The nested-LES approach is based on the solution of LES equations at coarse resolution in the full domain, coupled with well-resolved LES in a minimal flow unit. For incompressible flow, the LES equations are given by (*Sagaut*, 2006)

$$\frac{\partial \overline{u}_i}{\partial t} + \frac{\partial}{\partial x_j}(\overline{u}_i \overline{u}_j) = -\frac{1}{\rho}\frac{\partial \overline{p}}{\partial x_i} + \nu \frac{\partial^2 \overline{u}_i}{\partial x_j^2} - \frac{\partial \tau_{ij}}{\partial x_j}; \quad \frac{\partial \overline{u}_i}{\partial x_i} = 0, \tag{2.1}$$

where the overbar denotes a filtering operation which removes the small (subgrid) scales, $\overline{u}_i$ is the velocity field resolved in LES, $\overline{p}$ is the resolved pressure field, ρ is the density, and $\tau_{ij} = \overline{u_i u_j} - \overline{u}_i \overline{u}_j$ is the subgrid-scale (SGS) stress tensor.

Let $\overline{u}_{\alpha,\mathscr{D}}(\boldsymbol{x}, t)$ denote the LES velocity fields in the full domain and minimal flow unit of nested-LES at the conclusion of time-step t, with $\mathscr{D} = \mathscr{F}$ denoting the full domain and $\mathscr{D} = \mathscr{M}$ denoting the minimal flow unit. The key to the nested-LES approach is a renormalization procedure in between time-steps t and $t + dt$, in which the velocity fields, $\overline{u}_{\alpha,\mathscr{D}}(\boldsymbol{x}, t)$, in both domains are 'renormalized' to $\overline{u}^R_{\alpha,\mathscr{D}}(\boldsymbol{x}, t)$. The LES solution at $t + dt$ in each domain is then advanced using $\overline{u}^R_{\alpha,\mathscr{D}}(\boldsymbol{x}, t)$ instead of $\overline{u}_{\alpha,\mathscr{D}}(\boldsymbol{x}, t)$. To construct the renormalized velocity fields, $\overline{u}^R_{\alpha,\mathscr{D}}(\boldsymbol{x}, t)$, the velocity fields,

$\overline{u}_{\alpha,\mathscr{D}}(\boldsymbol{x},t)$, in each domain are decomposed as

$$\overline{u}_{\alpha,\mathscr{D}}(\boldsymbol{x},t) = \langle\langle \overline{u}_{\alpha,\mathscr{D}}(\boldsymbol{x},t)\rangle\rangle + \overline{u}''_{\alpha,\mathscr{D}}(\boldsymbol{x},t), \tag{2.2}$$

where $\langle\langle\ \rangle\rangle$ denotes a single-time, ensemble-average over the 'locally' or 'globally' homogeneous (or nearly homogeneous) wall-parallel flow direction or directions, and $\langle\langle \overline{u}_{\alpha,\mathscr{D}}(\boldsymbol{x},t)\rangle\rangle$ and $\overline{u}''_{\alpha,\mathscr{D}}(\boldsymbol{x},t)$ are the single-time 'mean' and fluctuating parts of the velocity field, respectively. The renormalized velocity fields, $\overline{u}^R_{\alpha,\mathscr{D}}(\boldsymbol{x},t)$, in each domain are then defined as

$$\overline{u}^R_{\alpha,\mathscr{D}}(\boldsymbol{x},t) = \langle\langle \overline{u}_{\alpha,\mathscr{D}}(\boldsymbol{x},t)\rangle\rangle\ R(\langle\langle \overline{u}_{\alpha,\mathscr{D}}\rangle\rangle\langle\langle \overline{u}_{\alpha,\mathscr{D}}\rangle\rangle) + \overline{u}''_{\alpha,\mathscr{D}}(\boldsymbol{x},t)\ R(\langle\langle \overline{u}''_{\alpha,\mathscr{D}}\overline{u}''_{\alpha,\mathscr{D}}\rangle\rangle), \tag{2.3}$$

where $R(\phi_{\alpha,\mathscr{D}})$ are renormalization functions, given by

$$R(\phi_{\alpha,\mathscr{D}}) = \ (\phi_{\alpha,\mathscr{M}}/\phi_{\alpha,\mathscr{D}})^{1/2} \quad , \ \text{at } z \leq z^*, \tag{2.4a}$$

$$R(\phi_{\alpha,\mathscr{D}}) = \ (\phi_{\alpha,\mathscr{F}}/\phi_{\alpha,\mathscr{D}})^{1/2} \quad , \ \text{at } z > z^*, \tag{2.4b}$$

where $\phi_{\alpha,\mathscr{D}}$ can denote $\langle\langle \overline{u}_{\alpha,\mathscr{D}}\rangle\rangle\langle\langle \overline{u}_{\alpha,\mathscr{D}}\rangle\rangle$ or $\langle\langle \overline{u}''_{\alpha,\mathscr{D}}\overline{u}''_{\alpha,\mathscr{D}}\rangle\rangle$, with no summation implied over the index α, and z^* is the wall-normal position at which the basis for renormalization of the velocity fields is switched from the LES solution in the minimal flow unit at $z \leq z^*$ to the LES solution in the full domain at $z > z^*$.

The renormalization procedure described by equations (2.2)–(2.4) rescales the velocity fields in the full domain and the minimal flow unit to match the wall-normal profiles of the single-time ensemble-averaged kinetic energies of the components of the 'mean' velocity, $\langle\langle \overline{u}_\alpha\rangle\rangle\langle\langle \overline{u}_\alpha\rangle\rangle$, and fluctuating velocity, $\langle\langle \overline{u}''_\alpha\overline{u}''_\alpha\rangle\rangle$, in both domains to those of the minimal flow unit in the inner layer, $z \leq z^*$, and to those of the full domain in the outer layer, $z > z^*$.

The fundamental principle behind the renormalization procedures of equations (2.2)–(2.4) are the ideas of energy cascade. At $z > z^*$, the minimal flow unit is not large enough to accommodate the large-scale, outer-layer turbulence structures. If it did, however, the amount of turbulence kinetic energy (TKE) in each component of the fluctuating velocity which would cascade down to the scales that are contained within the minimal flow unit would be the energy that exists in the corresponding fluctuating velocity component in the large domain. This implies that for $z > z^*$, the magnitude of $\langle\langle \overline{u}''_\alpha \overline{u}''_\alpha \rangle\rangle$ in the minimal flow unit should be dictated by that in the full domain for each velocity component, α. In these arguments, the viscous dissipation of TKE in the energy containing and equilibrium-range eddies in both domains has been neglected, and it is assumed that the largest scales of the minimal flow unit fall somewhere within the universal equilibrium range. Similarly, for $z < z^*$, where the full domain does not have sufficient resolution to resolve the near-wall eddies, the proper amount of energy $\langle\langle \overline{u}''_\alpha \overline{u}''_\alpha \rangle\rangle$ which should reside in each component of TKE in the full domain is that which exists in the corresponding α component of the fluctuating velocity in the minimal flow unit. For the above arguments to be valid, both domains need to have the same mean velocity profiles and wall shear stresses. This is ensured by equating of the kinetic energies of the components of the mean velocity, $\langle\langle \overline{u}_\alpha \rangle\rangle \langle\langle \overline{u}_\alpha \rangle\rangle$, in both domains to that of the full domain for $z > z^*$ and to that of the minimal-flow-unit for $z \leq z^*$.

While the renormalization procedures of equations (2.2)–(2.4) are designed to correct only the turbulence kinetic energy in each domain, in practice this simple renormalization procedure is found to correctly predict not only the flow statistics up to second order, but also higher order turbulence statistics and structural features. These results are discussed in further detail in Sections 4.1–4.3.

The location z^* in equation (2.4) represents the wall-normal position at which

the basis for renormalization of the velocity fields is switched from the LES solution in the minimal flow unit at $z \leq z^*$ to the LES solution in the full domain at $z > z^*$. The value of z^* is chosen to place z^* in the overlap region between the inner layer, $z/\delta < 0.1$ (*Pope*, 2000, Table 7.1), and outer layer, $z^+ > 50$ (*Pope*, 2000, Table 7.1), where superscript $^+$ denotes normalization using the wall-friction velocity, u_τ, and kinematic viscosity, ν. Accordingly, a value of $z^*/\delta = 0.05$ has been used in all the simulations reported in this study. However, the results were found to be fairly insensitive to the exact choice of z^* for $0.04 \leq z^*/\delta \leq 0.06$. A detailed discussion of the effect of z^* on the predictions of nested-LES is given in Section 4.4.

In practice (see Sections 4.5 and 5.4), the renormalization functions, $R(\phi_{\alpha,\mathscr{D}})$, remain fairly close to unity throughout the cross-section of the channel, and confined to 1 ± 0.001 for $0.05 \leq z/\delta < 1$. With a choice of $z^*/\delta = 0.05$ and these values of $R(\phi_{\alpha,\mathscr{D}})$, no significant jump discontinuity occurs at $z = z^*$ when the solution in each domain is switched from its original velocity field, $\overline{u}_{\alpha,\mathscr{D}}(\boldsymbol{x}, t)$, to the renormalized velocity field, $\overline{u}^R_{\alpha,\mathscr{D}}(\boldsymbol{x}, t)$. One can also introduce a blending zone, in which the renormalized and original velocity fields in each domain are gradually blended together. However, we found no particular advantage to introducing such a blending zone, and adopted the simpler approach of switching between the renormalized and original velocity fields at z^*.

After application of the renormalization procedure equations (2.2)–(2.4), the velocity fields, $\overline{u}^R_{\alpha,\mathscr{D}}(\boldsymbol{x}, t)$, are no longer divergence-free. However, one should note that $\overline{u}^R_{\alpha,\mathscr{D}}(\boldsymbol{x}, t)$ represent only intermediate velocity fields in between time-steps. By the end of each time-step, the velocity field in each domain is once again projected onto the divergence-free space as part of the solution for that time-step. These divergence-free velocity fields no longer have identical turbulence statistics in the two domains, with the difference between the two sets of statistics being equal to the values of

$R(\phi_{\alpha,\mathscr{D}})$ which need to be applied at the next time-step. All the turbulence statistics reported in this study were obtained from the divergence-free velocity fields at the conclusion of each time-step in the full domain.

2.3 Computational Savings

In nested-LES approach, a full domain of any desired size in outer scaling is employed The minimal flow unit is of a fixed size in inner scaling (wall units) in the homogeneous (or nearly homogeneous), wall-parallel, flow direction(s), but is of the same size as the full domain in the inhomogeneous flow direction(s). In the homogeneous (or nearly homogeneous), wall-parallel, flow direction(s), a grid spacing of fixed size in outer scaling is employed in the full domain, while a grid spacing of fixed size in inner scaling is employed in the minimal flow unit. This makes the required number of grid points in the homogeneous (or nearly homogeneous) flow direction(s) independent of Reynolds number in both domains.

The required grid spacing in the wall-normal (z) direction needs to have a size proportional to the distance from the wall in the inner layer ($z/\delta < 0.1$), to properly capture the dynamics of the turbulence structures, whose size grows proportional to the distance from the wall in this region (see Figure 4.12). Thus, the required number of wall-normal grid-points in a slab of thickness dz is given by $dN_z \sim dz/z$. In the outer layer ($z/\delta > 0.1$), where the size of the turbulence structures becomes nearly fixed in outer scaling (see Figure 4.12), a wall-normal grid spacing of fixed size in outer scaling can be employed.

With such a grid distribution, the total required number of grid points in a slab of thickness dz in flows with two homogeneous (or nearly homogeneous) directions is given by $dN_{tot} \sim (N_x \cdot N_y) \cdot dN_z \sim (N_x \cdot N_y) \cdot dz/z$ (*Jimenez*, 2003), where $N_x \cdot N_y$ is the required number of grid points in the homogeneous flow directions, which is

independent of the Reynolds number. Thus, the total number of required grid points in the whole domain grows with the Reynolds number as

$$N_{tot} \sim \int_{z_0}^{0.1\delta} dz/z \sim \log(\delta/z_0) \sim \log(\delta^+/z_0^+) \sim \log(Re_\tau), \tag{2.5}$$

where z_0 is a wall-normal location of a fixed distance in wall units from the wall. Consequently, in flows with two homogeneous (or nearly homogeneous) directions, the total required number of grid points grows with the Reynolds number as $O(\log Re_\tau)$.

In flows with only one homogeneous (or nearly homogeneous) direction (such as flow in a separating turbulent boundary layer, flow in a channel expansion, flow around any two-dimensional object, or flow in the mid-section of an airplane wing), the minimal flow unit needs to span the full length of the computational domain in the inhomogeneous wall-parallel direction, but can remain 'minimal' in the homogeneous (or nearly homogeneous) flow direction. For such flows, the required number of grid points in a slab of thickness dz is given by $dN_{tot} \sim N_y \cdot C\delta/z \cdot dz/z$ (*Jimenez*, 2003), where N_y is number of grid points in the homogeneous (or nearly homogeneous) flow direction, and is independent of the Reynolds number, $C\delta$ is the size of the domain in the inhomogeneous, wall-parallel (x), flow direction, and a grid-spacing in the x-direction proportional to the size of the turbulent eddies, which are themselves proportional to z, is assumed. As such, the total number of required grid points grows with the Reynolds number as

$$N_{tot} \sim \int_{z_0}^{0.1\delta} C\delta \; dz/z^2 \sim (\delta/z_0) \sim (\delta^+/z_0^+) \sim Re_\tau \; , \tag{2.6}$$

in any given geometry. While the $O(Re_\tau)$ grid-point requirement flows with only one direction of homogeneity is larger than $O(\log Re_\tau)$ of flows with two homogeneous

directions, it is still a significant savings compared to $O(Re_\tau^2)$ grid point requirement of conventional LES.

In more general flows, the nested-LES approach may still be applied to regions of local homogeneity (or near homogeneity) in the flow, to offer significant computational savings compared to conventional LES. In these cases, multiple minimal flow units may be introduced to represent a local ensemble of the near-wall dynamics in different regions of the full domain. Applying the same analysis above, the number of required grid points still remains $O(\log Re_\tau)$ and $O(Re_\tau)$ in regions with two or one locally homogeneous directions, respectively.

The overhead associated with the renormalization step of nested-LES is minimal, rendering the cost of nested-LES no different from the cost of non-nested LES in each of the full domain and minimal flow unit of nested-LES. These features give nested-LES the ability to provide high-fidelity predictions in a wide range of wall flows, while reducing the required number of grid points from $O(Re_\tau^2)$ of conventional LES to $O(\log Re_\tau)$ to $O(Re_\tau)$ in flows with two or one locally or globally homogeneous (or nearly homogeneous) directions.

CHAPTER III

Application to Equilibrium and Non-equilibrium Turbulent Channel Flows

In this study, we apply the nested-LES approach to compute equilibrium turbulent channel flows at $Re_\tau \approx 1000$, 2000, 5000, and 10000, and non-equilibrium, strained turbulent channel flow at $Re_\tau \approx 2000$. A schematic of the channels and the coordinate system is shown in Figures 3.1 and 3.3. Note that no specific positioning of the minimal flow unit relative to the full domain is required in the nested-LES approach, as the two domains are coupled only through their single-time-averaged turbulence statistics. This chapter describes the numerical methods, simulation parameters, and choice of SGS model employed in the present study.

3.1 Numerical Methods

The LES equations (2.1) are solved in both the full domain and the minimal flow unit using a patching collocation spectral domain-decomposition method (*Orszag*, 1980; *Kang*, 1996; *Canuto et al.*, 2007; *Haliloglu*, 2007). The computational box spans the full height of the channel, from one wall to the other, in both the full domain and the minimal flow unit, and is partitioned into three non-overlapping sub-domains Ω_s ($s = 1, 2, 3$) in the wall-normal direction, as shown in Figure 3.2. This partitioning

allows the grid-point distribution in each zone to be customized to minimize the required number of grid points in the wall-normal direction. This section describes the details of the spatial and temporal discretization, internal boundary conditions, and solvers employed in the present study.

3.1.1 Spatial Discretization

The velocity field, $\overline{u}_{i,s}$, in each sub-domain is represented in terms of Fourier series in the homogeneous streamwise (x) and spanwise (y) directions and mapped Chebyshev polynomials in the wall-normal (z) direction as (*Orszag*, 1980; *Canuto et al.*, 2007)

$$\overline{u}_{i,s}(x,y,z,t) = \sum_{|m|\leq M_s/2} \sum_{|n|\leq N_s/2} v_{i,s}(m,n,z,t) \exp[i\alpha m x + i\beta n y], \tag{3.1}$$

where $\alpha = 2\pi L_x$, $\beta = 2\pi L_y$,

$$v_{i,s}(m,n,z,t) = \sum_{p=0}^{P_s} \hat{v}_{i,s}(m,n,p,t) T_p(\xi_s), \tag{3.2}$$

and T_p represents the Chebyshev polynomial.

The same internal interface locations and wall-normal distribution of grid points were employed in the full domain and the minimal flow unit at each Reynolds number, with the internal interface locations between the Ω_2/Ω_1 or Ω_2/Ω_3 sub-domains placed at $z^+ \approx 200 - 250$ at all Reynolds numbers, as shown in Table 3.1. The continuity of the velocity field, $\overline{u}_i$, and its normal derivative, $\partial\overline{u}_i/\partial z$, were enforced at the internal interfaces between these sub-domains, as described in detail in Sections 3.1.3–3.1.5. No-slip boundary conditions were applied at the two-walls in both the full domain and minimal flow unit.

Algebraic mappings (*Kosloff and Talezer*, 1993; *Halilogl u*, 2007) were used to

project the $\xi_s \in [-1, 1]$ domain of Chebyshev polynomials to the physical domain in the wall-normal direction, in order to maintain the desired distribution of grid points in each sub-domain. The specific algebraic mappings employed in the present study are given by

$$\frac{z}{h} = (\frac{L_{z,s}}{h} - 1) - \frac{A_w(1-\xi_s)}{1 + 2A_w h/L_{z,s} + \xi_s} \qquad \text{for } s = 1, \tag{3.3a}$$

$$\frac{z}{h} = \frac{A_c \xi_s}{(1 + (2A_c h/L_{z,s})^2 - \xi_s^2)^{1/2}} \qquad \text{for } s = 2, \tag{3.3b}$$

$$\frac{z}{h} = -(\frac{L_{z,s}}{h} - 1) + \frac{A_w(1-\xi_s)}{1 + 2A_w h/L_{z,s} + \xi_s} \qquad \text{for } s = 3, \tag{3.3c}$$

where h denotes the channel half-height, $L_{z,s}$ denotes the wall-normal height of sub-domain Ω_s, and A_w and A_c are appropriate scale factors. The specific values of $L_{z,s}$, A_w, and A_c for each case are summarized in Table 3.1.

Using the mappings (3.3a)–(3.3c), nearly same distribution of grid points in inner scaling (+ units) was maintained in the Ω_1 and Ω_3 sub-domains at all Reynolds numbers, with a fixed number of grid points in these sub-domains, as shown in Table3.2. Maintaining such a distribution of grid points in the Ω_1 and Ω_3 sub-domains was found to be critical for accurate prediction of the friction-coefficient at all Reynolds numbers. Similarly, in the wake region, $z/h > 0.3$, the mappings result in a nearly uniform distribution of grid points in outer (z/h) scaling at all Reynolds numbers, as shown in Table3.2. This makes the required number of grid points in the wake region also independent of Reynolds number for a full domain of a fixed size in outer scaling. In the logarithmic region ($z^+ > 3{Re_\tau}^{1/2}$ and $z/h < 0.3$) (*Marusic et al.*, 2013; *Meneveau and Marusic*, 2013), where the size of the eddies grows in proportion to the distance from the wall, the required number of grid points has a weak dependence on Re_τ and grows as $\log(Re_\tau)$, as shown in Section 2.3. Because of the weak, logarithmic nature of this dependence on Re_τ, computations can be performed with

a fixed number of grid points in the wall-normal direction over nearly a decade of Re_τ values in this region as well, which is the approach adopted in the present study. Since the computational grids for both the minimal flow unit and the full domain are well-resolved in the wall-normal direction in the near-wall region, no additional wall models are needed and the non-slip boundary condition is prescribed at the wall.

In the homogeneous streamwise and spanwise directions, the grid spacings in the full domain and the minimal flow unit are kept fixed in outer scaling (z/h) and wall scaling ($^+$ unit), respectively, as described in Section 2.3. Therefore, for the turbulent channel flows in this study, the required number of grid points in the streamwise and spanwise directions remains independent of Reynolds number.

3.1.2 Temporal Discretization

The LES governing equations (2.1) were integrated in time using a fractional-step (splitting) method with a partially-implicit treatment of the viscous terms (*Yakhot et al.*, 1989). The scheme can be summarized as follows

1. Nonlinear step:

$$\frac{\overline{u}_i^* - \overline{u}_i^n}{\Delta t} = \frac{3}{2}N_i^n - \frac{1}{2}N_i^{n-1}, \tag{3.4}$$

2. Pressure step:

$$\begin{aligned} \frac{\overline{u}_i^{**} - \overline{u}_i^*}{\Delta t} &= -\frac{\partial \overline{p}^{n+1}}{\partial x_i}, \\ \frac{\partial \overline{u}_i^{**}}{\partial x_i} &= 0, \end{aligned} \tag{3.5}$$

3. Viscous step:

$$\begin{aligned} \frac{\overline{u}_i^{n+1} - \overline{u}_i^{**}}{\Delta t} &= \frac{\partial}{\partial x_j}\left(\langle\langle \nu_T^n \rangle\rangle \frac{\partial \overline{u}_i^{n+1}}{\partial x_j}\right) + F_i^n, \\ F_i^n &= \frac{\partial}{\partial x_j}\left((\nu_T^n - \langle\langle \nu_T^n \rangle\rangle)\frac{\partial \overline{u}_i^n}{\partial x_j}\right) + \frac{\partial}{\partial x_j}\left(\nu_t^n \frac{\partial \overline{u}_j^n}{\partial x_i}\right). \end{aligned} \tag{3.6}$$

Here, the superscripts n and $n+1$ denote the time-steps, $N_i = -\overline{u}_j \frac{\partial \overline{u}_i}{\partial x_j}$, $\nu_t = C\overline{\Delta}^2|\overline{S}|$ denotes the turbulent eddy viscosity, $\nu_T = \nu + \nu_t$ is the total effective viscosity, and $\langle\!\langle\ \rangle\!\rangle$ denotes spatial averaging in the homogeneous directions. The two equations in the pressure step are combined into a single Poisson equation for the wall-normal component of the velocity, which is solved subject to the inviscid boundary conditions $\overline{u}_3{}^{**} = 0$ at the walls. The last step incorporates viscous effects and imposes the viscous boundary conditions on all components of the velocity. In this step, the mean effective viscosity is incorporated implicitly, while variations about this mean are incorporated explicitly.

3.1.3 Internal Interface Boundary Conditions

With the time integration scheme given by equations (3.4)–(3.6), the solution of the Navier-Stokes equations at each time step reduces to an advection step plus a sequence of solutions of elliptic equations for each Fourier mode $(\alpha m, \beta n)$ in the pressure and viscous steps. The general elliptic problem to be solved is of the form

$$\begin{aligned} Lv_{i,s} \equiv \frac{d}{dz}\left(q_s \frac{d}{dz}\right) v_{i,s} + \gamma v_{i,s} &= f_{i,s} \qquad \text{in} \quad \Omega_s, \\ v_{i,s} &= 0 \qquad \text{on} \quad \partial\Omega, \end{aligned} \tag{3.7}$$

where $v_{i,s}(m,n,z,t)$ is given in equations (3.1)–(3.2), $q_s(z)$ and $f_{i,s}(z)$ are known variables, and γ is a negative constant.

The equations for these second-order problems are solved using a patching collocation spectral domain decomposition method (*Orszag*, 1980; *Canuto et al.*, 2007), subject to the boundary conditions that enforce the continuity of the velocity field, $\overline{u}_i$, and its normal derivative, $\partial\overline{u}_i/\partial z$, at the internal interfaces between the sub-domains. In the present numerical implementation utilizing Fourier series in the wall-parallel directions, these internal boundary conditions are specified mode by mode in the

Fourier space as

$$
\begin{aligned}
v_{i,s}(m,n,z,t) &= v_{i,s+1}(m,n,z,t) \qquad \text{for } i = x,y,z, &(3.8)\\
\frac{dv_{i,s}(m,n,z,t)}{dz} &= \frac{dv_{i,s+1}(m,n,z,t)}{dz} \qquad \text{for } i = x,y,z, &(3.9)
\end{aligned}
$$

where the subscripts s and $s+1$ denote neighboring sub-domains. As a result, the solution to equation (3.7) is C^1 continuous (*Canuto et al.*, 2007).

3.1.4 Direct Solver

When $q(z)$ in equation (3.7) is constant, such as in equations resulting from the pressure step, the elliptic equations (3.7) and (3.8-3.9) are solved using the direct patching method suggested by *Israeli et al.* (1993). In such cases, equation (3.7) can be written as

$$
\begin{aligned}
\frac{d^2}{dz^2}v_z - \lambda^2 v_z &= g(z) \quad \text{on } z \in [-h,h], &(3.10)\\
v_z &= 0 \qquad \text{at } z = \pm h, &(3.11)
\end{aligned}
$$

where λ is a constant.

The overall solution v_z to equations (3.10–3.11) is represented as a collection of solutions $v_{z,s}$ in each sub-domain, each of which is decomposed into a homogeneous solution $v^h_{z,s}$ and a particular solution $v^p_{z,s}$,

$$
\begin{aligned}
v_z &= \bigcup_{s=1}^{3} v_{z,s}, &(3.12)\\
v_{z,s} &= v^h_{z,s} + v^p_{z,s}.
\end{aligned}
$$

For the particular solution, $v^p_{z,s}$, the unknown boundary conditions at the grid interfaces $\Gamma_s, s = 1,2$, are chosen arbitrarily and the equations in each sub-domain

are solved using a collocation diagonalization method (*Haidvogel and Zang*, 1979). The resulting particular solution $v_z^p = \bigcup_{s=1}^{3} v_{z,s}^p$ and its first derivative dv_z^p/dz are discontinuous at the interfaces Γ_s. The continuity of the overall solution v_z is imposed using the homogeneous solutions $v_{z,s}^h$ in each sub-domain, which are obtained analytically as

$$v_{z,s}^h = A_s e^{\lambda(z_s - l_s)} + B_s e^{-\lambda z_s} \quad \text{on } z_s \in [0, l_s]. \tag{3.13}$$

The coefficients A_s and B_s are determined so that the continuity conditions

$$v_{z,s} = v_{z,s+1}, \tag{3.14}$$

$$\frac{d}{dz} v_{z,s} = \frac{d}{dz} v_{z,s+1} \tag{3.15}$$

at the interfaces Γ_s are satisfied.

Combining equations (3.13)–(3.15), one obtains

$$A_{s+1} = A_s e^{-\lambda l_s} + \varphi_s, \quad B_s = B_{s+1} e^{-\lambda l_{s+1}} + \psi_s, \tag{3.16}$$

where

$$\varphi_s = \frac{1}{2}\left(\frac{\delta_s'}{\lambda} + \delta_s\right), \qquad \psi_s = \frac{1}{2}\left(\frac{\delta_s'}{\lambda} - \delta_s\right), \tag{3.17}$$

$$\delta_s = v_{z,s}^p(0) - v_{z,s+1}^p(l_{s+1}), \qquad \delta_s' = \frac{d}{dz} v_{z,s}^p(0) - \frac{d}{dz} v_{z,s+1}^p(l_{s+1}).$$

Applying the global boundary conditions one gets

$$A_1 + B_1 e^{-\lambda l_1} = \varphi_o, \quad A_3 e^{-\lambda l_3} + B_3 = \psi_3, \tag{3.18}$$

where

$$\varphi_o = -v_{z,1}^p(l_1) = 0, \quad \psi_3 = -v_{z,3}^p(0) = 0. \tag{3.19}$$

Thus, the solution to the Poisson equation (3.10–3.11) can be obtained by solving equations (3.16) and (3.18) for the unknown coefficients A_s and B_s, which can be achieved by solving a cyclic quasi-bidiagonal matrix:

$$\begin{pmatrix} 1 & 0 & 0 & 0 & 0 & E_1 \\ -E_1 & 1 & 0 & 0 & 0 & 0 \\ 0 & -E_2 & 1 & 0 & 0 & 0 \\ 0 & 0 & E_3 & 1 & 0 & 0 \\ 0 & 0 & 0 & -E_3 & 1 & 0 \\ 0 & 0 & 0 & 0 & -E_2 & 1 \end{pmatrix} \begin{pmatrix} A_1 \\ A_2 \\ A_3 \\ B_3 \\ B_2 \\ B_1 \end{pmatrix} = \begin{pmatrix} \varphi_o \\ \varphi_1 \\ \varphi_2 \\ \psi_3 \\ \psi_2 \\ \psi_1 \end{pmatrix}, \tag{3.20}$$

where $E_s \equiv e^{-\lambda l_s}$.

Overall, the patching algorithm described here analytically enforces the continuities of the solution and its first derivative at the grid interfaces.

3.1.5 Iterative Solver

For non-constant $q(z)$, such as in elliptic equations which result from the viscous step, the above direct solver is no longer applicable and an iterative patching method has to be applied. In this case, the so-called Dirichlet-Neumann method (or iteration-by-sub-domains method) suggested by *Funaro et al.* (1988) is used to solve equation (3.7) subject to the interface conditions (3.8) and (3.9). The procedure alternates the solutions of Dirichlet boundary problems on the odd sub-domains with those of Neumann boundary problems on the even sub-domains, and can be summarized as follows:

for s odd, solve:

$$\begin{aligned} (Lv_{i,s}^n - f_{i,s}) &= 0 \qquad \text{in } \Omega_s, \\ v_{i,s}^n &= 0 \qquad \text{on } \Omega_s \cap \partial\Omega, \\ v_{i,s}^n &= \lambda^n \qquad \text{on } \Gamma_s \cup \Gamma_{s-1}, \end{aligned} \tag{3.21}$$

for s even, solve:

$$\begin{aligned} (Lv_{i,s}^n - f_{i,s}) &= 0 \qquad \text{in } \Omega_s, \\ v_{i,s}^n &= 0 \qquad \text{on } \Omega_s \cap \partial\Omega, \\ \frac{dv_{i,s}^n}{dx_3} &= \frac{dv_{i,s+1}^n}{dx_3} \qquad \text{on } \Gamma_s, \\ \frac{dv_{i,s}^n}{dx_3} &= \frac{dv_{i,s-1}^n}{dx_3} \qquad \text{on } \Gamma_{s-1}, \end{aligned} \tag{3.22}$$

where n denotes iteration over the sub-domains and

$$\lambda^{n+1} = \begin{cases} \theta_n v_{i,s-1} + (1-\theta_n)\lambda^n & \text{on } \Gamma_{s-1}, \\ \theta_n v_{i,s+1} + (1-\theta_n)\lambda^n & \text{on } \Gamma_s. \end{cases} \tag{3.23}$$

Here, the parameter θ_n in equation (3.23) is a relaxation parameter applied in the preconditioned minimum residual method (PMR) (*Canuto et al.*, 2007) used to solve the discretized boundary value problem (3.21) or (3.22) in each sub-domain. The value of θ_n is determined using a minimal error approach (*Funaro et al.*, 1988), where the first relaxation parameter θ_1 is assigned a value and the subsequent θ_n ($n \geq 2$) are determined using

$$\theta_n = \frac{\sum_{s=1,odd}^{S-1}(e_{i,s}^n, e_{i,s+1}^n)_{\Gamma_s} + \sum_{s=2,even}^{S-1}(e_{i,s+1}^n, e_{i,s+1}^n - e_{i,s}^n)_{\Gamma_s}}{\sum_{s=1}^{S-1} |e_{i,s}^n - e_{i,s+1}^n|_{\Gamma_s}^2}, \tag{3.24}$$

where

$$e^n_{i,s} \equiv v^n_{i,s} - v^{n-1}_{i,s}, \tag{3.25}$$

and ( ) and | | denote the approximation to the inner product and its norm, respectively.

3.2 Subgrid-scale Model

The nested-LES approach can be applied with any SGS model of choice. In the present study, the Dynamic Smagorinsky Model (DSM) of *Germano et al.* (1991) and *Lilly* (1992) with sharp, spectral, cutoff filters has been used because of its simplicity and known performance characteristics.

In DSM, the SGS stresses in equation (2.1) are modelled using the gradient transport hypothesis as

$$\tau^*_{ij} = \tau_{ij} - \frac{1}{3}\delta_{ij}\tau_{kk} = -2\nu_t\overline{s}_{ij} = -2C\overline{\Delta}^2|\overline{s}|\overline{s}_{ij}, \tag{3.26}$$

where $\overline{s}_{ij} = \frac{1}{2}\left(\frac{\partial\overline{u}_i}{\partial x_j} + \frac{\partial\overline{u}_j}{\partial x_i}\right)$ is the resolved rate of strain tensor, ν_t denotes the eddy-viscosity, $C = C_s^2$ is square of the Smagorinsky coefficient C_s, $\overline{\Delta}$ is the characteristic width of the LES filter, and $|\overline{s}| = (2\overline{s}_{ij}\overline{s}_{ij})^{1/2}$. The coefficient C is determined using a dynamic procedure proposed by *Germano et al.* (1991) and *Lilly* (1992), given by

$$C(\boldsymbol{x}, t) = -\frac{1}{2}\frac{\langle\langle L_{ij}M_{ij}\rangle\rangle}{\langle\langle M_{ij}M_{ij}\rangle\rangle}, \tag{3.27}$$

where $L_{ij} = (\widetilde{\overline{u}_i\overline{u}_j} - \widetilde{\overline{u}}_i\widetilde{\overline{u}}_j)$, $M_{ij} = (\widetilde{\overline{\Delta}}^2|\widetilde{\overline{s}}|\widetilde{\overline{s}}_{ij} - \overline{\Delta}^2\widetilde{|\overline{s}|\overline{s}_{ij}})$, the brackets $\langle\langle\ \rangle\rangle$ denote averaging in the homogeneous directions, and the superscript $\widetilde{\ }$ denotes a test filter. In the present study, following the original formulation by *Germano et al.* (1991) and *Lilly* (1992), the implicit spectral cutoff LES filters are placed at the de-aliased

grid filter location, while test filtering is applied only in the streamwise and spanwise directions, and the test filters are placed at one-half the implicit LES filter location. All the simulations were de-aliased using the so-called 2/3 rule (*Canuto et al.*, 2006).

In LES, only the filtered velocity, $\overline{u}_i$, is computed. Consequently, the turbulent stresses, $\langle \overline{u}_i' \overline{u}_j' \rangle$, computed in LES, are not the true RANS stresses, $\langle u_i' u_j' \rangle$. Here, $\overline{u}_i' = \overline{u}_i - \langle \overline{u}_i \rangle$ denotes the fluctuating velocity field in LES, $u_i' = u_i - \langle u_i \rangle$ denotes the RANS fluctuating velocity field, $\overline{u}_i$ is the velocity field resolved in LES, u_i is the full velocity field, and $\langle\ \rangle$ denotes ensemble-averaging in time, and in space, over the homogeneous flow directions. To allow meaningful comparisons between LES results and the RANS turbulence statistics obtained in DNS and experiments, the RANS turbulent stresses were recovered from the turbulent stresses computed in LES, using the formulation suggested by *Voelkl et al.* (2000) and *Winckelmans et al.* (2002), given by

$$\langle u_i' u_j' \rangle \simeq \langle \overline{u}_i' \overline{u}_j' \rangle + \langle \tau_{ij}^* \rangle + \frac{1}{3} \delta_{ij} \langle \tau_{kk} \rangle, \tag{3.28}$$

where $\tau_{ij}^* = \tau_{ij} - \frac{1}{3}\delta_{ij}\tau_{kk}$ denotes the deviatoric part of the SGS stress tensor, and $\langle \tau_{kk} \rangle$ is the SGS turbulent kinetic energy (TKE).

During the course of LES, τ_{kk} can be lumped with the pressure term and solved implicitly, and therefore is not modelled explicitly with most SGS models. With such SGS models, including the DSM employed in the present study, application of equation (3.28) to obtain $\langle u_i' u_j' \rangle$ requires a method for reconstructing $\langle \tau_{kk} \rangle$. In the present study, the SGS TKE is recovered from the one-dimensional (1D) energy spectra obtained in LES at each wall-normal location using an analytical formulation of the 1D energy spectra in wall flows, which was derived from Pao's (*Pao*, 1965) or Meyers & Meneveau's (*Meyers and Meneveau*, 2008) three-dimensional (3D) spectrum for isotropic turbulence. These analytical 1D spectra were used to 'continue' the 1D energy spectra from LES down to the Kolmogorov scale. The SGS TKE was then

recovered by integrating the areas under these combined LES and analytical spectra.

The details on this method of recovery of SGS TKE and reconstruction of true RANS stresses from LES results are given in Appendix A. This method has been applied to all the simulations performed with nested-LES presented in this study. In these applications, only the recovered RANS statistics based on the 1D energy spectra formulated using Pao's spectrum (*Pao*, 1965) are presented, for its simpler form and less model parameters. The RANS turbulent stresses obtained using the 1D energy spectra formulated based on Meyers & Meneveau's spectrum (*Meyers and Meneveau*, 2008) are virtually identical, as shown in the examples shown in Appendix A.

3.3 Simulation Parameters

The simulations of equilibrium turbulent channel flow were performed at bulk Reynolds numbers, $Re_b \equiv U_b h/\nu$, of 20000, 45000, 125000, and 275000, which correspond to friction Reynolds numbers, $Re_\tau \equiv u_\tau h/\nu$, of 1016, 2066, 5051, and 10068, respectively, based on the u_τ from Dean's correlation (*Dean*, 1978). Throughout this study, these cases will be referred to as 'nominal' $Re_\tau \approx 1000$, 2000, 5000, and 10000, respectively, as shown in Table 3.1.

The simulations of non-equilibrium, strained turbulent channel flow were designed to emulate the experimental conditions of *Driver and Hebbar* (1987, 1991), in which an initially two-dimensional turbulent boundary layer (TBL) at $Re_\theta \approx 6900$ ($Re_\tau \approx 2000$) was driven to three-dimensionality by impulsive transverse motion of the wall at speed $V_s = U_\infty$ over a length $L_s \approx 32.6\delta_0$, followed by cessation of the transverse motion of the wall, and recovery to initial two-dimensional state, as shown in Figure 3.3(a). Here, U_∞ denotes the free-stream velocity in the original TBL, δ_0 denotes the boundary layer thickness at the end of the shearing zone, and L_s denotes the length of the shearing zone. In the large eddy simulations, a fully-developed, equilibrium

turbulent channel flow at $Re_\tau \approx 2000$ is subjected to impulsive transverse motion of one of the walls at speed $V_s = U_c$ for a time period T_s, followed by cessation of the transverse motion of the wall, and recovery to equilibrium turbulent channel flow, as shown in Figure 3.3(b), where U_c denotes the mean centreline velocity in the initial equilibrium turbulent channel. The correspondence between 'time' in simulations and 'position' in experiments is computed based on Taylor's hypothesis,

$$\frac{tU_c}{h} = \frac{x}{\delta(x)}, \tag{3.29}$$

where t is the time from the start of the transverse motion of the lower wall in the simulations, x denotes the streamwise distance from the leading edge of the moving wall-section in the experiments (see Figure 3.3a), and $\delta(x)$ is the local boundary thickness in the experiments. The evolution of turbulence statistics from equilibrium channel flow to strained, non-equilibrium flow, and recovery to equilibrium turbulent channel flow is tracked in LES and compared to experimental measurements (*Driver and Hebbar*, 1987, 1991). In comparing the turbulence statistics from TBL experiments to LES predictions in turbulent channel flow, the normalized wall-normal location, $z/\delta(x)$, mean velocities, $\langle \overline{u}_i \rangle / U_\infty$, and turbulent stresses, $\langle u_i' u_j' \rangle / U_\infty^2$, from the TBL were equated with z/h, $\langle \overline{u}_i \rangle / U_c$, and $\langle u_i' u_j' \rangle / U_c^2$ in channel flow, respectively. The evolution of all quantities is tracked as a function of $x^* = (x - x_0)/\delta_0$ in experiments, where x_0 and δ_0 denote the x-location and boundary-layer thickness at the end of the shearing zone, respectively. In the simulations, x^* is equated to the time in the simulations according to $x^* = t^* = (t - T_s)\frac{U_c}{h}\frac{\delta(x)}{\delta_0}$. It should be noted, however, that the correspondence between the temporal evolution of the strained channel flow studied in nested-LES and the spatial development of shear-driven, three-dimensional turbulent boundary layer is approximate, as the convective velocities in wall-bounded turbulent flows can be scale-dependent (*del Alamo and Jimenez*, 2009) and the anal-

ogy between turbulent channel flow and TBL has been shown to be only approximate, especially in the outer layer (*Jimenez et al.*, 2010).

All the simulations of equilibrium and non-equilibrium channel flow were performed in full domains of size $L_x \times L_y \times L_z = 2\pi h \times \pi h \times 2h$, and minimal flow units of size $l_x^+ \approx 3200 - 3900$, $l_y^+ \approx 1600 - 1950$ wall units, and $l_z = 2h$ in the streamwise, spanwise, and wall-normal directions, respectively, as shown in Table 3.1. Grid resolutions of $64 \times 64 \times 17/33/17$ were employed in both the full domain and the minimal flow unit as the standard resolution in all the simulations, independent of the Reynolds number. With these domains sizes and grid resolutions, grid spacings of $\Delta_x^+ \approx 50$–60 in the streamwise direction and $\Delta_y^+ \approx 25$–30 in the spanwise direction were maintained in the minimal flow unit at all Reynolds numbers, while in the full domain, grid spacings of $\Delta_x/h = 2\pi/64 \approx 0.1$ in the streamwise direction and $\Delta_y/h = \pi/64 \approx 0.05$ in the spanwise direction were maintained at all Reynolds numbers. In the wall-normal direction, the same grid distribution was used in the full domain and minimal flow unit at each Reynolds number. The specific grid distributions employed at each Reynolds number are shown in Table 3.2. With the aid of the patching collocation method and the mappings discussed in Section 3.1.1, a nearly fixed distribution of grid points in inner scaling ($^+$ units) was maintained in the near-wall region ($0 \leq z^+ \leq$ 200-250) at all Reynolds numbers to resolve the near-wall region down to the viscous sublayer and the wall, as shown in Table 3.2. In the wake region, $z/h > 0.3$, the patching collocation method and the mappings discussed in Section 3.1.1 result in nearly uniform grid spacings of $\Delta_z/h \approx 0.05$-0.1 at all Reynolds numbers, while in the logarithmic region, between $z^+ \geq 3Re_\tau^{1/2}$ and $z/h \leq 0.3$, the grid size almost linearly increases from its value in the near-wall sub-domain to its values in the wake region.

In addition to these 'standard-resolution' cases, nested-LES of equilibrium turbu-

lent channel flow at $Re_\tau \approx 2000$ and 5000 were performed with double the resolution in each direction, to verify the grid-independence of the results. These cases, which were performed with grid resolutions of $128 \times 128 \times 33/65/33$, are denoted by 2000^h and 5000^h in Table 3.1.

Furthermore, to assess the effectiveness of the nested-LES approach, a set of non-nested large eddy simulations were performed in equilibrium and non-equilibrium turbulent channel flows at $Re_\tau \approx 2000$ in domains of the same size as the full domain and minimal flow unit of the nested-LES, with the same grid resolutions as those employed in nested-LES. These cases are denoted by 2000^F and 2000^M, 2000-S^F and 2000-S^M in Table 3.1.

All simulations were initialized from an LES database of fully-developed turbulent channel flow at $Re_\tau \approx 570$. A constant flow rate (per unit width) was maintained in both the full domain and minimal flow unit throughout the course of all simulations.

The turbulence statistics reported in equilibrium turbulent channel flow were obtained by ensemble-averaging the flow quantities in space, over the homogeneous flow directions, and in time, over approximately ten eddy turn-over times, h/u_τ. The turbulence statistics reported in the non-equilibrium, strained turbulent channel flow were obtained by ensemble-averaging the flow quantities in space, over the homogeneous flow directions, and over ten independent realizations of the strained turbulent channel flow, each initialized from a different nested-LES realization of a fully-developed, equilibrium turbulent channel flow at $Re_\tau \approx 2000$.

$Re_\tau\|_{\text{nom}}$	$\mathscr{D}$	$(L_x, L_y, L_{z,s})/h$	$(L_x^+, L_y^+, L_{z,s}^+)\|_{\text{nom}}$	N_x, N_y, $N_{z,s}$	Δ_x^+, Δ_y^+	A_w	A_c
Nested-LES in equilibrium turbulent channel flow							
1000	$\mathscr{F}$	2π, π, 0.2/1.6/0.2	6280, 3140, 200/1600/200	64, 64, 17/33/17	98, 49	0.1	1.2
	$\mathscr{M}$	π, $\frac{\pi}{2}$, 0.2/1.6/0.2	3140, 1570, 200/1600/200	64, 64, 17/33/17	49, 25		
2000	$\mathscr{F}$	2π, π, 0.1/1.8/0.1	12560, 6280, 200/3600/200	64, 64, 17/33/17	196, 98	0.05	1.5
	$\mathscr{M}$	$\frac{\pi}{2}$, $\frac{\pi}{4}$, 0.1/1.8/0.1	3140, 1570, 200/3600/200	64, 64, 17/33/17	49, 25		
5000	$\mathscr{F}$	2π, π, 0.05/1.9/0.05	31400, 15700, 250/9500/250	64, 64, 17/33/17	490, 245	0.02	2.5
	$\mathscr{M}$	$\frac{\pi}{4}$, $\frac{\pi}{8}$, 0.05/1.9/0.05	3920, 1960, 250/9500/250	64, 64, 17/33/17	61, 31		
10000	$\mathscr{F}$	2π, π, 0.025/1.95/0.025	62800, 31400, 250/19500/250	64, 64, 17/33/17	980, 490	0.008	2.5
	$\mathscr{M}$	$\frac{\pi}{8}, \frac{\pi}{16}$, 0.025/1.95/0.025	3920, 1960, 250/19500/250	64, 64, 17/33/17	61, 31		
2000^h	$\mathscr{F}$	2π, π, 0.1/1.8/0.1	12560, 6280, 200/3600/200	128, 128, 33/65/33	98, 49	0.05	1.5
	$\mathscr{M}$	$\frac{\pi}{2}$, $\frac{\pi}{4}$, 0.1/1.8/0.1	3140, 1570, 200/3600/200	128, 128, 33/65/33	25, 12		
5000^h	$\mathscr{F}$	2π, π, 0.05/1.9/0.05	31400, 15700, 250/9500/250	128, 128, 33/65/33	245, 123	0.02	2.5
	$\mathscr{M}$	$\frac{\pi}{4}$, $\frac{\pi}{8}$, 0.05/1.9/0.05	3920, 1960, 250/9500/250	128, 128, 33/65/33	31, 15		
Non-nested LES in equilibrium turbulent channel flow							
2000^F	$\mathscr{F}$	2π, π, 0.1/1.8/0.1	12560, 6280, 200/3600/200	64, 64, 17/33/17	196, 98	0.05	1.5
2000^M	$\mathscr{M}$	$\frac{\pi}{2}$, $\frac{\pi}{4}$, 0.1/1.8/0.1	3140, 1570, 200/3600/200	64, 64, 17/33/17	49, 25	0.05	1.5
$2000^{F,h}$	$\mathscr{F}$	2π, π, 2	12560, 6280, 4000	256, 256, 257	49, 25	-	-
Nested-LES in non-equilibrium, strained turbulent channel flow							
2000-S	$\mathscr{F}$	2π, π, 0.1/1.8/0.1	12560, 6280, 200/3600/200	64, 64, 17/33/17	196, 98	0.05	1.5
	$\mathscr{M}$	$\frac{\pi}{2}$, $\frac{\pi}{4}$, 0.1/1.8/0.1	3140, 1570, 200/3600/200	64, 64, 17/33/17	49, 25		
Non-nested LES in non-equilibrium, strained turbulent channel flow							
2000-S^F	$\mathscr{F}$	2π, π, 0.1/1.8/0.1	12560, 6280, 200/3600/200	64, 64, 17/33/17	196, 98	0.05	1.5
2000-S^M	$\mathscr{M}$	$\frac{\pi}{2}$, $\frac{\pi}{4}$, 0.1/1.8/0.1	3140, 1570, 200/3600/200	64, 64, 17/33/17	49, 25	0.05	1.5

Table 3.1: Computational domain sizes, grid resolutions, grid spacings and mapping parameters employed in nested-LES and non-nested LES of equilibrium and non-equilibrium turbulent channel flow in the present study.

$Re_\tau \approx 1000$		$Re_\tau \approx 2000$		$Re_\tau \approx 5000$		$Re_\tau \approx 10000$	
z/h	z^+	z/h	z^+	z/h	z^+	z/h	z^+
0.00000	0.00	0.00000	0.00	0.00000	0.00	0.00000	0.00
0.00064	0.64	0.00032	0.64	0.00014	0.69	0.00006	0.59
0.00260	2.60	0.00130	2.60	0.00056	2.79	0.00024	2.38
0.00595	5.95	0.00298	5.95	0.00128	6.40	0.00055	5.46
0.01082	10.82	0.00541	10.82	0.00234	11.68	0.00100	9.98
0.01739	17.39	0.00870	17.39	0.00377	18.87	0.00162	16.19
0.02591	25.91	0.01295	25.91	0.00566	28.28	0.00244	24.42
0.03667	36.67	0.01833	36.67	0.00807	40.34	0.00351	35.09
0.05000	50.00	0.02500	50.00	0.01111	55.56	0.00488	48.78
0.06621	66.21	0.03311	66.21	0.01489	74.46	0.00662	66.17
0.08549	85.49	0.04275	85.49	0.01951	97.56	0.00880	87.98
0.10769	107.69	0.05385	107.69	0.02500	125.00	0.01148	114.76
0.13204	132.04	0.06602	132.04	0.03124	156.20	0.01464	146.39
0.15673	156.73	0.07837	156.73	0.03782	189.10	0.01812	181.21
0.17878	178.78	0.08939	178.78	0.04392	219.59	0.02149	214.92
0.19434	194.34	0.09717	194.34	0.04836	241.79	0.02404	240.38
0.20000	200.00	0.10000	200.00	0.05000	250.00	0.02500	250.00
0.20000	200.00	0.10000	200.00	0.05000	250.00	0.02500	250.00
0.20555	205.55	0.10588	211.76	0.05523	276.15	0.03040	304.03
0.22193	221.93	0.12328	246.56	0.07080	354.02	0.04649	464.90
0.24839	248.39	0.15153	303.05	0.09639	481.94	0.07291	729.05
0.28384	283.84	0.18960	379.19	0.13145	657.25	0.10909	1090.85
0.32692	326.92	0.23623	472.47	0.17530	876.51	0.15430	1543.00
0.37623	376.23	0.29008	580.16	0.22714	1135.70	0.20770	2077.02
0.43044	430.44	0.34980	699.60	0.28609	1430.46	0.26837	2683.75
0.48832	488.32	0.41415	828.30	0.35126	1756.30	0.33538	3353.80
0.54887	548.87	0.48204	964.09	0.42176	2108.79	0.40779	4077.93
0.61127	611.27	0.55257	1105.15	0.49673	2483.66	0.48473	4847.33
0.67491	674.91	0.62501	1250.01	0.57538	2876.92	0.56538	5653.78
0.73933	739.33	0.69877	1397.54	0.65698	3284.88	0.64897	6489.75
0.80422	804.22	0.77343	1546.87	0.74083	3704.16	0.73484	7348.37
0.86937	869.37	0.84868	1697.35	0.82633	4131.67	0.82234	8223.40
0.93466	934.66	0.92426	1848.52	0.91290	4564.52	0.91091	9109.08
1.00000	1000.00	1.00000	2000.00	1.00000	5000.00	1.00000	10000.00

Table 3.2: Wall-normal grid distribution employed in nested-LES and non-nested LES of equilibrium and non-equilibrium turbulent channel flow at $Re_\tau \approx 1000$, 2000, 5000, and 10000 at 'standard' resolution.

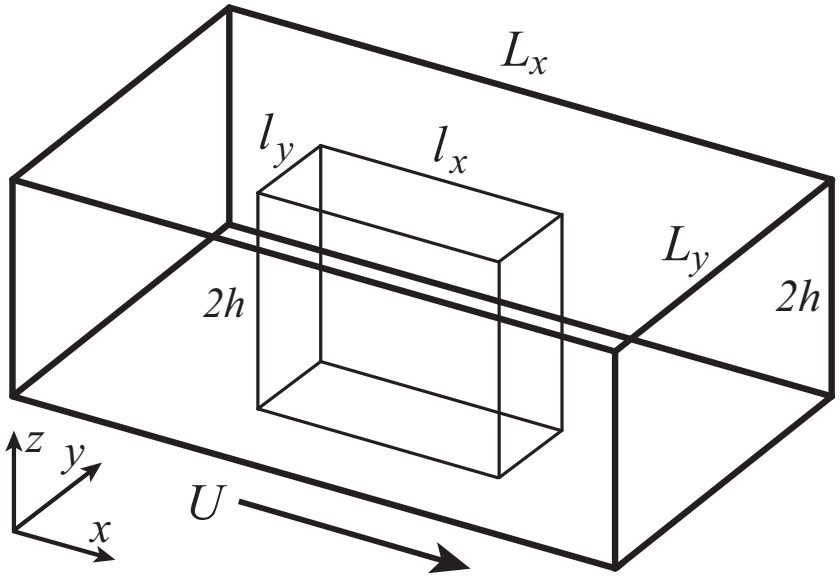

Figure 3.1: The computational domain and coordinate system used in nested-LES of equilibrium and non-equilibrium turbulent channel flow. —— (thick), full domain; —— (thin), minimal flow unit.

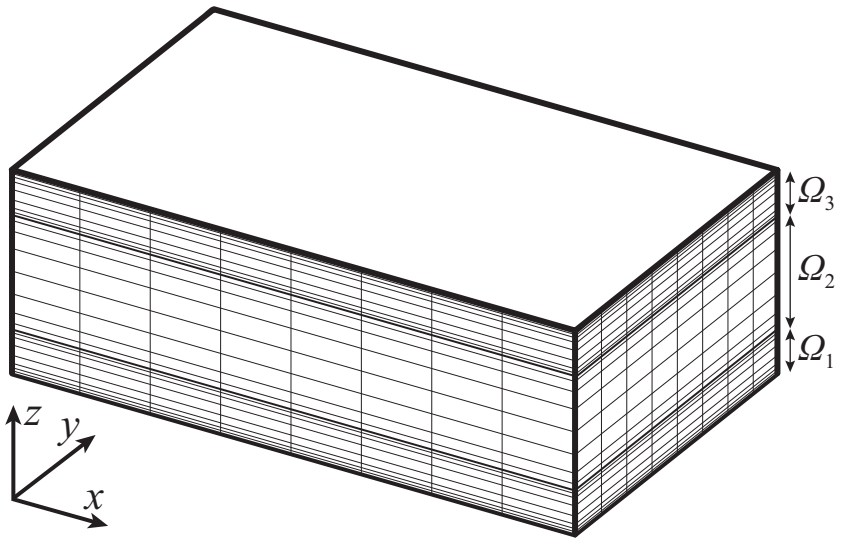

Figure 3.2: The wall-normal grid distribution in the patching collocation spectral domain-decomposition method used in both the full domain and minimal flow unit of nested-LES.

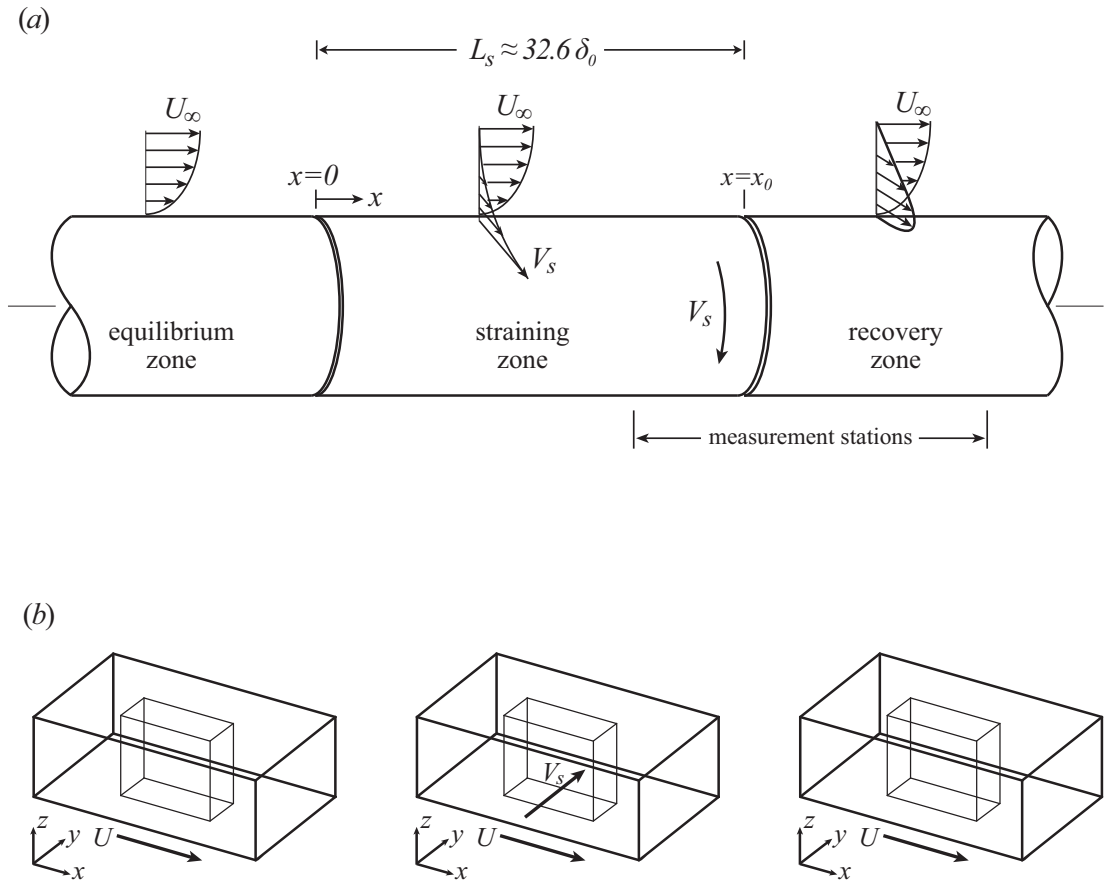

Figure 3.3: (a) Schematic of experimental setup of shear-driven, three-dimensional turbulent boundary layer of *Driver and Hebbar* (1987, 1991); (b) schematic of the channel flow used in simulations of non-equilibrium, strained turbulent channel flow in each of the equilibrium, straining, and recovery zones in the present study.

CHAPTER IV

Results in Equilibrium Turbulent Channel Flow

The performance of the nested-LES approach was first assessed in equilibrium turbulent channel flow at $Re_\tau \approx 1000$, 2000, 5000 and 10000 through comparisons with results from Dean's correlation (*Dean*, 1978), DNS, and experiments. The details on the simulations have been described in Section 3.3 and summarized in Table 3.1. This chapter presents the results of nested-LES in equilibrium turbulent channel flow and discusses the underlying mechanism of the present method.

4.1 Mean statistics

Table 4.1 shows the skin-friction coefficients, $C_f \equiv \langle 2\tau_w \rangle / \rho U_b^2$, predicted by nested-LES in equilibrium turbulent channel flow, at standard and high resolutions, compared to Dean's correlation (*Dean*, 1978). The predicted skin-friction coefficients were within -2.1%, -2.9%, -0.5%, and -0.8% of values from Dean's correlation at $Re_\tau \approx 1000$, 2000, 5000 and 10000, respectively, with standard resolution, and within -2% of the values from Dean's correlation in the high resolution simulations of 2000^h and 5000^h.

The profiles of the mean velocity, turbulence intensities, and Reynolds shear stresses predicted by nested-LES in these flows are shown in Figures 4.1–4.4. The

mean velocity profiles predicted at $Re_\tau \approx$1000, 2000, and 5000 show good agreement with available DNS data at $Re_\tau \approx 950$ (*del Alamo et al.*, 2004), $Re_\tau \approx 2000$ (*Hoyas and Jimenez*, 2006), $Re_\tau \approx 5200$ (*Lee and Moser*, 2015), and experimental data at $Re_\tau \approx 4800$ (*Comte-Bellot*, 1963), respectively. At $Re_\tau \approx 10000$, no DNS data is currently available. Consequently, the nested-LES results were assessed based on a combination of DNS data at $Re_\tau \approx 5200$ (*Lee and Moser*, 2015) and experimental data at $Re_\tau \approx 8600$ (*Comte-Bellot*, 1963). The original experimental data at $Re_\tau \approx 8600$ published by *Comte-Bellot* (1963) displays a mean velocity profile which is shifted relative to the universal law-of-the-wall. In the present study, this experimental data is displayed after adjusting the value of the wall friction velocity, u_τ, in the experiments to bring the experimental data into agreement with the universal law-of-the-wall. All the experimental data of *Comte-Bellot* (1963) at $Re_\tau \approx 8600$ shown in the present study has been normalized using this adjusted u_τ.

The mean velocity profiles predicted by nested-LES exhibit the correct behavior throughout the cross-section of the channel at all Reynolds numbers, including the correct slope in the logarithmic layer, and agreement with DNS and experimental data in the wake region. Furthermore, no change in slope or other anomalies are observed in the mean velocity profiles at $z = z^*$. The high resolution cases of 2000^h and 5000^h predict mean velocity profiles which are virtually indistinguishable from those obtained at standard resolution, consistent with the close agreement between the C_f values of the standard- and high-resolution cases.

Good agreement is also observed in Figures 4.1–4.4 between the turbulence intensities and Reynolds shear stresses predicted by nested-LES and available DNS and experimental data. To allow direct comparison of the nested-LES predictions with available DNS and experimental data, the true RANS turbulence intensities, $\langle u'_\alpha u'_\alpha \rangle^{1/2}$, were reconstructed from the LES results using equation (A.1) and shown

in Figures 4.1–4.4. For reference, the LES turbulence intensities, $\langle \overline{u}'_\alpha \overline{u}'_\alpha \rangle^{1/2}$, without reconstruction are also shown. Unlike most existing wall-modelling approaches, which only provide the turbulence statistics in the outer layer, the nested-LES approach can provide accurate predictions of the turbulent statistics in both the inner and outer layers. Both the locations and magnitudes of the near-wall peaks of the turbulence intensities are accurately predicted at all Reynolds numbers, with the magnitude of the near-wall peak of the streamwise turbulence intensity showing a gradual increase with increasing Reynolds number, consistent with recent observations in experiments (*Marusic et al.*, 2010c) and DNS (*Hoyas and Jimenez*, 2006; *Schlatter et al.*, 2010). The over-prediction of the near-wall peak of the streamwise turbulence intensity by 6–8% at standard resolution, and 3–4% at high resolution, and under-prediction of the streamwise turbulence intensities in the logarithmic layer by up to 10–15% at both resolutions, observed in Figures 4.1–4.4 compared to DNS, are both features of DSM which have also been observed in a number of prior studies. An example of such studies, performed with DSM using well-resolved conventional LES at $Re_\tau \approx 4000$ (*Kravchenko, Moin, and Moser*, 1996; *Cabot and Moin*, 1999), is also shown in Figure 4.3. Similar differences of up to 5%, 10% and 5% at standard resolution, and 3%, 6%, and 2% at high resolution, are also observed in Figures 4.1–4.4 in the prediction of the spanwise and wall-normal turbulent intensities and the Reynolds shear-stress, respectively, compared to DNS.

The high-resolution cases of 2000^h and 5000^h predict reconstructed RANS turbulence intensities and a Reynolds shear-stress within 5% of the results from standard resolution for $z^+ \leq 200$, and within 2% of the results from standard resolution in the rest of the channel, indicating the invariance of the results to the resolution of the grid.

Recovery of the SGS stresses leads to differences of up to 5%, 12%, and 16%, at

standard resolution, and 3%, 8%, and 12% at high resolution, between the RANS and LES turbulence intensities in the streamwise, spanwise, and wall-normal directions, respectively.

4.2 High-order moments

Recent experiments in high Reynolds number turbulent boundary layers and pipe flows (*Hultmark et al.*, 2013; *Marusic et al.*, 2013; *Meneveau and Marusic*, 2013) have confirmed that the variance of the streamwise velocity fluctuations exhibits logarithmic behavior within an inertial sublayer, consistent with and supportive of earlier predictions by models based on the 'attached-eddy' hypothesis (*Townsend*, 1976; *Perry et al.*, 1986). It has further been shown (*Meneveau and Marusic*, 2013) that this logarithmic behavior can be generalized to all even-order moments of the streamwise velocity fluctuations as,

$$\langle (u'^{+})^{2p} \rangle^{1/p} = -A_p \ln(z/\delta) + B_p = -A_p \ln(z^{+}) + D_p(Re_\tau), \tag{4.1}$$

where the coefficients A_p are the generalized 'Townsend-Perry' constants for moments of order $2p$, and appear quite insensitive to the Reynolds number, while B_p and D_p are non-universal constants.

It has been suggested that the ability of LES to reproduce this logarithmic behavior in the higher-order moments of the streamwise velocity fluctuations, with generalized 'Townsend-Perry' constants, A_p, in agreement with experiments, should be used as an additional criterion for evaluation of the capability of LES to capture the fundamental scaling laws and inherent nonlinear dynamics of turbulence (*Stevens, Wilczek, and Meneveau*, 2014). Furthermore, it has been reported that for wall-modelled conventional LES to faithfully reproduce these generalized 'Townsend-Perry' constants,

a fine resolution is required in the simulations (*Stevens et al.*, 2014).

In this section, the ability of the nested-LES approach to predict this logarithmic behavior in the even-order moments of the streamwise velocity fluctuations is explored. Figures 4.5(a) and 4.5(b) show the second ($2p = 2$) and sixth ($2p = 6$) order moments of streamwise velocity fluctuations, $\langle (u'^{+})^{2p} \rangle^{1/p}$, predicted by nested-LES at $1000 \leq Re_\tau \leq 10000$, respectively, while Figure 4.5(c) shows the even-order moments for $2 \leq 2p \leq 12$ at $Re_\tau \approx 10000$. A logarithmic behavior can be observed in all the even-order moments displayed in Figures 4.5(a–c) over the range $z^+ > 3Re^{1/2}$ and $z/h < 0.30$, for which the logarithmic behavior has been observed in experiments (*Marusic et al.*, 2013; *Meneveau and Marusic*, 2013). The data in Figure 4.5(c) indicate that the logarithmic behavior may extend beyond $z/h \sim 0.3$ with increasing order of the moments.

The coefficients A_p and D_p in equation (4.1) were obtained by a least-squares fit to the moments data between $z^+ > 3Re^{1/2}$ and $z/h < 0.30$. Figure 4.5(d) shows the values of the coefficients, A_p, for $2 \leq 2p \leq 12$ obtained from nested-LES results at $1000 \leq Re_\tau \leq 10000$. For reference, the A_p coefficients from experimental measurements in TBL at $Re_\tau \approx 19030$ (*Meneveau and Marusic*, 2013) are also shown. The A_p coefficients obtained from nested-LES at $Re_\tau \approx 10000$ show good agreement with the A_p coefficients from TBL experiments at $Re_\tau \approx 19030$, indicating insensitivity of the A_p coefficients to Reynolds number at high enough values of the Reynolds numbers. At low Reynolds numbers ($Re_\tau \leq 2000$), the trends in A_p coefficients from nested-LES are similar to those observed at low Reynolds numbers in experiments (*Meneveau and Marusic*, 2013). At all Reynolds numbers, the A_p coefficients from both nested-LES and experiments show sub-Gaussian behavior. The limiting asymptotic behavior of the A_p coefficient at high Reynolds numbers indicates that this sub-Gaussian scaling of the moments does not become more Gaussian with increasing Reynolds number.

Further evidence of the sub-Gaussian behavior of the streamwise velocity fluctuations is observed in the plots of skewness and flatness, as shown in Figures 4.6–4.7. Both the skewness and flatness of the streamwise velocity fluctuations display sub-Gaussian behavior in the logarithmic region. A sign change is observed in the skewness of the streamwise velocity fluctuations in the inner layer ($z/h < 0.1$). A similar sign change in the sign of S_u has been reported experimentally, but only in the buffer layer and of much weaker negative magnitude (*Marusic et al.*, 2010b). The profiles of the flatness of the streamwise velocity fluctuations show similar trends to experiments in TBL (*Meneveau and Marusic*, 2013). The spanwise velocity fluctuations display near-Gaussian behavior throughout the logarithmic layer, with skewness and flatness values near the Gaussian values of 0 and 3, respectively. The wall-normal velocity fluctuations display slightly super-Gaussian behavior with a slightly positive skewness and flatness values slightly higher than the Gaussian values.

4.3 Two-point Statistics

The previous sections have established the ability of nested-LES to faithfully predict the one-point statistics in turbulent channel flow. In this section, the ability of nested-LES to predict structural features of the flow is investigated by examining the two-point correlations obtained from nested-LES in turbulent channel flow.

The two-point correlation coefficient, $C_{\varphi\varphi}$, is defined as

$$C_{\varphi\varphi}(\boldsymbol{r}, \boldsymbol{r'}) = \frac{\langle \varphi(\boldsymbol{r})\ \varphi(\boldsymbol{r'}) \rangle}{\sigma_\varphi(\boldsymbol{r})\ \sigma_\varphi(\boldsymbol{r'})}, \tag{4.2}$$

where φ denotes the streamwise, spanwise, or wall-normal velocity fluctuations, $\boldsymbol{r} = (x, y, z)$ and $\boldsymbol{r'} = (x', y', z')$ are the coordinates of the reference point and the moving point, respectively, $\langle\ \rangle$ denotes ensemble-averaging in time and in homogeneous

directions, and $\sigma_\varphi(\boldsymbol{r})$ and $\sigma_\varphi(\boldsymbol{r'})$ are the standard deviations of φ evaluated at $\boldsymbol{r}$ and $\boldsymbol{r'}$, respectively.

Figures 4.8–4.9 show the streamwise (xz) and spanwise (yz) sections of the contour maps of C_{uu}, C_{vv}, C_{ww} at $z/h = 0.1$ and $z/h = 0.6$, based on data from nested-LES at $1000 \leq Re_\tau \leq 10000$. The contour maps of the correlation coefficients at different Reynolds numbers show a reasonable collapse, with the exception of the weakly correlated structures of C_{uu}. This lack of simple Reynolds-number scaling for C_{uu} structures has been observed and reported in several studies (*del Alamo et al.*, 2004; *Jimenez and Hoyas*, 2008; *Sillero et al.*, 2014). The weakly correlated contours of C_{uu} (contours of $C_{uu} \leq 0.1$), suggest a size of structures on the order of $O(4h)$, which is much smaller than the $O(18h)$ reported by *Sillero et al.* (2014) in DNS of turbulent channel flow at $Re_\tau \approx 950$, due to the small domain size employed in the present study. Other features of the structures are consistent with those reported by *Sillero et al.* (2014). On the streamwise section, the streamwise and spanwise velocity fluctuations both exhibit structures which are inclined to the wall. The structures of C_{vv} are inclined at a steeper angle than those of C_{uu}, and exhibit structures with negative correlation above and underneath the ones with positive correlation, indicating the presence of inclined mean vortical motions, consistent with those observed in many earlier studies (*Robinson*, 1991). On the spanwise section, the structures of C_{uu} exhibit the pattern of alternating high- and low-velocity regions. At the same time, C_{vv} shows negative contours below and above the positive core, and C_{ww} has negative contours on the side of the positive core, both indicating evidence of quasi-streamwise vortical structures.

From the contours in the streamwise section, the inclination angles, $\theta_{\varphi\varphi}$, of the structures are computed by fitting a line through the two points which are furthest away upstream and downstream from the reference location at each contour level

between 0.2 and 0.7 (*Wu and Christensen*, 2010). The values of $\theta_{\varphi\varphi}$ obtained at all contour levels and for all Reynolds numbers are then averaged at each wall-normal location, and the resulting values for θ_{uu} and θ_{vv} are shown in Figures 4.8(a,c) and 4.9(a,c).

Figure 4.10 shows the variation of the inclination angles, θ_{uu}, θ_{vv}, and θ_{ww}, as a function of the distance from the wall, from the nested-LES results at $1000 \leq Re_\tau \leq 10000$, compared to the inclination angles reported from DNS of turbulent channel flow at $Re_\tau \approx 950$ (*del Alamo et al.*, 2004; *Sillero et al.*, 2014). In the channel core, the inclination angles predicted by nested-LES asymptote to values of 10°, 25°, and 90° for θ_{uu}, θ_{vv}, and θ_{ww}, respectively, which agree reasonably well with the inclination angles reported by *Sillero et al.* (2014) in DNS of turbulent channel flow at $Re_\tau \approx 950$. The discrepancies observed in Figure 4.10 can be attributed to the different methodologies used for obtaining the inclination angles in the present study compared to *Sillero et al.* (2014).

Figure 4.11 shows the one-dimensional two-point correlation functions in all directions, predicted by nested-LES for all components of the velocity fluctuations in the outer layer ($z/h \approx 0.5$) and the near-wall region ($z^+ \approx 10$). The 1D two-point correlations at $z^+ \approx 10$ were computed from the minimal flow unit of nested-LES, and show evidence of the presence of a streaky structure with a streak spacing of ~ 100 wall units in the near-wall region in Figure (4.11d), indicating that the near-wall dynamics is adequately captured by nested-LES. As with all LES, the diameter of the near-wall streamwise vortices is over-predicted by nested-LES in Figure (4.11d), because the grid size, $\Delta_y^+ \approx 25-30$, employed in the minimal flow unit of nested-LES, is of the same order as the diameter of these structures.

From the two-point correlation functions, one may obtain a measure of the average

size of the structures by computing the integral length scales, $\Lambda_{\alpha,\varphi}$, given by

$$\Lambda_{\alpha,\varphi} = \int C_{\varphi\varphi}(\boldsymbol{r}, \boldsymbol{r'})\ dr_\alpha, \tag{4.3}$$

where r_α denotes x, y, or z. The integrations in equation (4.3) are performed only to $C_{\varphi\varphi} = 0.05$, to avoid the noisy correlation tails and long negative regions in $C_{\varphi\varphi}$, which could cancel out the positively correlated regions (*Sillero et al.*, 2014).

Figure 4.12 shows the integral length scales as function of wall-normal distance predicted by nested-LES at $1000 \leq Re_\tau \leq 10000$. The size of the structures, as inferred from $\Lambda_{\alpha,\varphi}(z)$, better motivate the construction of the grid and the choice of $z^*/h = 0.05$ in the present study. From Figure 4.12, it can be seen that for $z \geq z^*$, the structures have a size $\Lambda_{x,\varphi}/h > 0.15$, $\Lambda_{y,\varphi}/h > 0.07$, and $\Lambda_{z,\varphi}/h > 0.07$. Therefore, for $z > z^*$, the grid-spacings of $\Delta_x/h \approx 0.1$, $\Delta_y/h \approx 0.05$, and $\Delta_z/h \approx 0.05$, employed in the full domain of nested-LES in the present studies, can adequately resolve these structures. However, for $z < z^*$, $\Lambda_{x,v}/h$ and $\Lambda_{x,w}/h$ become smaller than Δ_x/h in the full domain, while $\Lambda_{y,w}/h$ becomes smaller than Δ_y/h in the full domain. Thus the full domain can no longer properly resolve these structures, and the basis for renormalization of the velocity field in equations (2.2)–(2.4) needs to switched from the full domain to the minimal flow unit.

The $\Lambda_{z,\varphi}$ of Figure 4.12 also motivate the construction of the grid and the required number of grid points in the wall-normal direction. In the wake region ($z/h > 0.1$), the $\Lambda_{z,\varphi}$ nearly plateau and all $\Lambda_{z,\varphi}/h$ have values greater than 0.1. Consequently a fixed number of grid points with a nearly uniform grid of size $\Delta_z/h \approx 0.05$-0.1 can properly resolve the turbulence structures in this region at all Reynolds numbers. In contrast, for $z/h < 0.1$, the size of the $\Lambda_{z,\varphi}$ grows approximately linearly with the distance from the wall, and $O(\log Re_\tau)$ grid points are needed to resolve these structures, as discussed in Section 2.3.

4.4 Effect of z^*

This section examines the effect, on the predicted flow statistics and structure, of the placement of z^*, the wall-normal location at which the basis for renormalization of the velocity fields is switched from the velocity field in the minimal flow unit (for $z \leq z^*$), to the velocity field in the full domain (for $z > z^*$). To this end, nested-LES were performed at $Re_\tau \approx 2000$ with $z^*/h = 0.025$, 0.04, 0.07, 0.10, 0.15, and 0.20.

Table 4.2 and Figure 4.13 show these results. The most accurate predictions of C_f and the mean statistics are obtained with $z^*/h = 0.04$ or 0.05. When z^*/h is moved closer to the wall, the computations become under-resolved between $z^*/h < z/h < 0.05$ because of the grid spacings in the x and y directions in the full domain. When z^*/h is moved above $z/h = 0.05$, the computations suffer from the inadequate size of the minimal flow unit in the region $0.05 < z/h < z^*/h$. It appears that the best results are obtained when the solution is switch from the minimal flow unit to the full domain as soon as the grid resolution in the full domain becomes adequate.

While choosing a non-optimal value of z^* slightly degrades the performance of nested-LES, it is not catastrophic. The effect is even less prominent in the prediction of the average flow structures, as shown in Figures 4.14–4.15, where the streamwise and spanwise sections of two-point correlation coefficient, $C_{\varphi\varphi}$, for all components of the velocity fluctuations at $z/h = 0.1$ and $z/h = 0.6$, are plotted for nested-LES at $Re_\tau \approx 2000$ with $z^*/h = 0.025$, 0.04, 0.04, and 0.07. The contours of $C_{\varphi\varphi}$ predicted with different z^* are observed to nearly collapse, with the exception of the large, weakly correlated structures for C_{uu}.

4.5 Renormalization functions

The ability of nested-LES to accurately compute the turbulence statistics and structures results from only minor renormalizations of the velocity fields in the full

domain and the minimal flow unit at each time-step during the course of the simulation. Figures 4.16–4.19 show the time histories of the instantaneous renormalization functions, $R(\langle\langle\overline{u}_{\alpha,\mathscr{D}}\rangle\rangle\langle\langle\overline{u}_{\alpha,\mathscr{D}}\rangle\rangle)$ and $R(\langle\langle\overline{u}''_{\alpha,\mathscr{D}}\overline{u}''_{\alpha,\mathscr{D}}\rangle\rangle)$, for the 'mean' and fluctuating components of the velocity, respectively, from nested-LES of turbulent channel flow at $1000 \leq Re_\tau \leq 10000$. Overall, the renormalization functions show little variation with the Reynolds number. At all Reynolds numbers, $R(\phi_{\alpha,\mathscr{D}})$ remain very close to unity above $z/h = 0.05$, while fluctuating within 1 ± 0.01 for $\langle\langle\overline{u}\rangle\rangle\langle\langle\overline{u}\rangle\rangle$ and $\langle\langle\overline{u}''\overline{u}''\rangle\rangle$, and within 1 ± 0.03 for $\langle\langle\overline{v}''\overline{v}''\rangle\rangle$ and $\langle\langle\overline{w}''\overline{w}''\rangle\rangle$ below $z/h = 0.05$, with the maximum variations occurring close to the wall. When the nested-LES is started from the initial velocity field, the renormalization functions quickly converge to the range above, and no clipping or damping is needed to maintain the stability of the simulations. During the course of the simulations, the values $R(\phi_{\alpha,\mathscr{D}})$ at a given z-location occasionally cross unity, meaning that a given component of the velocity at a given location can alternate between being instantaneously amplified or attenuated.

Figures 4.20–4.21 show the profiles of the time-averaged renormalization functions, $\langle R(\phi_{\alpha,\mathscr{D}})\rangle$, along with the absolute magnitudes of $|1 - \langle R(\phi_{\alpha,\mathscr{D}})\rangle|$, and the standard deviations of $R(\phi_{\alpha,\mathscr{D}})$, from nested-LES of turbulent channel flow at $1000 \leq Re_\tau \leq 10000$. In all cases, the time-averaged renormalization functions, $\langle R(\phi_{\alpha,\mathscr{D}})\rangle$, remain close to unity and stay confined to 1 ± 0.03 for $0 \leq z/h < 0.02$; 1 ± 0.005 for $0.02 \leq z/h < 0.05$; and 1 ± 0.001 for $0.05 \leq z/h \leq 1$. The main effect of $R(\phi_{\alpha,\mathscr{D}})$ in the inner layer ($z \leq z^*$) is to attenuate the streamwise and spanwise turbulence intensities in the full domain by 0.1–1% and 0.1–3%, respectively, while enhancing the wall-normal turbulence intensity by 0.1–3% at each time-step. In addition, the mean streamwise velocity is attenuated by 0.05–0.5% in the inner layer of the full domain. In the outer layer ($z > z^*$), the main effect of $R(\phi_{\alpha,\mathscr{D}})$ is to attenuate the spanwise and wall-normal turbulence intensities by less than 0.1%, while enhancing the streamwise turbulence

intensity by less than 0.1% in the minimal flow unit. Similarly, the correction to the streamwise mean velocity of the minimal flow unit in the outer layer is less than 0.05%. These small corrections, when applied at every time-step, are sufficient to correct the velocity fields and turbulence statistics in both the full domain and minimal flow unit of the nested-LES approach.

4.6 Comparison to non-nested LES

To better understand the mechanisms behind the performance of the nested-LES approach, the simulations at $Re_\tau \approx 2000$ were repeated as non-nested LES in channels with the same domain size and grid resolution as those employed in the full domain and minimal flow unit of nested-LES. These cases are denoted by 2000^F and 2000^M in Tables 3.1 and 4.1.

The skin-friction coefficients predicted in these non-nested LES cases had errors of -31.2% and -21.6%, for cases 2000^F and 2000^M, respectively, compared to Dean's correlation, as shown in Table 4.1. These errors should be contrasted with the error of -2.9% in the prediction of C_f by nested-LES approach at the same Reynolds number, with the same domain sizes and grid spacings. The source of the large errors in C_f for case 2000^F is lack of adequate resolution in the near-wall region, while for case 2000^M, the large errors in C_f arise from the lack of adequate domain size in the outer layer. These errors point to the need for two-way coupling in nested-LES. Clearly, the errors in C_f of non-nested cases can be reduced by performing well-resolved non-nested, conventional LES in the full-size domain, as shown by the case $2000^{F,h}$ in Table 4.1. But such computations require $O(256^3)$ grid points compared to $O(64^3)$ of nested-LES.

The one-point turbulence statistics predicted by these non-nested LES cases also show poor agreement with DNS and resolved conventional LES, as shown in Figure

4.22. For case 2000^F, the mean velocity profile is over-predicted throughout the cross-section of the channel and there is significant pileup of the turbulence kinetic energy near the peaks of the streamwise and spanwise turbulence intensities. This pileup of streamwise turbulence kinetic energy can be attributed to the lack of adequate grid resolution in case 2000^F, needed to resolve the pressure–strain correlations, which are responsible for redistribution of the turbulence kinetic energy from the streamwise to cross-stream directions. For case 2000^M, the mean velocity profile exhibits an excessive wake region and an upward shift of the logarithmic layer, while the peak of the streamwise turbulence intensity is over-predicted in the inner layer, and the turbulence intensities are excessively isotropic in the outer layer. The latter feature is caused by the minimal size of the computational domain, which prevents the large scales from developing into their natural anisotropic states. All these problems are resolved when the nested-LES approach is used. Figure 4.22 shows the turbulence statistics obtained from both the full domain and minimal flow unit of nested-LES. The differences between the two sets of turbulence statistics are hardly noticeable, reflecting the near unity values of $R(\phi_{\alpha,\mathscr{D}})$ in equation (2.4).

$Re_\tau\|_{\text{nom}}$	Re_b	$Re_\tau\|_{\text{Dean's}}$	$Re_\tau\|_{\text{LES}}$	$C_f\|_{\text{Dean's}}$	$C_f\|_{\text{LES}}$	% Error in C_f
1000	20000	1016	1005	5.162×10^{-3}	5.053×10^{-3}	− 2.1 %
2000	45000	2066	2035	4.215×10^{-3}	4.092×10^{-3}	− 2.9 %
5000	125000	5051	5037	3.265×10^{-3}	3.247×10^{-3}	− 0.5 %
10000	275000	10068	10030	2.681×10^{-3}	2.658×10^{-3}	− 0.8 %
2000^h	45000	2066	2020	4.215×10^{-3}	4.147×10^{-3}	− 1.6 %
5000^h	125000	5051	5009	3.265×10^{-3}	3.230×10^{-3}	− 1.1 %
2000^F	45000	2066	1714	4.215×10^{-3}	2.900×10^{-3}	− 31.2 %
2000^M	45000	2066	1828	4.215×10^{-3}	3.302×10^{-3}	− 21.6 %
$2000^{F,h}$	45000	2066	2030	4.215×10^{-3}	4.071×10^{-3}	− 3.4 %

Table 4.1: The skin friction coefficient, C_f, predicted in nested-LES and non-nested LES of equilibrium turbulent channel flow compared to Dean's correlation (*Dean*, 1978).

$Re_\tau\|_{\text{nom}}$	z^*/h	$C_f\|_{\text{Dean's}}$	$C_f\|_{\text{LES}}$	% Error in C_f
2000	0.025	4.215×10^{-3}	4.254×10^{-3}	+ 0.9 %
2000	0.040	4.215×10^{-3}	4.141×10^{-3}	− 1.8 %
2000	0.050	4.215×10^{-3}	4.092×10^{-3}	− 2.9 %
2000	0.070	4.215×10^{-3}	4.053×10^{-3}	− 3.8 %
2000	0.100	4.215×10^{-3}	3.883×10^{-3}	− 7.9 %
2000	0.150	4.215×10^{-3}	3.728×10^{-3}	−11.5 %
2000	0.200	4.215×10^{-3}	3.786×10^{-3}	−10.2 %

Table 4.2: The skin friction coefficient, C_f, predicted in nested-LES of equilibrium turbulent channel flow at $Re_\tau \approx 2000$ with different locations of z^*/h.

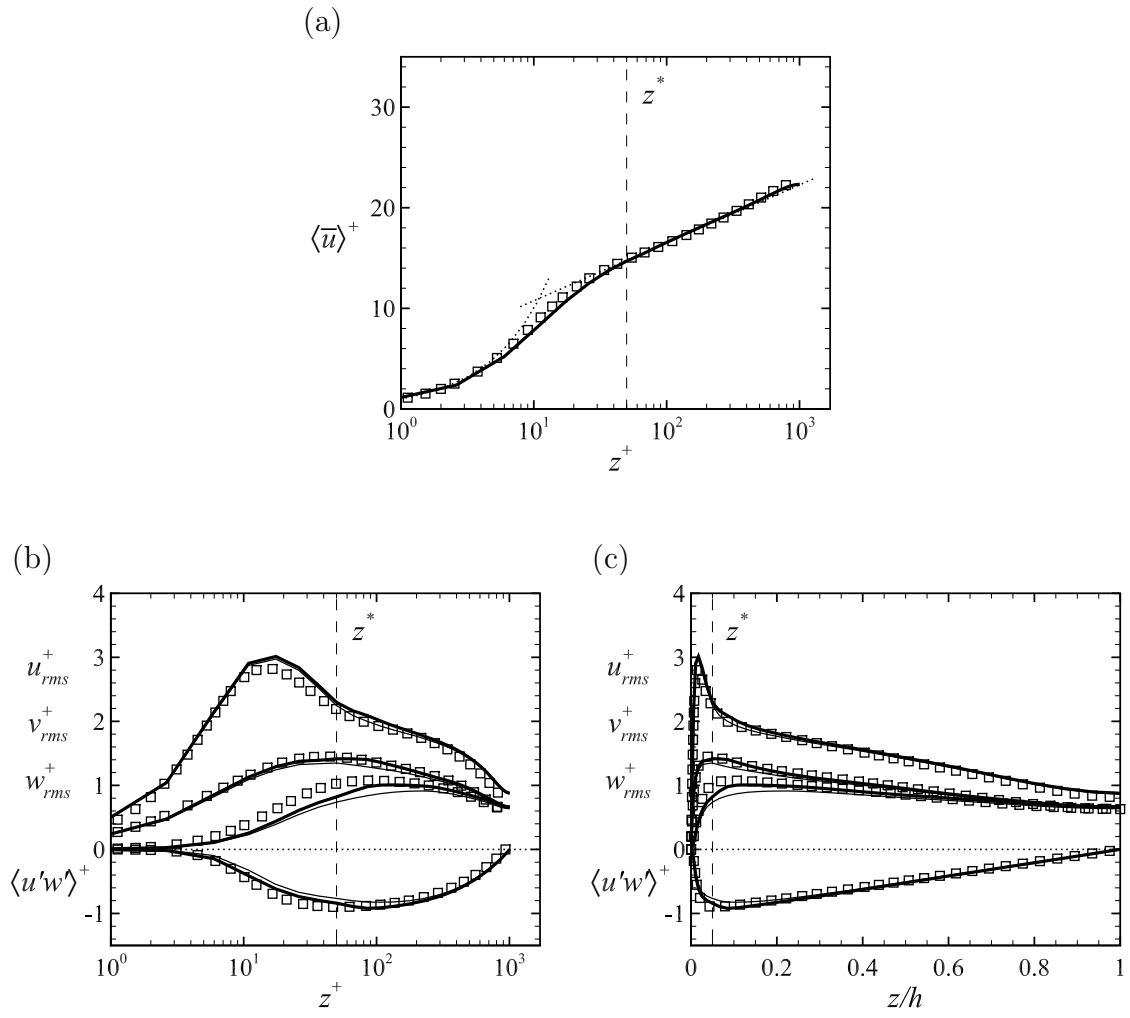

Figure 4.1: Profiles of mean velocity, turbulence intensities, and Reynolds shear stresses predicted by nested-LES in equilibrium turbulent channel flow at $Re_\tau \approx 1000$, compared to DNS data. ——, nested-LES performed at standard resolution; thick lines, mean velocity and RANS turbulence intensities, $\langle u'_\alpha u'_\alpha\rangle^{1/2}$, and Reynolds shear stress, $\langle u'w'\rangle$, reconstructed from nested-LES results using equation (A.1); thin lines, turbulence intensities, $\langle \overline{u}'_\alpha \overline{u}'_\alpha\rangle^{1/2}$, and Reynolds shear stress, $\langle \overline{u}'\overline{w}'\rangle$, predicted by nested-LES without reconstruction; □, DNS of *del Alamo et al.* (2004) at $Re_\tau \approx 950$; $\cdots$, the asymptotes $\langle\overline{u}\rangle^+ = z^+$, and $\langle\overline{u}\rangle^+ = 2.5\ln(z^+) + 5$.

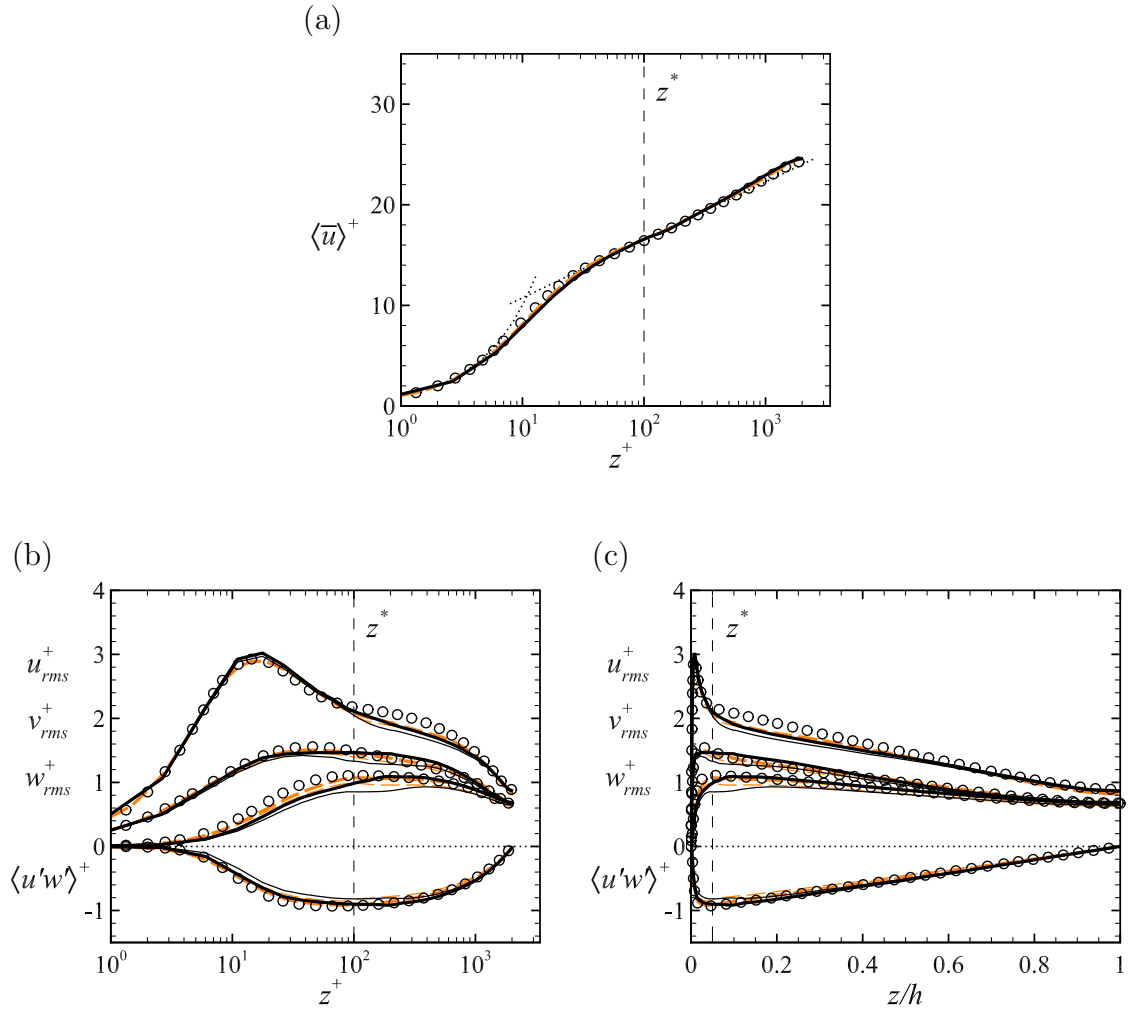

Figure 4.2: Profiles of mean velocity, turbulence intensities, and Reynolds shear stresses predicted by nested-LES in equilibrium turbulent channel flow at $Re_\tau \approx 2000$, compared to DNS data. Lines as in Figure 4.1; – – – (color in PDF format), nested-LES cases of 2000^h, performed at high resolution; ○, DNS of *Hoyas and Jimenez* (2006) at $Re_\tau \approx 2000$.

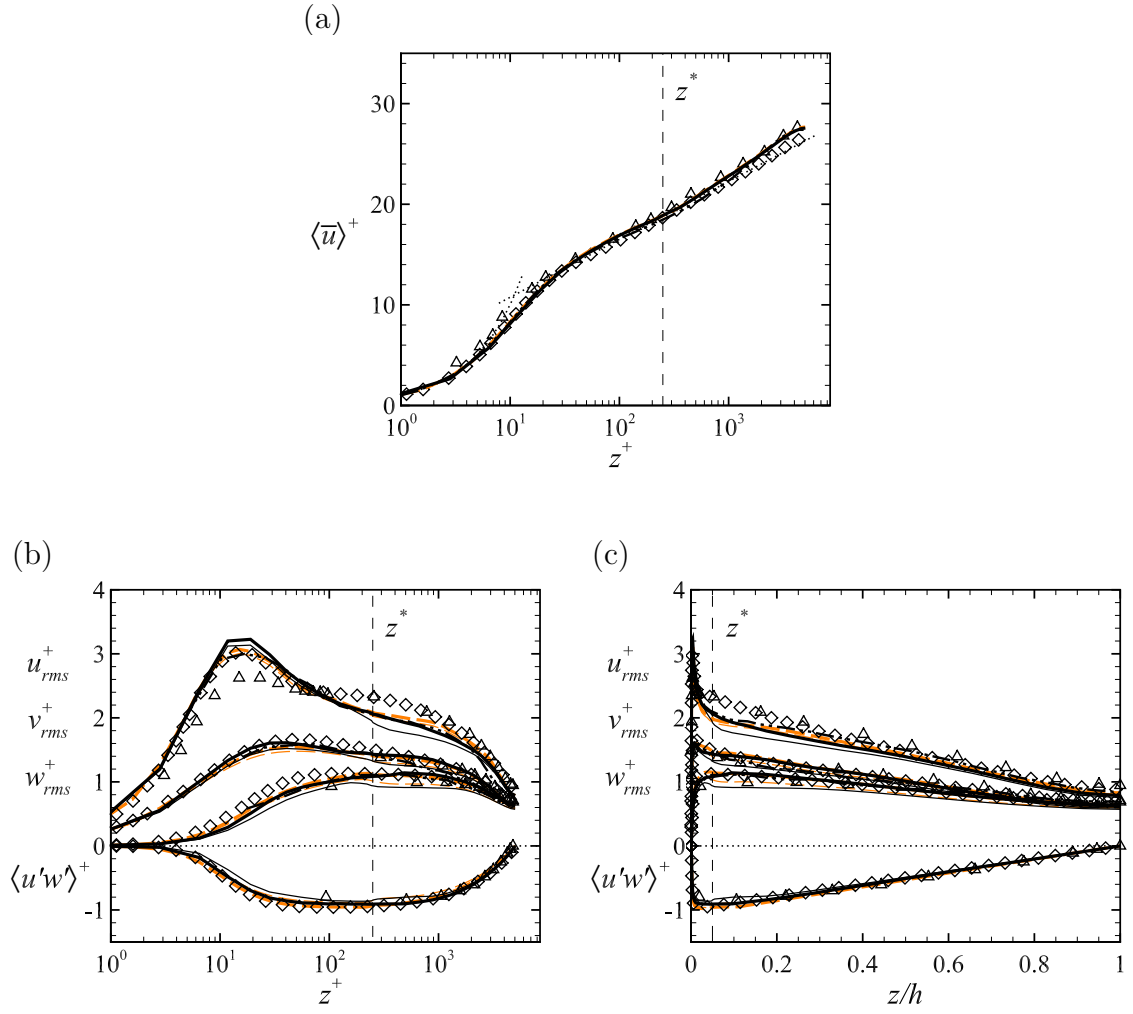

Figure 4.3: Profiles of mean velocity, turbulence intensities, and Reynolds shear stresses predicted by nested-LES in equilibrium turbulent channel flow at $Re_\tau \approx 5000$, compared to DNS, LES and experimental data. Lines as in Figure 4.1; – – – (color in PDF format), nested-LES cases of 5000^h, performed at high resolution; ◇, DNS of *Lee and Moser* (2015) at $Re_\tau \approx 5200$; △, experiments of *Comte-Bellot* (1963) at $Re_\tau \approx 4800$; –··–, LES of *Kravchenko et al.* (1996) at $Re_\tau \approx 4000$.

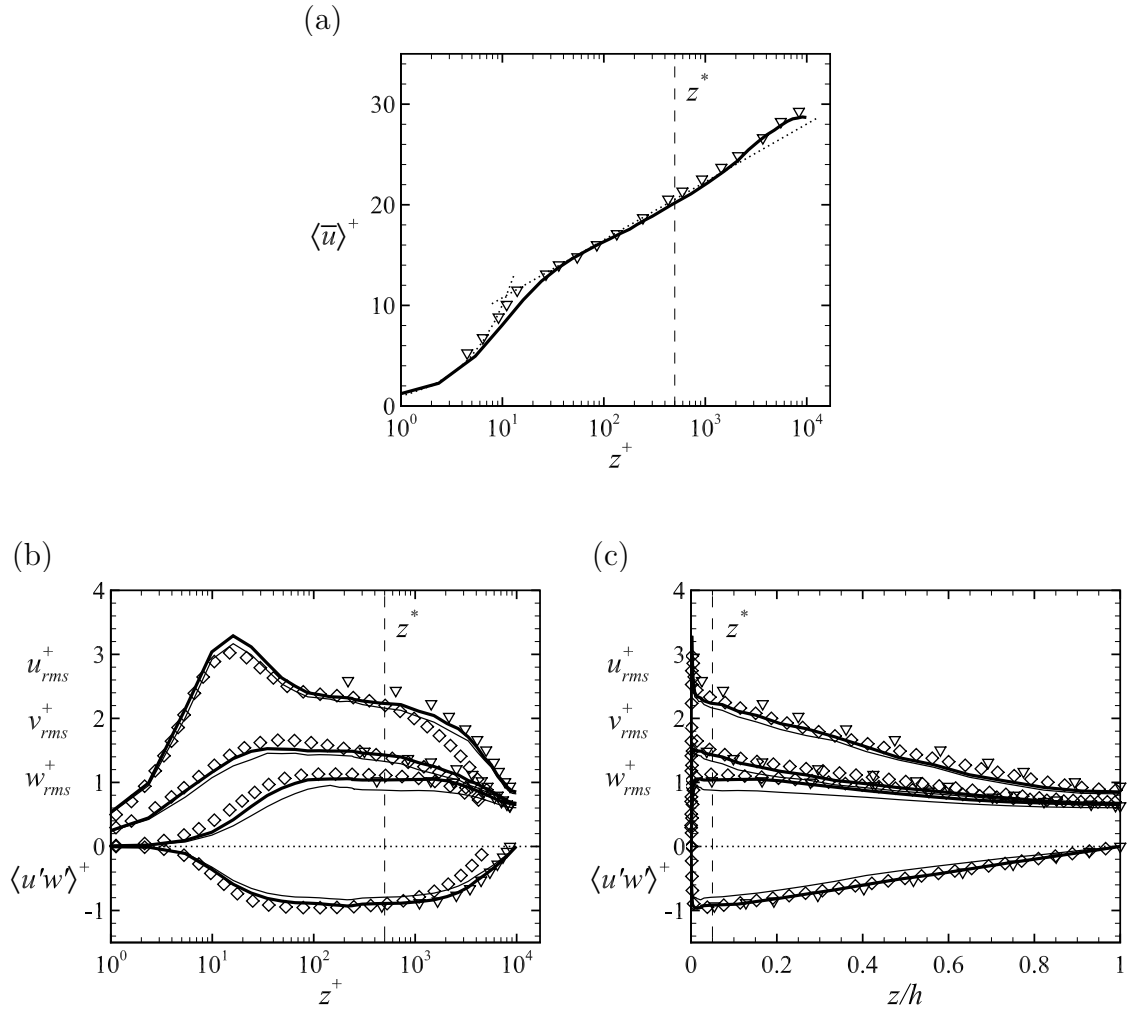

Figure 4.4: Profiles of mean velocity, turbulence intensities, and Reynolds shear stresses predicted by nested-LES in equilibrium turbulent channel flow at $Re_\tau \approx 10000$, compared to DNS and experimental data. Lines as in Figure 4.1; $\triangledown$, experiments of *Comte-Bellot* (1963) at $Re_\tau \approx 8600$; $\diamond$, DNS of *Lee and Moser* (2015) at $Re_\tau \approx 5200$.

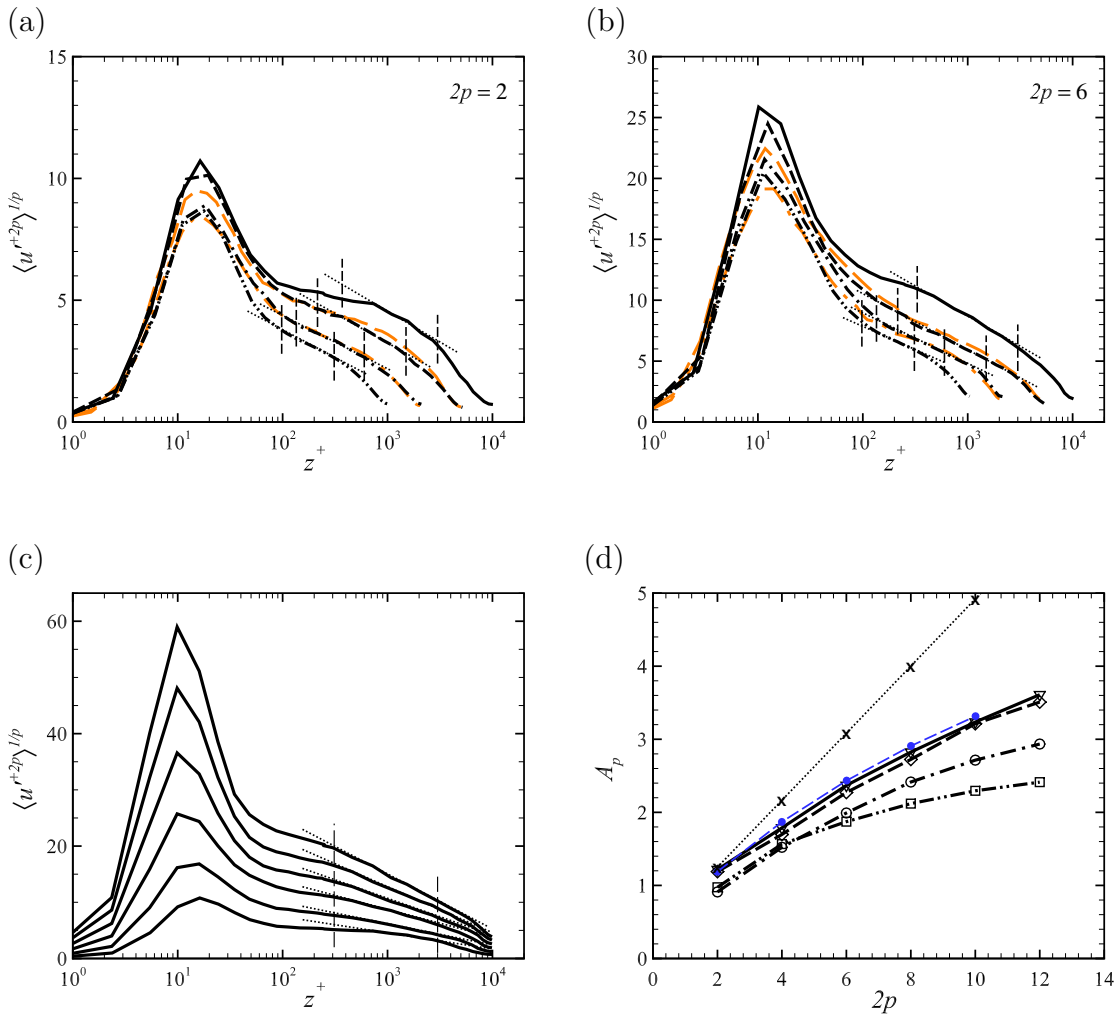

Figure 4.5: Moments of order (a) $2p = 2$, (b) $2p = 6$, (c) $2p = 2, 4, 6, 8, 10, 12$ (raised to the power of $1/p$) of streamwise velocity fluctuations, (d) coefficients A_p in the logarithmic law for moments as a function of the moment order $2p$, predicted by nested-LES at $1000 \leq Re_\tau \leq 10000$. $-\cdots-$, $Re_\tau \approx 1000$; $-\cdot-$, $Re_\tau \approx 2000$; $---$, $Re_\tau \approx 5000$; ——, $Re_\tau \approx 10000$; —·— (color in PDF format), $Re_\tau \approx 2000^h$ high-resolution; — — (color in PDF format), $Re_\tau \approx 5000^h$ high-resolution; $\cdots$, logarithmic fit to the region $3Re_\tau^{1/2} \leq z^+ \leq 0.3Re_\tau$; dashed vertical lines denote the bounds of the region $3Re_\tau^{1/2} \leq z^+ \leq 0.3Re_\tau$; $-\bullet-$ (blue in PDF format), experiments in TBL at $Re_\tau \approx 19030$ (*Meneveau and Marusic*, 2013); $\cdots\times\cdots$, Gaussian values for $A_p = A_1[(2p-1)!!]^{1/p}$ with $A_1 = 1.25$.

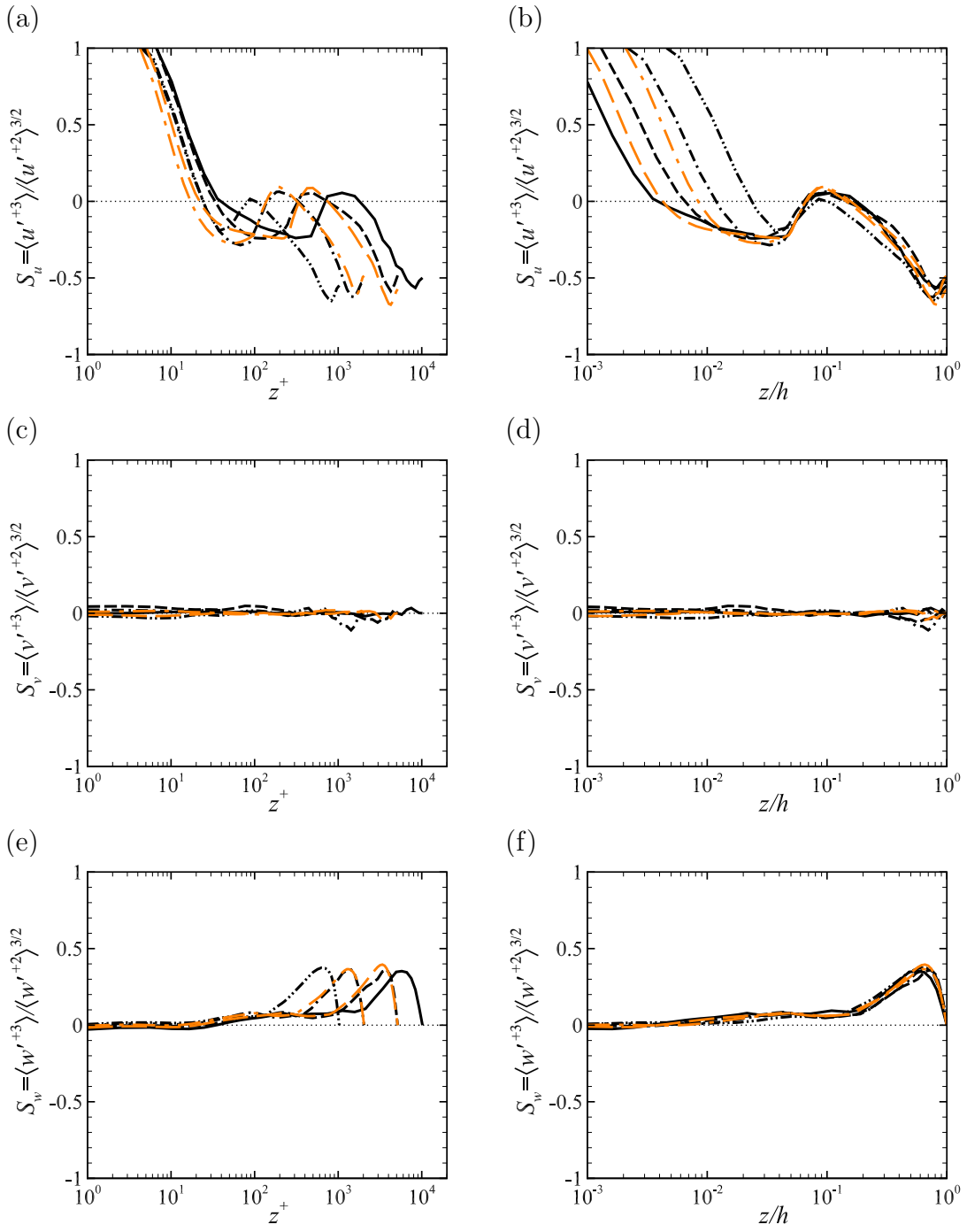

Figure 4.6: Skewness of (a,b) streamwise, (c,d) spanwise, and (e,f) wall-normal velocity fluctuations as functions of (a,c,e) z^+ and (b,d,f) z/h. Line types as in Figure 4.5.

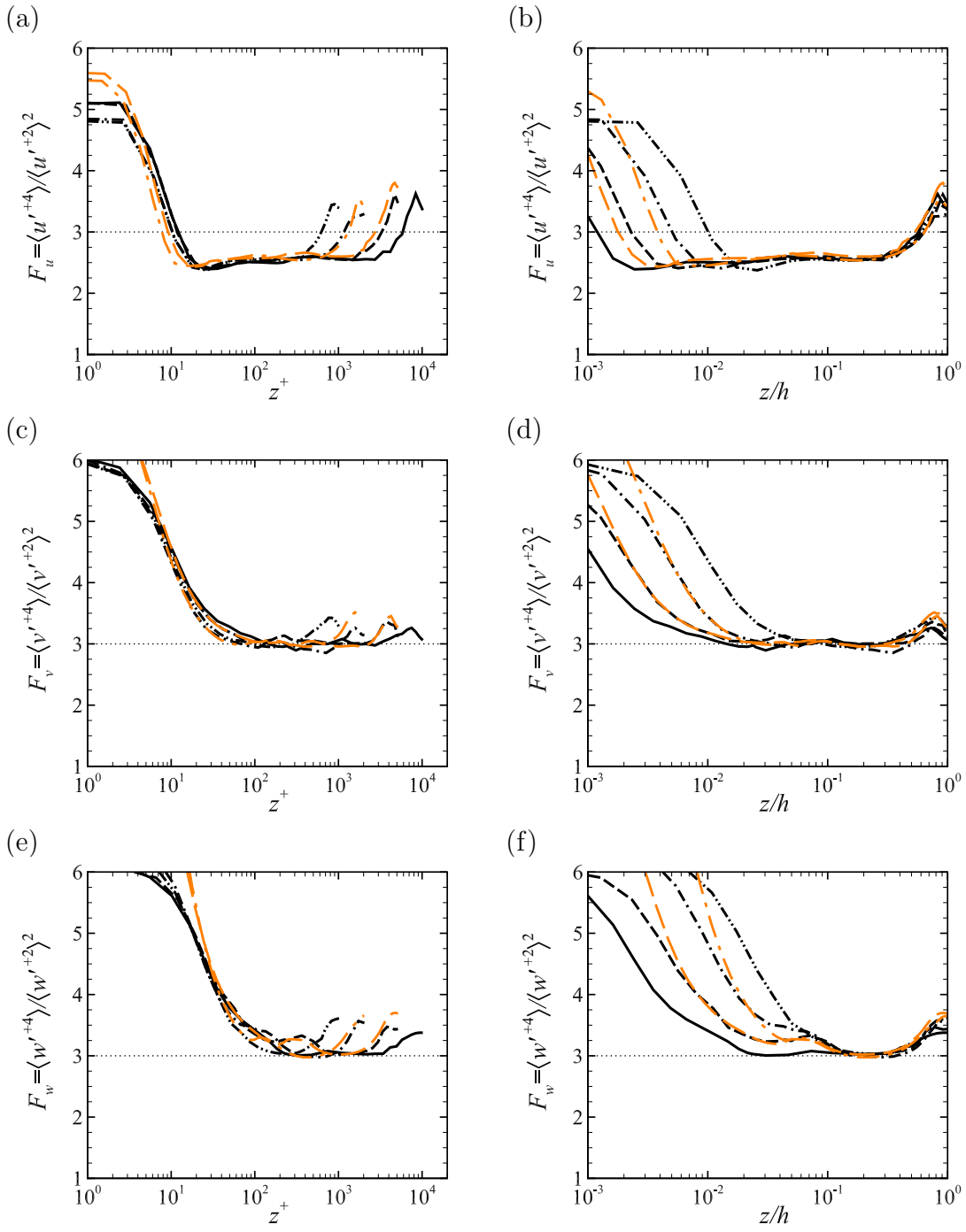

Figure 4.7: Flatness of (a,b) streamwise, (c,d) spanwise, and (e,f) wall-normal velocity fluctuations as functions of (a,c,e) z^+ and (b,d,f) z/h. Line types as in Figure 4.5.

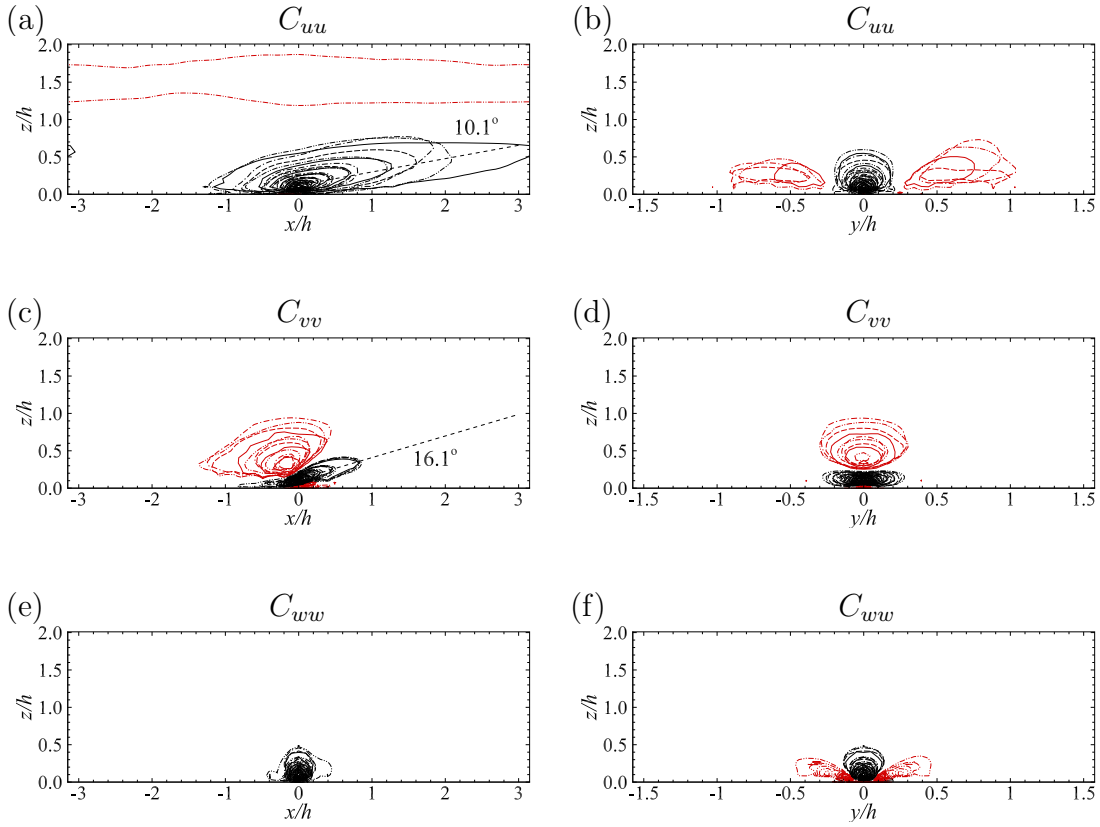

Figure 4.8: (a,c,e) Streamwise (xz) and (b,d,f) spanwise (yz) sections of the correlation maps of (a,b) C_{uu}, (c,d) C_{vv}, and (e,f) C_{ww}, predicted by nested-LES in equilibrium turbulent channel flow at $1000 \leq Re_\tau \leq 10000$ at $z/h = 0.1$. Line types as in Figure 4.5; black are positive contours at levels (0.1:0.1:0.9); red are negative contours at (-0.05:-0.05:-0.25), except in (f), where red are negative contours at (-0.01:-0.02:-0.09).

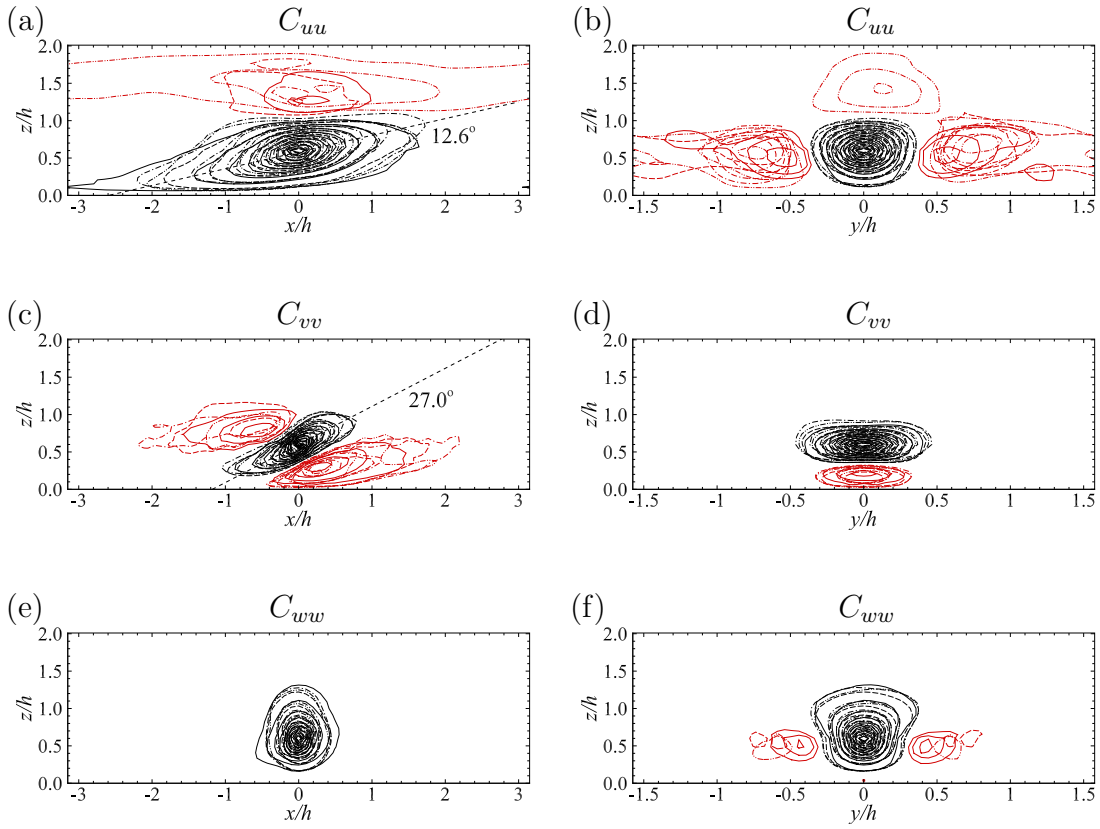

Figure 4.9: (a,c,e) Streamwise (xz) and (b,d,f) spanwise (yz) sections of the correlation maps of (a,b) C_{uu}, (c,d) C_{vv}, and (e,f) C_{ww}, predicted by nested-LES in equilibrium turbulent channel flow at $1000 \leq Re_\tau \leq 10000$ at $z/h = 0.6$. Line types as in Figure 4.5; contour levels and color as in Figure 4.8.

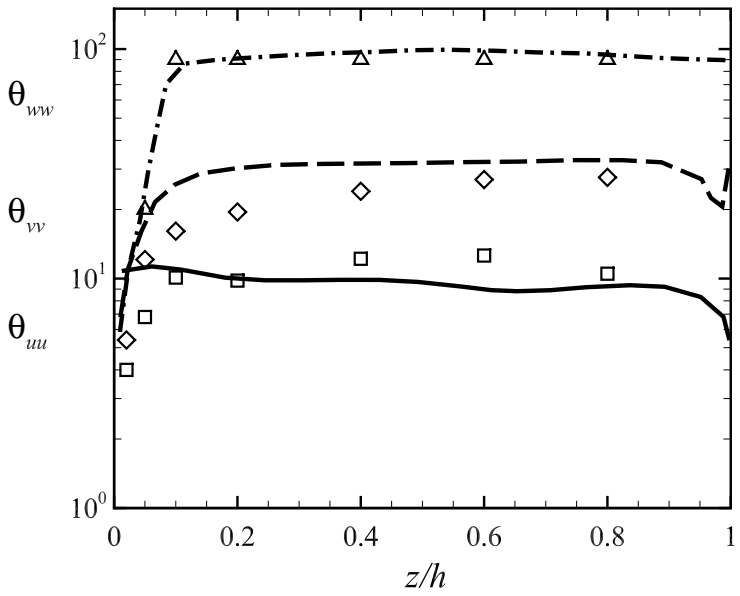

Figure 4.10: Inclination angles predicted by nested-LES in equilibrium turbulent channel flow at $1000 \leq Re_\tau \leq 10000$, compared to DNS data at $Re_\tau \approx 950$ (*del Alamo et al.*, 2004; *Sillero et al.*, 2014). □, ◇, △, inclination angles, θ_{uu}, θ_{vv}, θ_{ww}, respectively, predicted by nested-LES; ——, − − −, − · −, inclination angles, θ_{uu}, θ_{vv}, θ_{ww}, respectively, predicted by DNS.

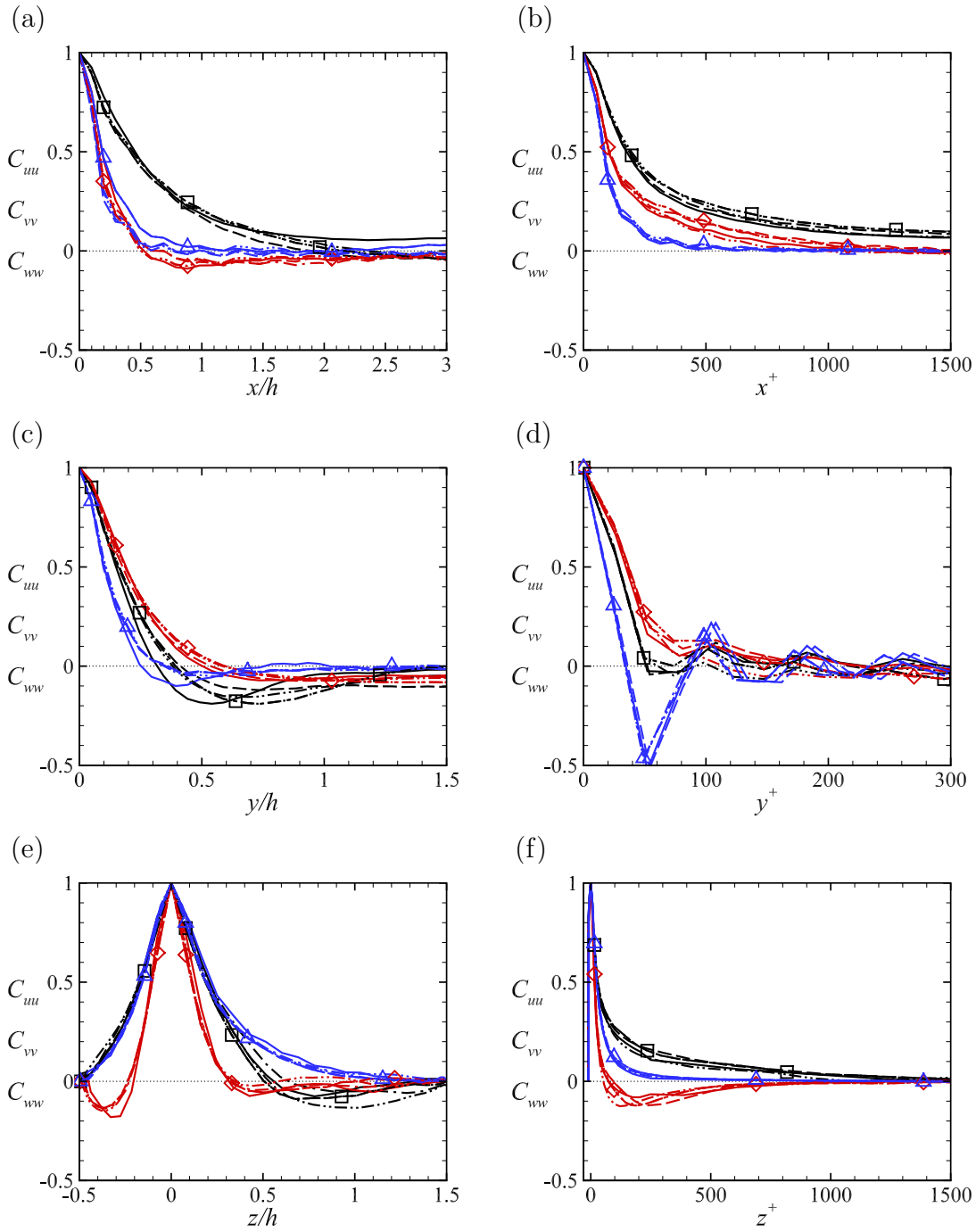

Figure 4.11: One-dimensional two-point correlations predicted by nested-LES in equilibrium turbulent channel flow at $1000 \leq Re_\tau \leq 10000$ in (a,c,e) outer region, $z/h \approx 0.5$, obtained from the full-domain; (b,d,f) near-wall region, $z^+ \approx 10$, obtained from the minimal flow unit. Line types as in Figure 4.5; lines with □ (black in PDF format), C_{uu}; lines with ◇ (red in PDF format), C_{vv}; lines with △ (blue in PDF format), C_{ww}.

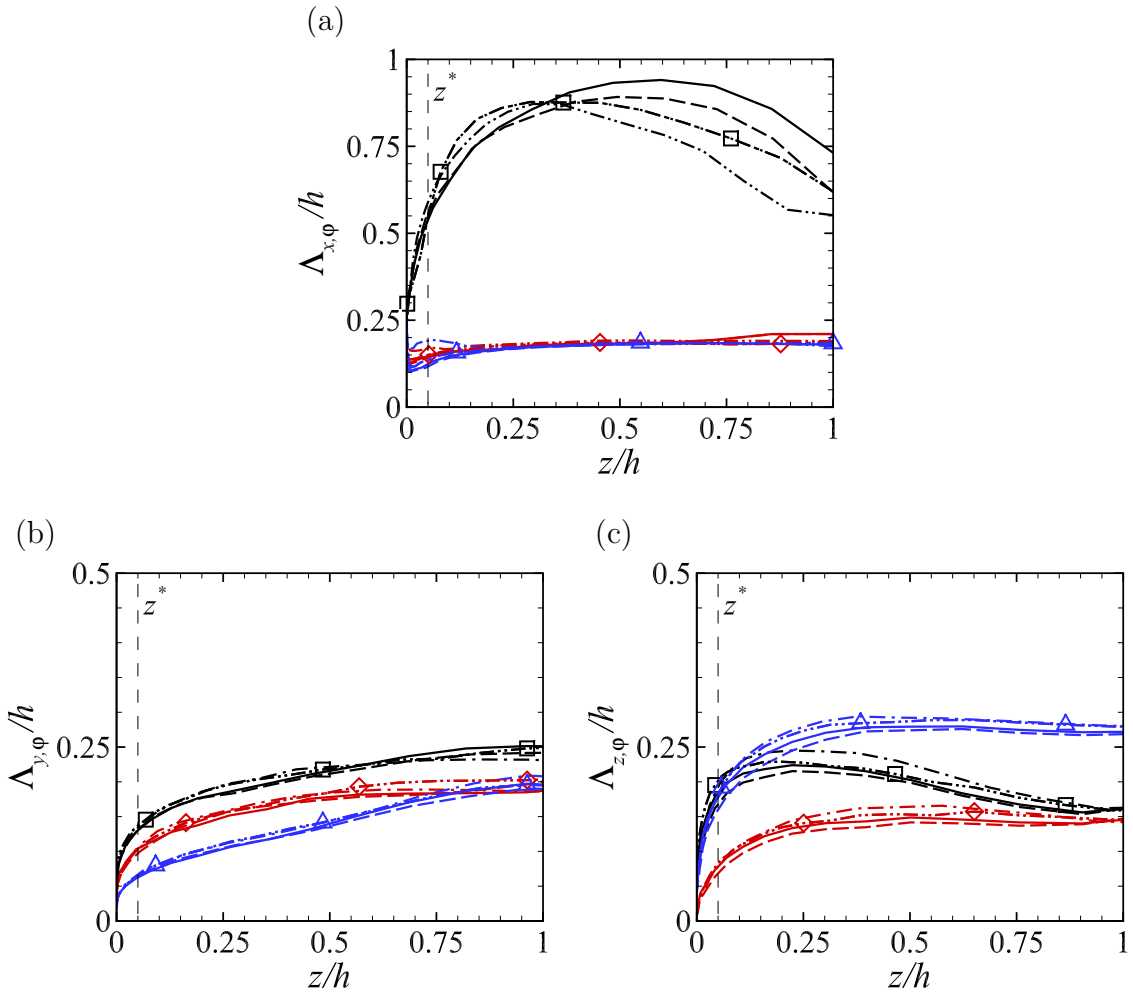

Figure 4.12: Integral scales, $\Lambda_{\alpha,\varphi}$, as a function z/h, predicted by nested-LES in equilibrium turbulent channel flow at $1000 \leq Re_\tau \leq 10000$. Line types as in Figure 4.5; lines with □ (black in PDF format), $\Lambda_{\alpha,u}$; lines with ◇ (red in PDF format), $\Lambda_{\alpha,v}$; lines with △ (blue in PDF format), $\Lambda_{\alpha,w}$.

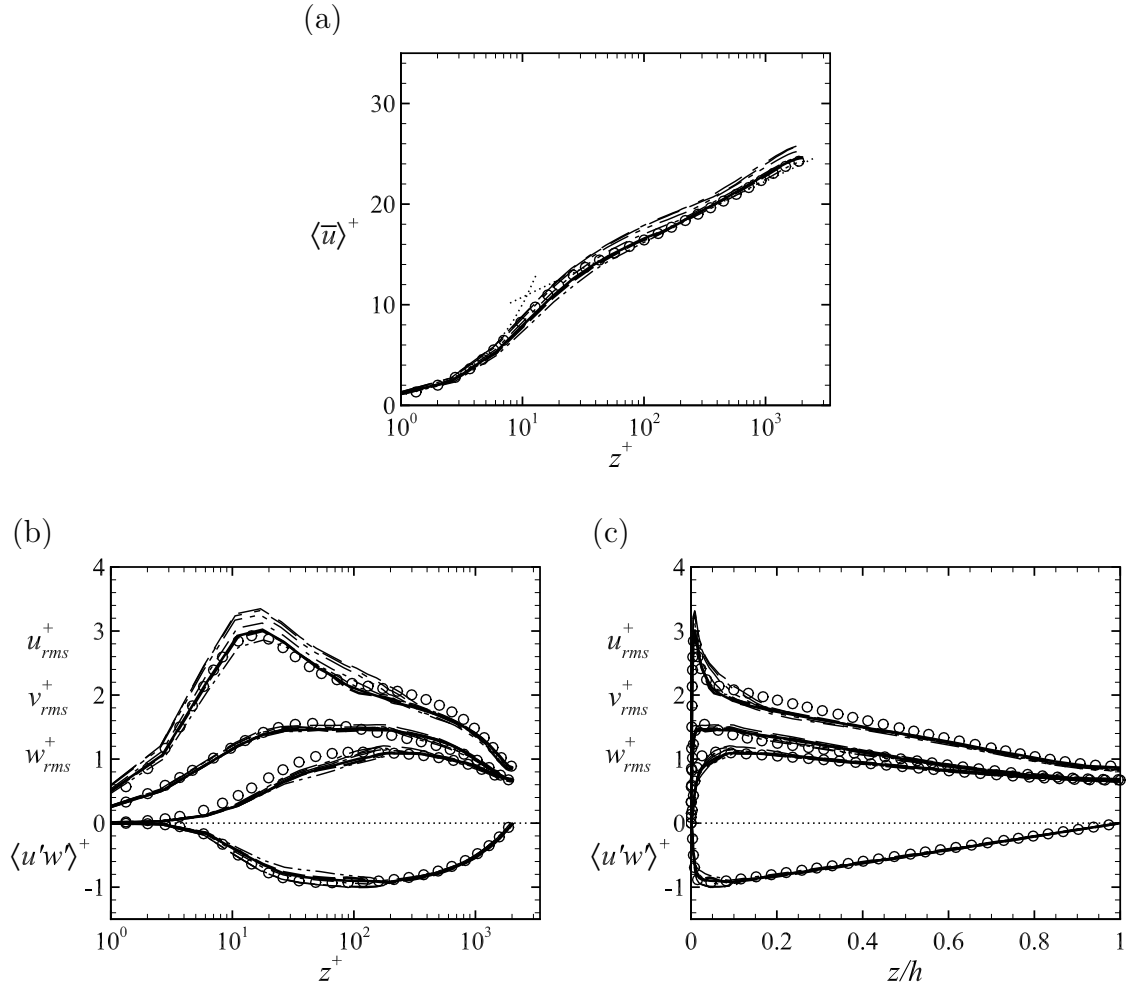

Figure 4.13: Profiles of mean velocity, turbulence intensities, and Reynolds shear stresses predicted by nested-LES in equilibrium turbulent channel flow at $Re_\tau \approx 2000$ with z^* placed at $-\cdot\cdot-$, $z^*/h = 0.025$; $--$, $z^*/h = 0.04$; ——, $z^*/h = 0.05$; $-\cdot-$, $z^*/h = 0.07$; —$\cdot\cdot$—, $z^*/h = 0.10$; —$\cdot$—, $z^*/h = 0.15$; — —, $z^*/h = 0.20$.

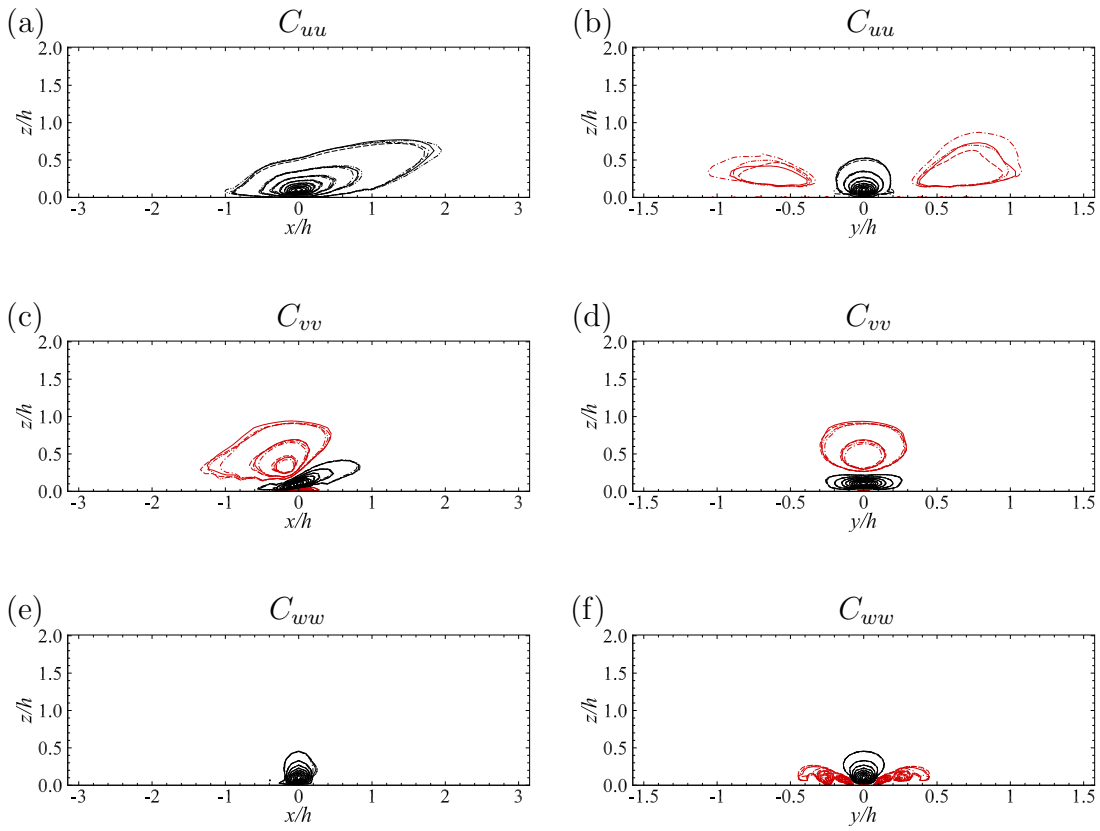

Figure 4.14: (a,c,e) Streamwise (xz) and (b,d,f) spanwise (yz) sections of the correlation maps of (a,b) C_{uu}, (c,d) C_{vv}, and (e,f) C_{ww} at $z/h = 0.1$, predicted by nested-LES in equilibrium turbulent channel flow at $Re_\tau \approx 2000$ with z^* placed at $z^*/h = 0.025$, 0.04, 0.05, and 0.07. Line types as in Figure 4.13; contour levels and color as in Figure 4.8.

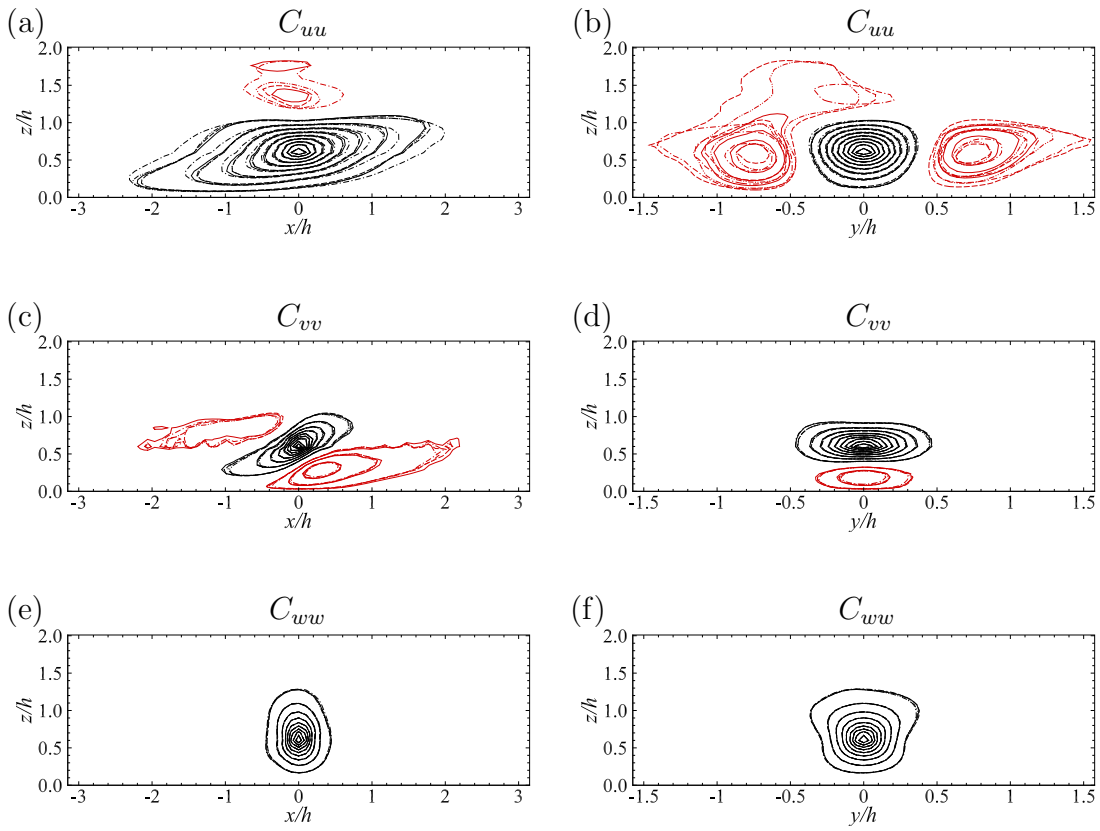

Figure 4.15: (a,c,e) Streamwise (xz) and (b,d,f) spanwise (yz) sections of the correlation maps of (a,b) C_{uu}, (c,d) C_{vv}, and (e,f) C_{ww} at $z/h = 0.6$, predicted by nested-LES in equilibrium turbulent channel flow at $Re_\tau \approx 2000$ with z^* placed at $z^*/h = 0.025$, 0.04, 0.05, and 0.07. Line types as in Figure 4.13; contour levels and color as in Figure 4.8.

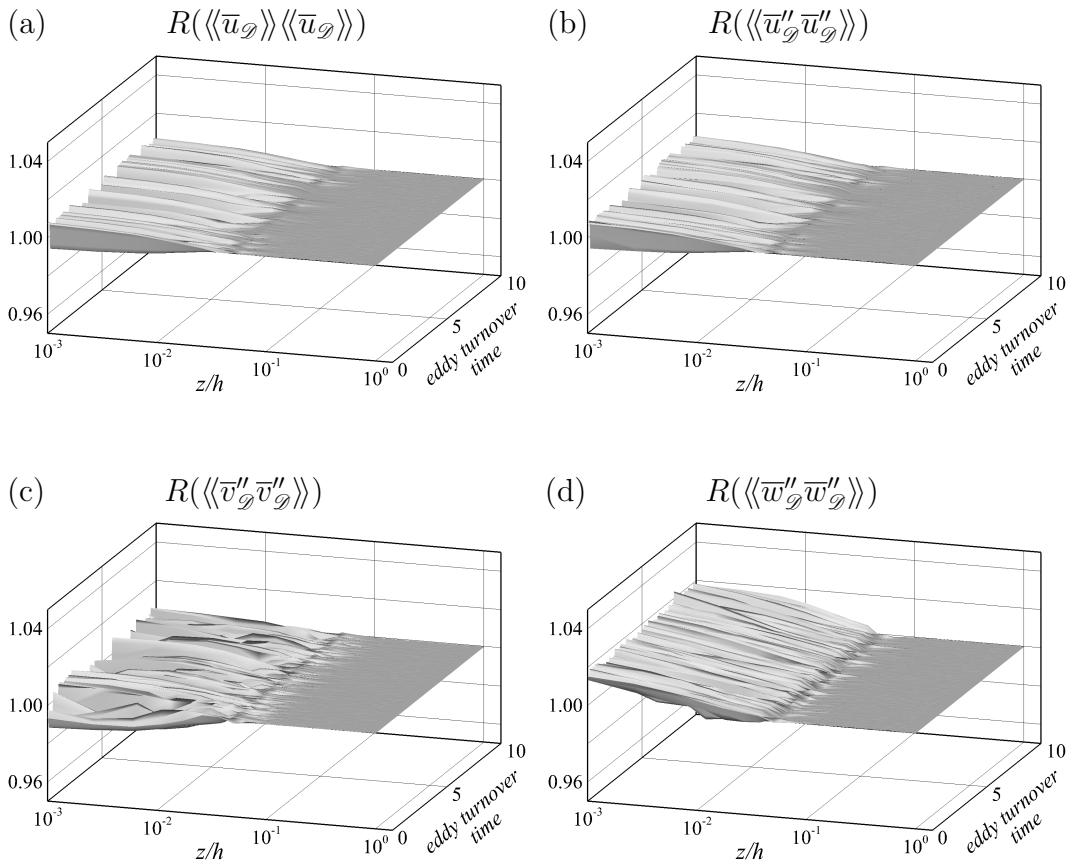

Figure 4.16: Time-history of the renormalization functions, $R(\phi_{\alpha,\mathscr{D}})$, as a function of z/h from nested-LES in equilibrium turbulent channel flow at $Re_\tau \approx 1000$ for (a) $\langle\langle\overline{u}_{\mathscr{D}}\rangle\rangle\langle\langle\overline{u}_{\mathscr{D}}\rangle\rangle$, (b) $\langle\langle\overline{u}''_{\mathscr{D}}\overline{u}''_{\mathscr{D}}\rangle\rangle$, (c) $\langle\langle\overline{v}''_{\mathscr{D}}\overline{v}''_{\mathscr{D}}\rangle\rangle$, and (d) $\langle\langle\overline{w}''_{\mathscr{D}}\overline{w}''_{\mathscr{D}}\rangle\rangle$.

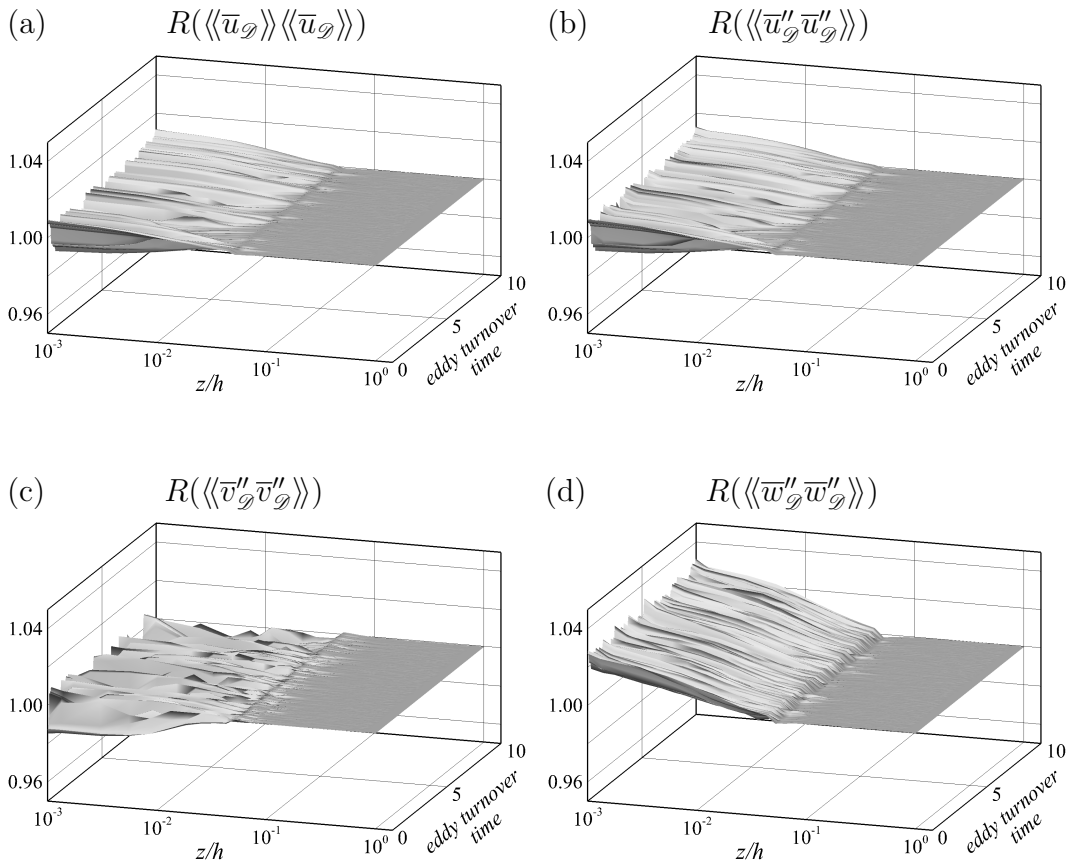

Figure 4.17: Time-history of the renormalization functions, $R(\phi_{\alpha,\mathscr{D}})$, as a function of z/h from nested-LES in equilibrium turbulent channel flow at $Re_\tau \approx 2000$ for (a) $\langle\langle\overline{u}_{\mathscr{D}}\rangle\rangle\langle\langle\overline{u}_{\mathscr{D}}\rangle\rangle$, (b) $\langle\langle\overline{u}''_{\mathscr{D}}\overline{u}''_{\mathscr{D}}\rangle\rangle$, (c) $\langle\langle\overline{v}''_{\mathscr{D}}\overline{v}''_{\mathscr{D}}\rangle\rangle$, and (d) $\langle\langle\overline{w}''_{\mathscr{D}}\overline{w}''_{\mathscr{D}}\rangle\rangle$.

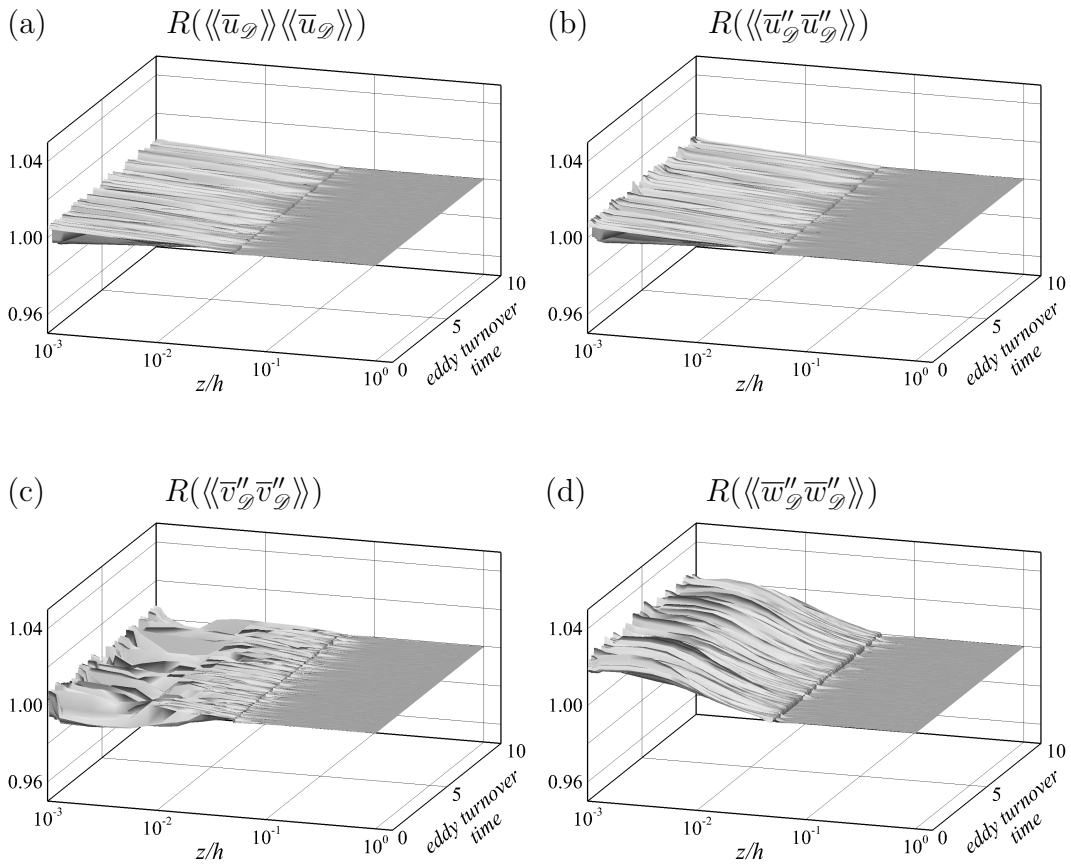

Figure 4.18: Time-history of the renormalization functions, $R(\phi_{\alpha,\mathscr{D}})$, as a function of z/h from nested-LES in equilibrium turbulent channel flow at $Re_\tau \approx 5000$ for (a) $\langle\langle\overline{u}_{\mathscr{D}}\rangle\rangle\langle\langle\overline{u}_{\mathscr{D}}\rangle\rangle$, (b) $\langle\langle\overline{u}''_{\mathscr{D}}\overline{u}''_{\mathscr{D}}\rangle\rangle$, (c) $\langle\langle\overline{v}''_{\mathscr{D}}\overline{v}''_{\mathscr{D}}\rangle\rangle$, and (d) $\langle\langle\overline{w}''_{\mathscr{D}}\overline{w}''_{\mathscr{D}}\rangle\rangle$.

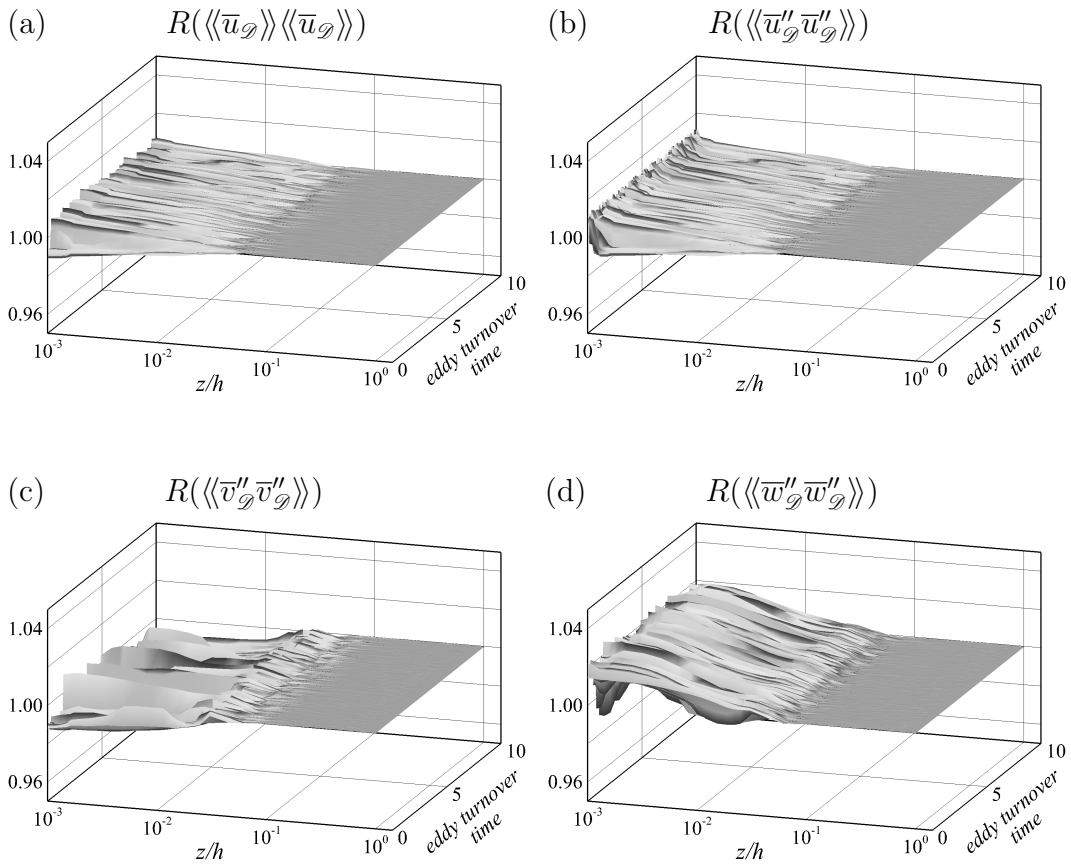

Figure 4.19: Time-history of the renormalization functions, $R(\phi_{\alpha,\mathscr{D}})$, as a function of z/h from nested-LES in equilibrium turbulent channel flow at $Re_\tau \approx 10000$ for (a) $\langle\langle\overline{u}_{\mathscr{D}}\rangle\rangle\langle\langle\overline{u}_{\mathscr{D}}\rangle\rangle$, (b) $\langle\langle\overline{u}''_{\mathscr{D}}\overline{u}''_{\mathscr{D}}\rangle\rangle$, (c) $\langle\langle\overline{v}''_{\mathscr{D}}\overline{v}''_{\mathscr{D}}\rangle\rangle$, and (d) $\langle\langle\overline{w}''_{\mathscr{D}}\overline{w}''_{\mathscr{D}}\rangle\rangle$.

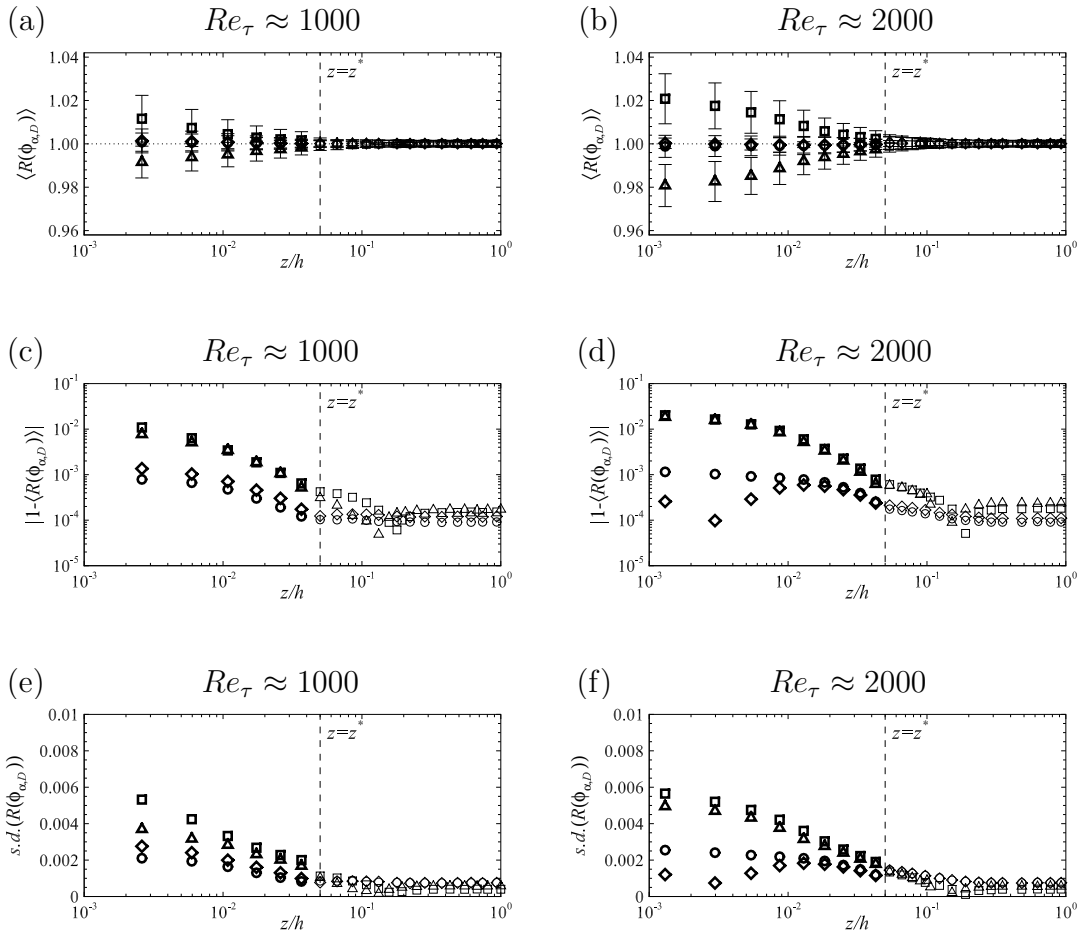

Figure 4.20: (a,b) Time-averaged renormalization functions, $\langle R(\phi_{\alpha,\mathscr{D}})\rangle$, (c,d) deviation of $\langle R(\phi_{\alpha,\mathscr{D}})\rangle$ from unity, and (e,f) standard deviations of $R(\phi_{\alpha,\mathscr{D}})$ in time from nested-LES in equilibrium turbulent channel flow at (a,c,e) $Re_\tau \approx 1000$ and (b,d,f) $Re_\tau \approx 2000$: ○, $R(\langle\langle\overline{u}_{\mathscr{D}}\rangle\rangle\langle\langle\overline{u}_{\mathscr{D}}\rangle\rangle)$; ◇, $R(\langle\langle\overline{u}''_{\mathscr{D}}\overline{u}''_{\mathscr{D}}\rangle\rangle)$; △, $R(\langle\langle\overline{v}''_{\mathscr{D}}\overline{v}''_{\mathscr{D}}\rangle\rangle)$; □, $R(\langle\langle\overline{w}''_{\mathscr{D}}\overline{w}''_{\mathscr{D}}\rangle\rangle)$; error bars in (a) are twice the standard deviation.

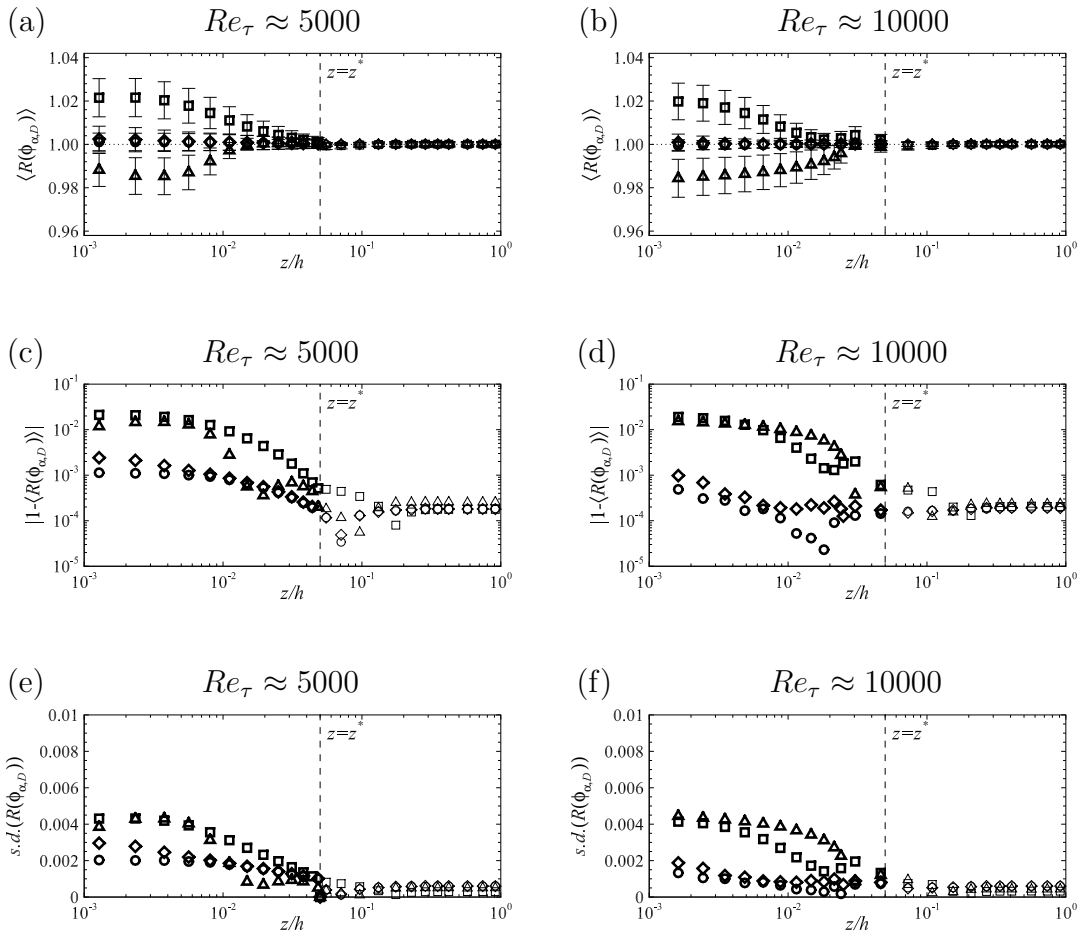

Figure 4.21: (a,b) Time-averaged renormalization functions, $\langle R(\phi_{\alpha,\mathscr{D}})\rangle$, (c,d) deviation of $\langle R(\phi_{\alpha,\mathscr{D}})\rangle$ from unity, and (e,f) standard deviations of $R(\phi_{\alpha,\mathscr{D}})$ in time from nested-LES in equilibrium turbulent channel flow at (a,c,e) $Re_\tau \approx 5000$ and (b,d,f) $Re_\tau \approx 10000$. Symbols as in Figure 4.20.

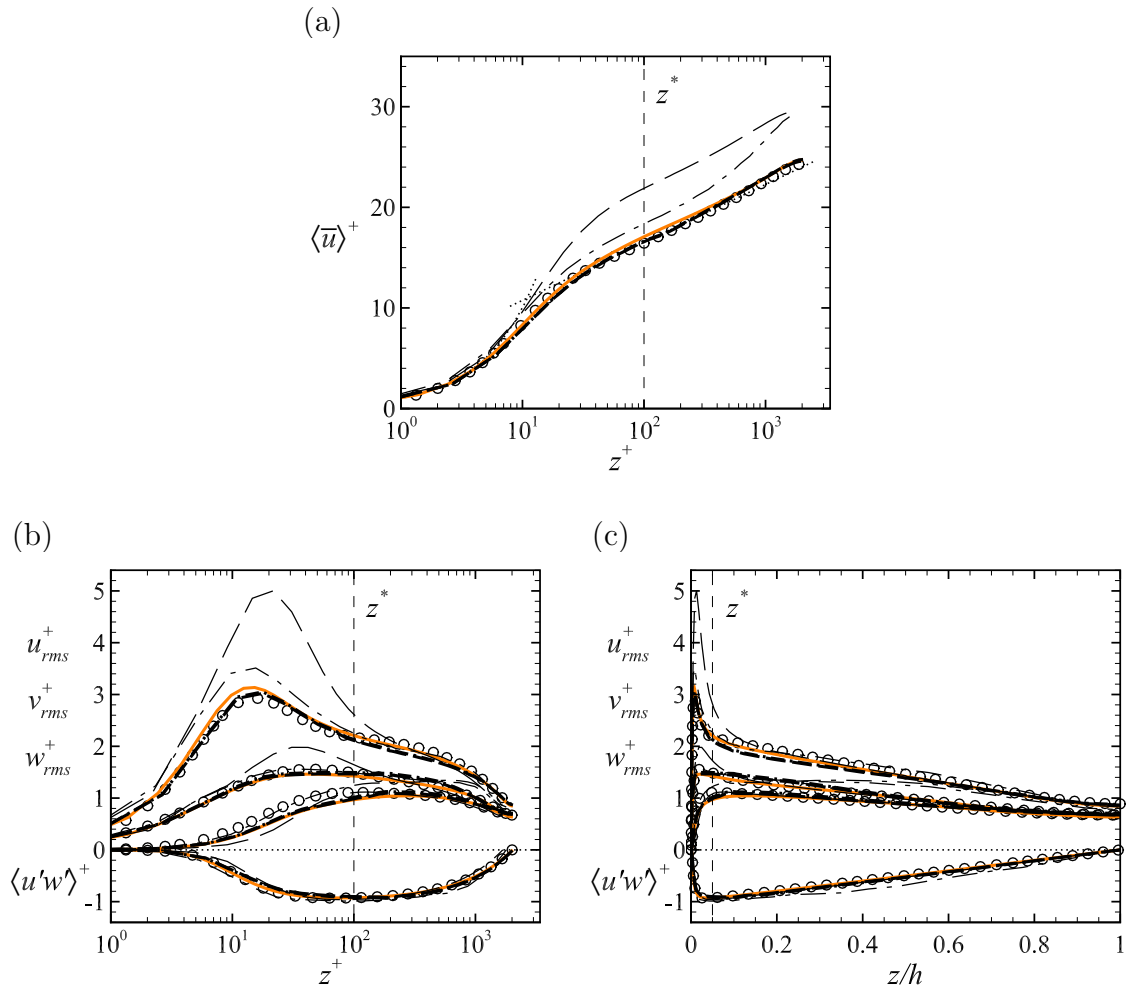

Figure 4.22: Profiles of mean velocity, turbulence intensities, and Reynolds shear stresses predicted by nested-LES and non-nested LES in equilibrium turbulent channel flow at $Re_\tau \approx 2000$: – – – (thick), full domain of nested-LES; – · – (thick), minimal flow unit of nested-LES; – – – (thin), non-nested LES in the full domain, case 2000^F; – · – (thin), non-nested LES in the minimal flow unit, case 2000^M; —— (color in PDF format), resolved conventional LES in the full domain, case $2000^{F,h}$; ○, DNS of *Hoyas and Jimenez* (2006) at $Re_\tau \approx 2000$.

CHAPTER V

Results in Non-Equilibrium, Strained Turbulent Channel Flow

As a further test of the nested-LES approach, its performance is assessed in non-equilibrium turbulent channel flow. In these studies, an initially equilibrium turbulent channel flow at $Re_\theta \approx 6900$ ($Re_\tau \approx 2000$) is driven to non-equilibrium by shear-driven strain introduced by impulsive transverse motion of a channel wall, followed by cessation of the transverse motion of the wall, and recovery to initial equilibrium state. The studies are designed to emulate the experimental conditions of *Driver and Hebbar* (1987, 1991), in which an initially two-dimensional TBL at $Re_\tau \approx 2000$ is driven to three-dimensionality by shear-driven strain introduced by impulsive transverse motion of the wall, followed by cessation of the transverse motion, and return to equilibrium two-dimensional TBL, as shown in Figure 3.3. In addition to nested-LES, non-nested LES are also performed in channels with the same domain size and grid resolution as those employed in the full domain and minimal flow unit of nested-LES. These nested-LES and non-nested LES cases are denoted by 2000-S, 2000-S^F, and 2000-S^M, in Table 3.1, respectively.

The evolution of the skin-friction coefficient and the one-point turbulence statistics predicted in these simulations are compared to experimental measurements during

the straining and recovery phases. The evolution of the flow quantities is tracked in position x^* in the TBL experiments and in time t^* in the simulations, and the correspondence between x^* and t^* is established using Taylor's hypothesis, as discussed in Section 3.3.

5.1 Evolution of Skin-friction Coefficients

Figures 5.1(a,b) show the evolution of the streamwise and spanwise skin-friction coefficients, $C_{f,x}$ and $C_{f,y}$, predicted in the simulations, compared to experimental measurements of *Driver and Hebbar* (1987, 1991). To allow a viable comparison between the skin-friction coefficients in the experiments and simulations, the streamwise and spanwise skin-friction coefficients in both flows are defined as $C_{f,x} \equiv \langle 2\tau_{w,x} \rangle / \rho U_\infty^2$ and $C_{f,y} \equiv \langle 2\tau_{w,y} \rangle / \rho U_\infty^2$, where U_∞ denotes either the free-stream velocity in the TBL experiments, or the mean centerline velocity in the base equilibrium turbulent channel flow in the simulations. Note that this is different from the conventional definition of the skin-friction coefficient in channel flow, which is normalized by the bulk velocity.

In the base equilibrium turbulent flow, $x^* \lesssim -32.6$, nested-LES predicts a $C_{f,x}$ in turbulent channel flow at $Re_\tau \approx 2000$ within 3% of the $C_{f,x}$ in two-dimensional TBL at $Re_\tau \approx 2000$, while $C_{f,y}$ in both flows is zero. Following the introduction of the transverse strain at $x^* \approx -32.6$, for $-32.6 \lesssim x^* \lesssim -28$, the $C_{f,x}$ predicted by nested-LES experiences a drop of ≈20%, followed by recovery to a value ≈ 20% higher than that in the base equilibrium flow, while $C_{f,y}$ experiences a sharp spike but rapidly settles to a magnitude comparable to $C_{f,x}$. For the rest of the straining zone, $-28 \lesssim x^* < 0$, the flow gradually settles into a new equilibrium state, in which both $C_{f,x}$ and $C_{f,y}$ become nearly constant and comparable in magnitude. Upon the removal of the transverse strain at $x^* = 0$, the $C_{f,x}$ predicted by nested-LES experiences a rapid drop of ≈10% for $0 \leq x^* \lesssim 0.15$, followed by recovery to a value comparable to the $C_{f,x}$

at the end of the straining zone, for $0.15 \lesssim x^* \lesssim 0.5$, and final gradual decay towards its base equilibrium channel value, for $0.5 \lesssim x^* \lesssim 20$. Meanwhile, $C_{f,y}$ experiences another spike accompanied by a change of sign at $x^* = 0$, followed by rapid decay to $\approx$20% of its value at the end of the straining zone, for $0 \leq x^* \lesssim 4$, and more gradual final decay towards its zero base equilibrium channel value, for $4 \lesssim x^* \lesssim 20$. Good overall agreement is observed between the $C_{f,x}$ and $C_{f,y}$ predicted by nested-LES and experimental data in the recovery zone, where experimental measurements are available. The biggest discrepancy is observed in the region $0 \leq x^* \lesssim 6$, where the initial rapid drop, recovery, and subsequent gradual decay of $C_{f,x}$ predicted by nested-LES occurs faster than experiments. These differences can be attributed to the more abrupt cessation of the transverse motion of the wall in the simulations compared to experiments. No experimental measurements of $C_{f,x}$ and $C_{f,y}$ are available in the straining zone, $-32.6 \lesssim x^* < 0$. However, the features observed in nested-LES are similar to those reported in previous DNS studies of strained turbulent channel flow (*Coleman et al.*, 1996), and LES of three-dimensional shear-driven TBL flow (*Kannepalli and Piomelli*, 2000) at lower Reynolds numbers.

The non-nested LES case of 2000-S^F exhibits significant lag in response to both the impulsive start and cessation of straining, and under-predicts the magnitudes of $C_{f,x}$ and $C_{f,y}$ by 50% in the straining zone, and by 10–20% in the initial equilibrium and final recovery zones, compared to experiments and nested-LES predictions. The non-nested LES case of 2000-S^M predicts the evolution of $C_{f,x}$ and $C_{f,y}$ with features similar to those in nested-LES, but under-predicts the $C_{f,x}$ and $C_{f,y}$ by 10–15%, compared to experiments and nested-LES predictions.

Figure 5.1(c) shows the evolution of the surface flow angle on the moving wall, defined as $\beta \equiv \tan^{-1}(C_{f,y}/C_{f,x})$. Nearly identical surface flow angles are predicted by nested-LES and non-nested LES cases of 2000-S^F and 2000-S^M, all showing good

agreement with experimental data in the recovery zone. The largest discrepancies from experiments are seen for case 2000-S^F.

5.2 Evolution of Turbulence Statistics in the Straining Zone

Figures 5.2–5.4 show the profiles of the mean velocities and turbulent stresses predicted by the simulations compared to experiments (*Driver and Hebbar*, 1987, 1991), at three stations, $x^* \approx -10.9$, -5.4, and -0.11, near the end of the straining zone, where experimental data is available. The strained flow has reached a new near-equilibrium state at both these stations, as evidenced by the near-constant values of $C_{f,x}$ and $C_{f,y}$ at these locations in Figure 5.1. Accordingly, nearly identical turbulence statistics are observed at both these stations in Figures 5.3–5.4.

The mean streamwise velocity, $\langle\overline{u}\rangle$, predicted by nested-LES, exhibits a small deficit in the region $0.1 \lesssim z/\delta(x) \lesssim 0.5$ compared to the $\langle\overline{u}\rangle$ in the base equilibrium flow, consistent with experimental observations by *Kiesow and Plesniak* (2003). The mean spanwise velocity, $\langle\overline{v}\rangle$, develops a profile which approximately satisfies $\langle\overline{v}\rangle/V_s = 1 - \langle\overline{u}\rangle/U_\infty$, as shown in Figure 5.5. Deviations of LES and experimental data from the line $\langle\overline{v}\rangle/V_s + \langle\overline{u}\rangle/U_\infty = 1$ are observed only in the outer layer, and here, the nested-LES results agree with experiments, while the non-nested LES cases of 2000-S^F and 2000-S^M both over-estimate the deviations due to their under-prediction of $\langle\overline{v}\rangle$.

The presence of this mean spanwise velocity leads to significant enhancement of all components of turbulent stresses in the strained flow compared to the base equilibrium flow, as seen in Figures 5.2–5.4. In the region $0 \leq z/\delta(x) \lesssim 0.7$, spanwise turbulent stress, $\langle v'v'\rangle$, predicted by nested-LES attains a magnitude comparable to $\langle u'u'\rangle$, while $\langle u'u'\rangle$ and $\langle w'w'\rangle$ are enhanced by 25% and 100% compared to their base equilibrium flow values, respectively. Furthermore, the wall-normal turbulent stress

$\langle w'w' \rangle$ develops a distinctive 'kink' in the region $z/\delta(x) \lesssim 0.1$, which is also reflected in the profiles of $\langle u'w' \rangle$ and $\langle v'w' \rangle$. The reorientation of the flow also gives rise to a non-zero Reynolds stress $\langle u'v' \rangle$, with a profile which is comparable in shape to $\langle v'v' \rangle$, but ≈50% smaller in magnitude. The Reynolds shear stress $\langle u'w' \rangle$ is enhanced by 15–50% in the outer layer compared to its value in the base equilibrium flow, while $\langle v'w' \rangle$, originally zero in the base equilibrium flow, develops a profile comparable in shape and magnitude to that of $\langle u'w' \rangle$. All these predictions of nested-LES in the straining zone are in agreement with experimental data. The biggest discrepancy between experiments and nested-LES results is observed in the profile of $\langle v'w' \rangle$ at $x^* \approx -0.11$, as shown in Figure 5.4(h), where experimental data show features which are characteristic of the recovery zone, $x^* \geq 0$.

In contrast, the non-nested LES case of 2000-S^F gives inaccurate predictions for all turbulent stresses as well as the mean spanwise velocity in both the inner and outer layers, while the non-nested LES case of 2000-S^M gives acceptable results in the inner layer but predicts inaccurate turbulent stresses in the outer layer.

5.3 Evolution of Turbulence Statistics in the Recovery Zone

Figures 5.6–5.8 show the evolution of the profiles of mean velocities and turbulent stresses predicted by nested-LES, compared to experiments (*Driver and Hebbar*, 1987, 1991), at $x^* \approx 0.11$, 0.23, and 0.45, in the initial recovery zone. In this initial recovery zone, the effect of the abrupt cessation of the transverse motion of the wall remains confined to the near-wall region, and is most dramatically felt in the spanwise component of the velocity. Both $\langle \overline{v} \rangle$ and $\langle v'v' \rangle$ rapidly decay during this phase, with their peaks values dropping to 40% and 50% of their respective peak values at the end of the straining zone. The cessation of the transverse motion of the wall also leads to positive values of the slope $d\langle \overline{v} \rangle / dz$ in the immediate vicinity of the wall, which

gives rise to a negative Reynolds shear stress, $\langle v'w' \rangle$, in the same region, as shown in Figures 5.6(b,h), 5.7(b,h), and 5.8(b,h). The rapid decay of $\langle v'v' \rangle$, combined with the skewed orientation of the mean flow, also gives rise to negative $\langle u'v' \rangle$ stresses in the near-wall region for $x^* \gtrsim 0.23$. At the start of the recovery zone, the near-wall peak of $\langle u'u' \rangle$ drops, reaching 70% of its value in the base equilibrium flow at $x^* \approx 0.23$, but recovers to 80% of its base flow value by $x^* \approx 0.45$. This initial drop in the peak of $\langle u'u' \rangle$ has also been observed in earlier DNS studies of strained channel flow (*Coleman et al.*, 1996) and LES of TBL flow (*Kannepalli and Piomelli*, 2000) at lower Reynolds numbers, and has been associated with the observed 'dip' in $C_{f,x}$ at the start of the recovery zone. The profile of the wall-normal turbulent stress, $\langle w'w' \rangle$, remains virtually unchanged from that at the end of the straining zone, while the 'kinks' in the near-wall region in the profiles of $\langle w'w' \rangle$, $\langle u'w' \rangle$, and $\langle v'w' \rangle$, observed in the straining zone, all become more pronounced. The nested-LES approach successfully captures all these features in agreement with experimental data. In contrast, the non-nested LES case of 2000-S^F exhibits significant lag in response to cessation of the transverse strain and fails to correctly predict any of the turbulent stresses or the mean spanwise velocity, while the non-nested LES case of 2000-S^M predicts the turbulent stresses inaccurately in the outer layer.

Figures 5.9–5.11 show the evolution of the profiles of the mean velocities and turbulent stresses predicted by nested-LES, compared to experiments (*Driver and Hebbar*, 1987, 1991), at $x^* \approx 0.9$, 1.8, and 3.6, in the mid-recovery zone. In this mid-recovery zone, $C_{f,x}$ begins to gradually decay towards its equilibrium value, while $C_{f,y}$ rapidly decays to 20% of its value at the end of the shearing zone, and the effect of cessation of straining begins to penetrate into the outer layer. The profiles of $\langle \overline{v} \rangle$, $\langle v'v' \rangle$ and $\langle w'w' \rangle$ continue to decay towards their equilibrium states in both the inner and outer layers, while the near-wall 'kinks' in $\langle w'w' \rangle$ and $\langle u'w' \rangle$ become

less pronounced, and $\langle u'w' \rangle$ becomes comparable in magnitude to that in the base equilibrium flow in the inner layer, while it continues to decay towards its equilibrium value in the outer layer.. The near-wall peak of $\langle u'u' \rangle$ continues to recover, reaching $\approx$90% of its peak value in the base equilibrium flow. The negative peaks of $\langle u'v' \rangle$ and $\langle v'w' \rangle$ gradually decay in the near-wall region, while $\langle u'v' \rangle$ and $\langle v'w' \rangle$ decay in the outer layer. The nested-LES approach successfully captures all these flow features in this mid-recovery zone in agreement with experimental data. The biggest discrepancy is observed in the profiles of $\langle w'w' \rangle$ and $\langle v'w' \rangle$, for which nested-LES predicts a faster decay compared to experiments. These discrepancies are attributed to the larger spanwise and wall-normal turbulence intensities in the outer layer of TBL compared to channel flow (*Jimenez et al.*, 2010). The non-nested LES case of 2000-S^F gives large errors in the prediction of all flow quantities, especially the turbulent stresses, in both the inner and outer layers, while case 2000-S^M gives poor predictions of the turbulent stresses in the outer layer.

Figures 5.12–5.14 show the evolution of the profiles of the mean velocities and turbulent stresses predicted by nested-LES, compared to experiments (*Driver and Hebbar*, 1987, 1991), at $x^* \approx 5.4$, 10.9, and 16.3, in the final recovery zone. In this final recovery zone, all turbulence statistics are approaching their equilibrium states. The predictions of nested-LES show good agreement with experimental data in this final recovery zone, as well. The biggest discrepancy is in the higher magnitudes of $\langle w'w' \rangle$ in the outer layer ($z/\delta(x) \geq 0.1$) and the slower approach of $\langle v'w' \rangle$ and $\langle u'w' \rangle$ towards their equilibrium values in experiments compared to the simulations. These are attributed to the stronger spanwise and wall-normal turbulence intensities in the outer layer of TBL compared to channel flow (*Jimenez et al.*, 2010), discussed earlier. The non-nested LES case of 2000-S^F predicts the turbulent stresses inaccurately throughout the cross-section of the channel, while the non-nested LES case of 2000-

S^M predicts inaccurate turbulent stresses in the outer layer.

5.4 Renormalization Factors in Nested-LES

Figure 5.15 shows the time history of the instantaneous renormalization functions from nested-LES of the non-equilibrium, strained turbulent channel flow in the straining zone and the recovery zone. In the recovery zone ($t^* \geq 0$), the renormalization functions are similar in shape as those in the equilibrium channel, except that $R(\langle\langle\overline{v}_{\mathscr{D}}\rangle\rangle\langle\langle\overline{v}_{\mathscr{D}}\rangle\rangle)$, which is not needed for the equilibrium channel case, is also reported here. However, near $t^* = 0$, an abrupt change of behavior is observed for the renormalization functions for $\langle\langle\overline{v}_{\mathscr{D}}\rangle\rangle\langle\langle\overline{v}_{\mathscr{D}}\rangle\rangle$ and $\langle\langle\overline{v}''_{\mathscr{D}}\overline{v}''_{\mathscr{D}}\rangle\rangle$.

This is further confirmed by the statistics of renormalization functions, $\langle R(\phi_{\alpha,\mathscr{D}})\rangle$, $|1-\langle R(\phi_{\alpha,\mathscr{D}})\rangle|$, and the standard deviations of $R(\phi_{\alpha,\mathscr{D}})$, shown in Figure 5.16. Overall, $\langle R(\phi_{\alpha,\mathscr{D}})\rangle$ varies between 1 ± 0.03 for $0 \leq z/h < 0.05$, and 1 ± 0.001 for $0.05 \leq z/h \leq 1$ throughout the straining and recovery zones. In the recovery region (Figures 5.16b,d,f), the statistics of $R(\phi_{\alpha,\mathscr{D}})$ agree with those predicted by nested-LES in equilibrium turbulent channel, except that $R(\langle\langle\overline{v}''_{\mathscr{D}}\overline{v}''_{\mathscr{D}}\rangle\rangle)$ remains closer to unity in the near-wall region and fluctuate less. In the straining zone (Figures 5.16a,c,e), $\langle R(\phi_{\alpha,\mathscr{D}})\rangle$ act to enhance the turbulence kinetic energy of both $\langle\langle\overline{v}_{\mathscr{D}}\rangle\rangle$ and $\overline{v}''_{\mathscr{D}}$ by up to 0.5% and 2%, respectively, instead of attenuating them by up to 0.5% and 2%, respectively, as in the recovery zone and in the equilibrium channel flow.

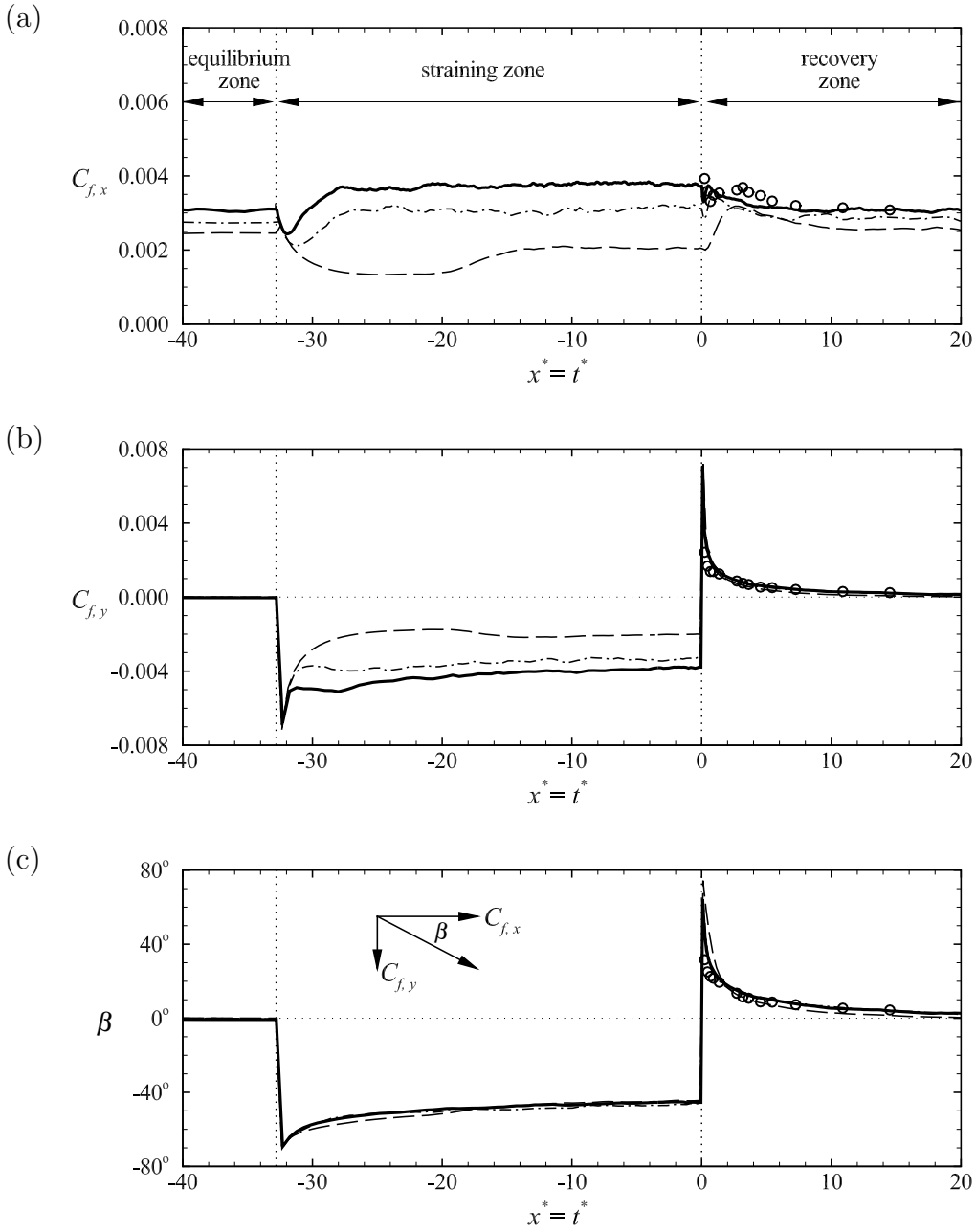

Figure 5.1: Evolution of (a) streamwise skin-friction coefficient, $C_{f,x}$, (b) spanwise skin-friction coefficient, $C_{f,y}$, and (c) surface-flow angle, β, predicted by nested-LES and non-nested LES in non-equilibrium, strained turbulent channel flow, compared to experiments (*Driver and Hebbar*, 1987, 1991). ——, nested-LES, case 2000-S; – – –, non-nested LES, case 2000-S^F; – · –, non-nested LES, case 2000-S^M; ○, experiments of *Driver and Hebbar* (1987, 1991).

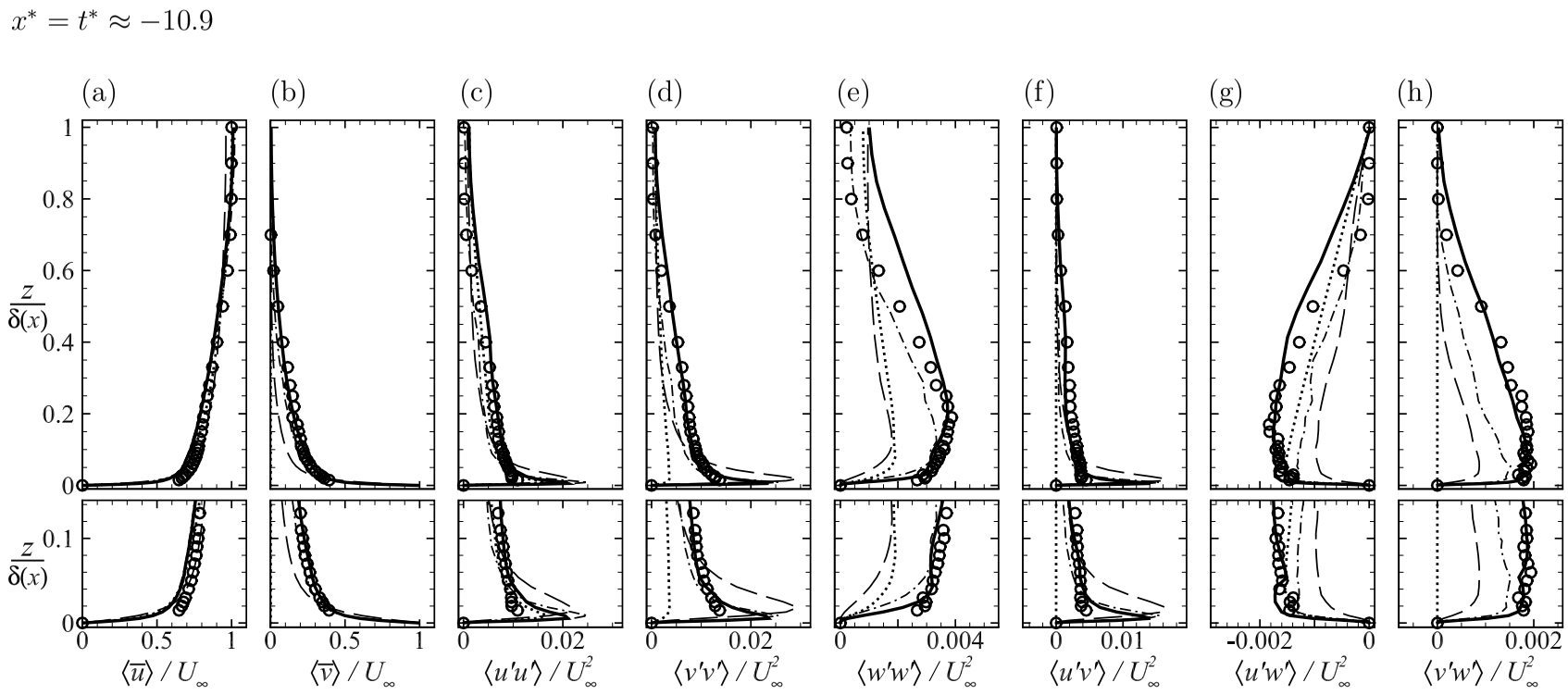

Figure 5.2: Profiles of mean velocities and turbulent stresses near the end of the straining zone predicted by nested-LES and non-nested LES in non-equilibrium, strained turbulent channel flow, compared to experimental measurements in shear-driven, three-dimensional TBL (*Driver and Hebbar*, 1987, 1991), at $x^* = t^* \approx -10.9$. ——, nested-LES, case 2000-S; – – –, non-nested LES, case 2000-S^F; – · –, non-nested LES, case 2000-S^M; · · · ·, nested-LES in equilibrium turbulent channel flow at $Re_\tau \approx 2000$; ○, experimental data of *Driver and Hebbar* (1987, 1991). An enlarged view of the near-wall region is shown below each figure.

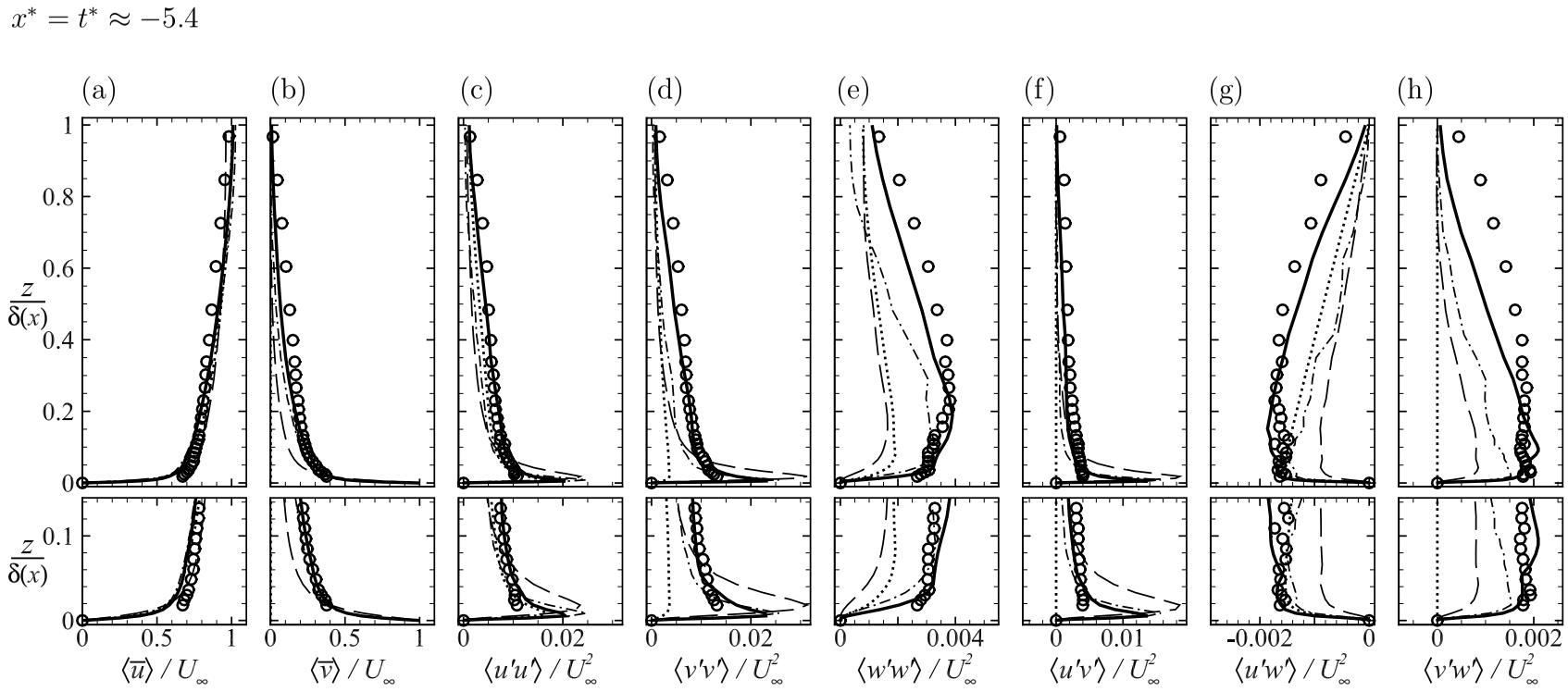

Figure 5.3: Profiles of mean velocities and turbulent stresses near the end of the straining zone predicted by nested-LES and non-nested LES in non-equilibrium, strained turbulent channel flow, compared to experimental measurements in shear-driven, three-dimensional TBL (*Driver and Hebbar*, 1987, 1991), at $x^* = t^* \approx -5.4$. Lines and symbols as in Figure 5.2.

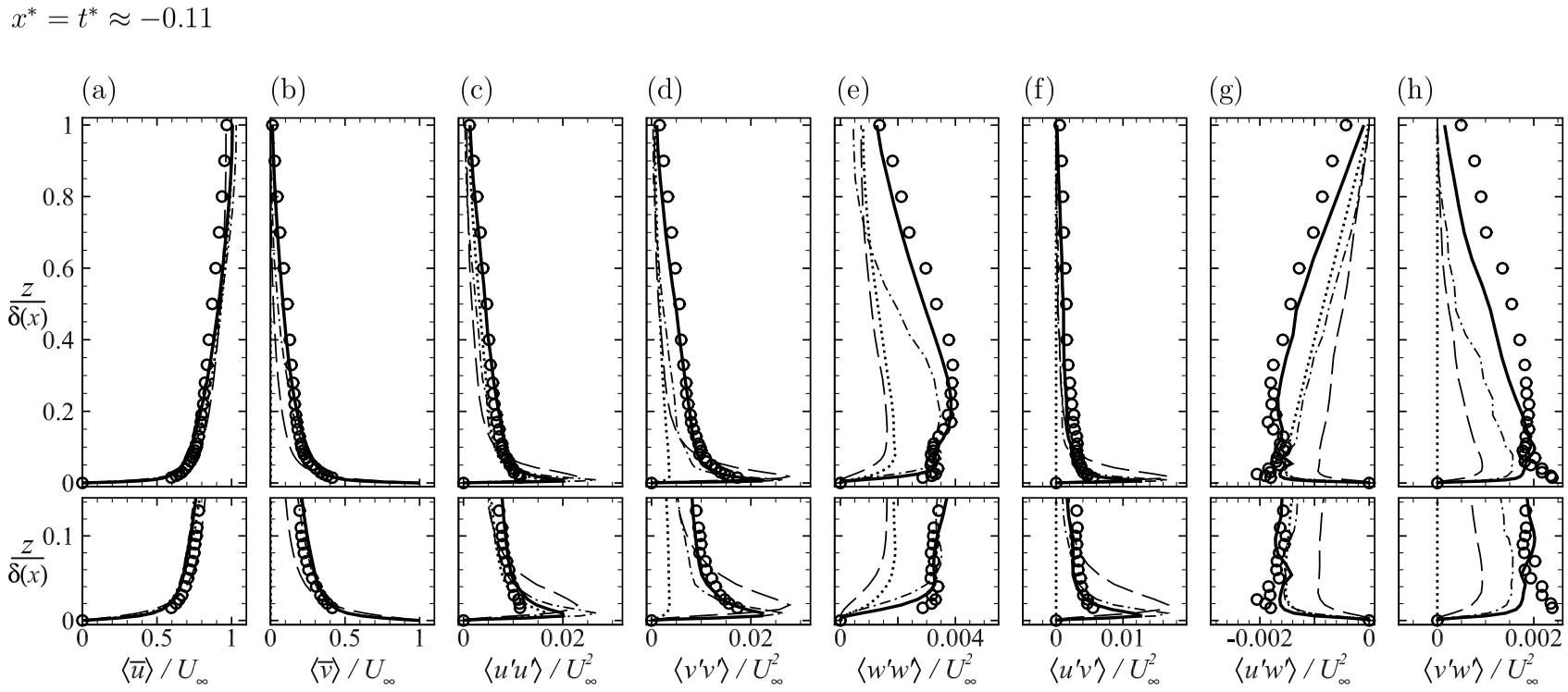

Figure 5.4: Profiles of mean velocities and turbulent stresses near the end of the straining zone predicted by nested-LES and non-nested LES in non-equilibrium, strained turbulent channel flow, compared to experimental measurements in shear-driven, three-dimensional TBL (*Driver and Hebbar*, 1987, 1991), at $x^* = t^* \approx -0.11$. Lines and symbols as in Figure 5.2.

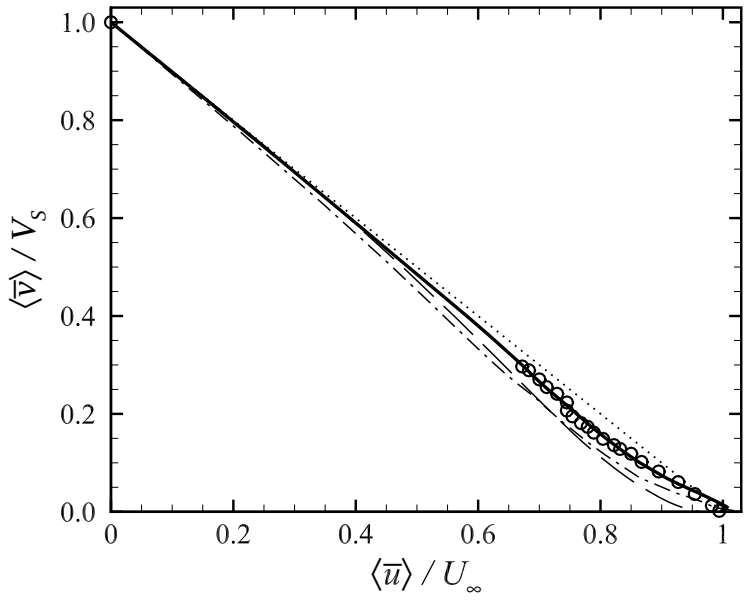

Figure 5.5: Hodograph of the mean streamwise and spanwise velocities at $x^* = t^* \approx -5.4$, near the end of the straining zone predicted by nested-LES and non-nested LES, compared to experiments (*Driver and Hebbar*, 1987, 1991). $\cdots$, analytical expression $\langle\overline{u}\rangle/U_\infty + \langle\overline{v}\rangle/V_s = 1$; other lines and symbols as in Figure 5.2.

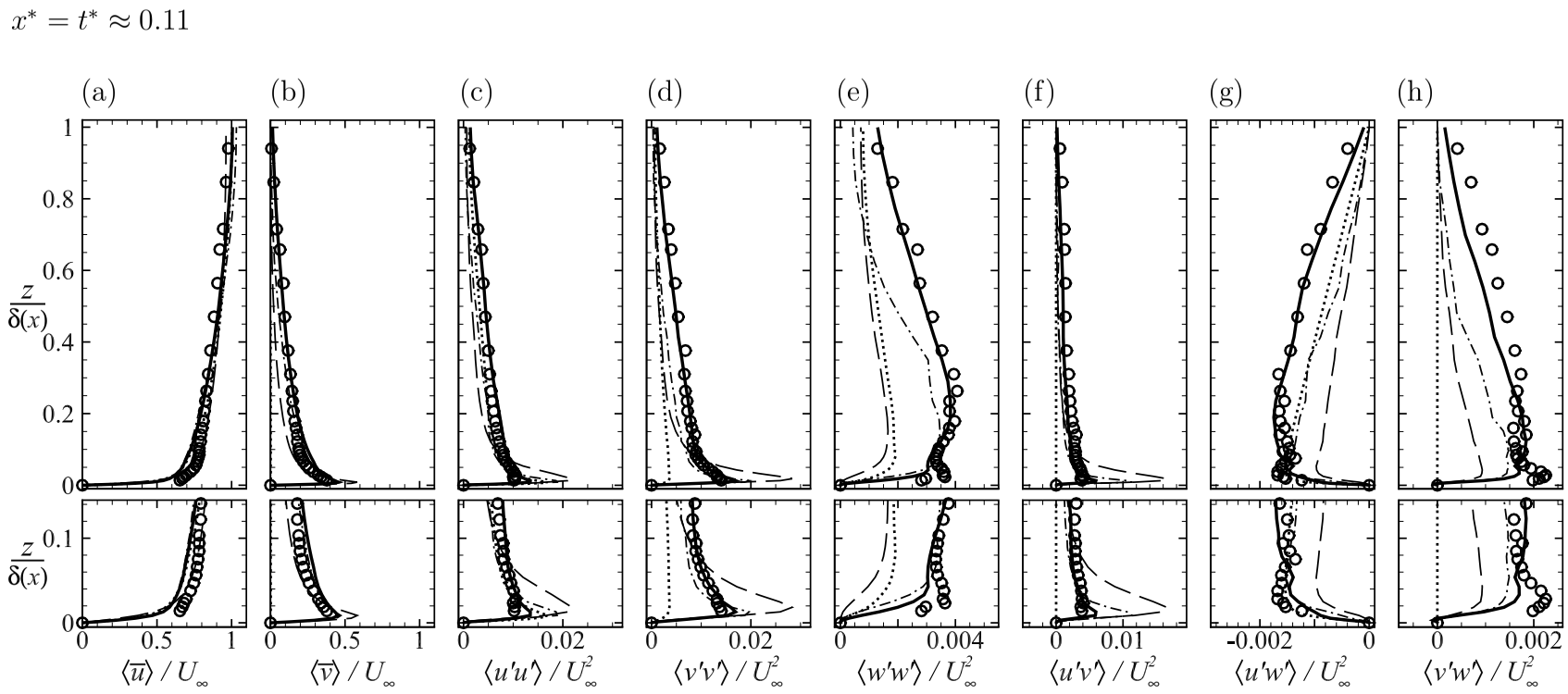

Figure 5.6: Profiles of mean velocities and turbulent stresses in the initial recovery zone predicted by nested-LES and non-nested LES in non-equilibrium, strained turbulent channel flow, compared to experimental measurements in shear-driven, three-dimensional TBL (*Driver and Hebbar*, 1987, 1991), at $x^* = t^* \approx 0.11$. Lines and symbols as in Figure 5.2.

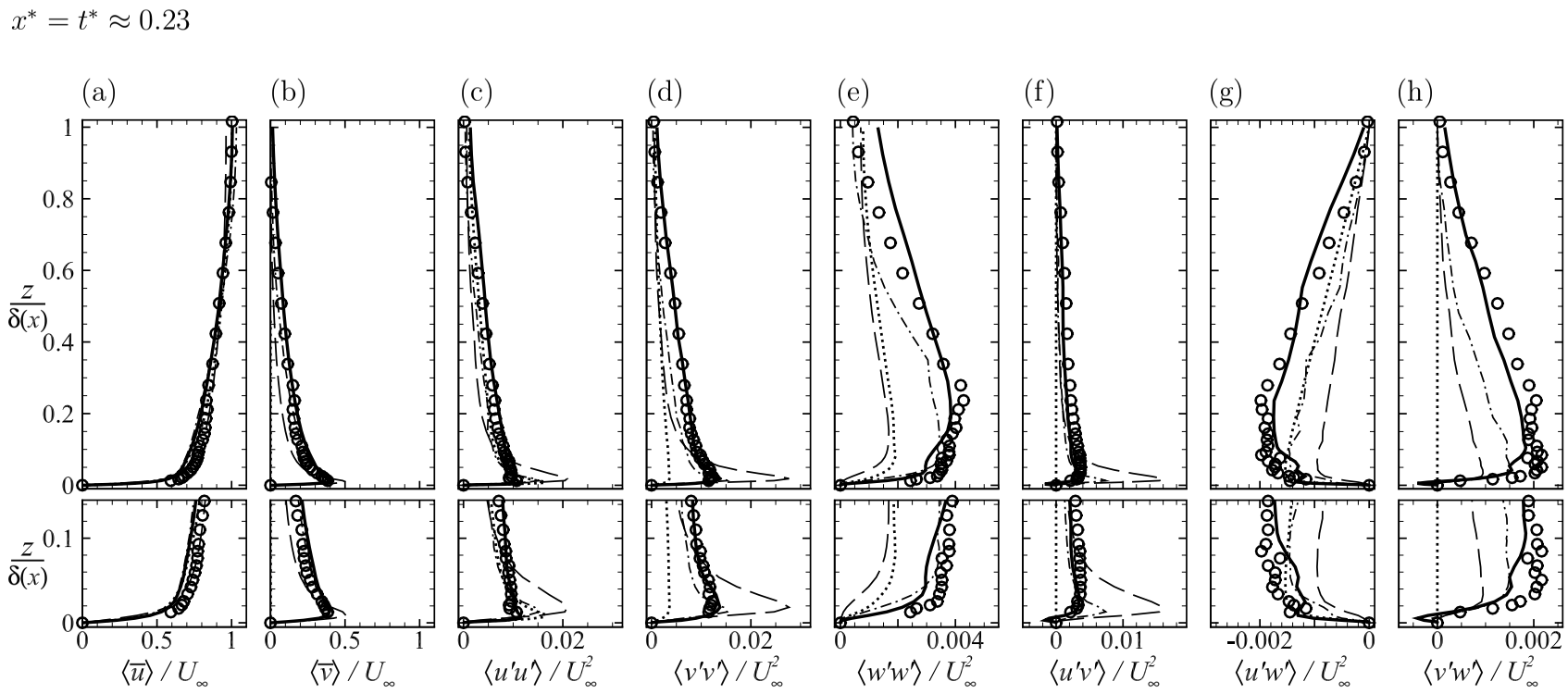

Figure 5.7: Profiles of mean velocities and turbulent stresses in the initial recovery zone predicted by nested-LES and non-nested LES in non-equilibrium, strained turbulent channel flow, compared to experimental measurements in shear-driven, three-dimensional TBL (*Driver and Hebbar*, 1987, 1991), at $x^* = t^* \approx 0.23$. Lines and symbols as in Figure 5.2.

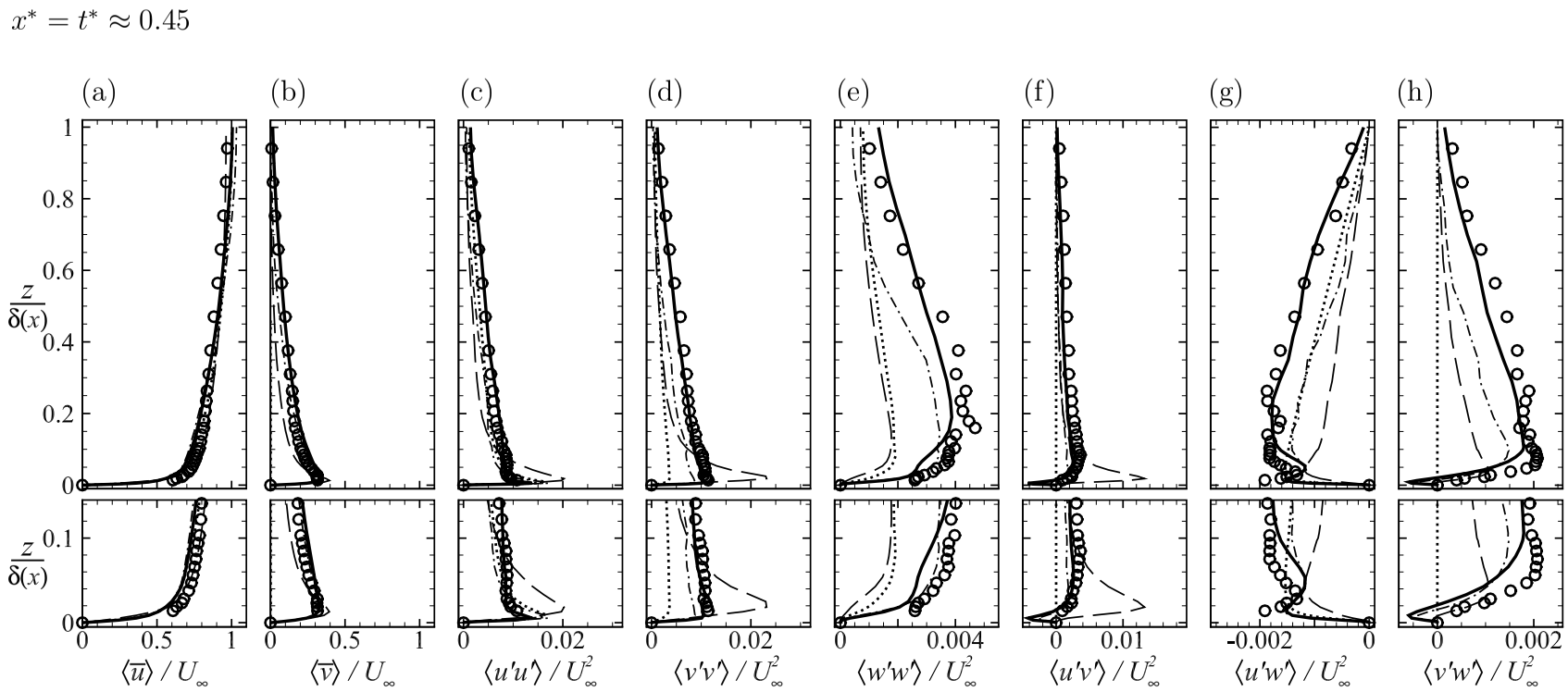

Figure 5.8: Profiles of mean velocities and turbulent stresses in the initial recovery zone predicted by nested-LES and non-nested LES in non-equilibrium, strained turbulent channel flow, compared to experimental measurements in shear-driven, three-dimensional TBL (*Driver and Hebbar*, 1987, 1991), at $x^* = t^* \approx 0.45$. Lines and symbols as in Figure 5.2.

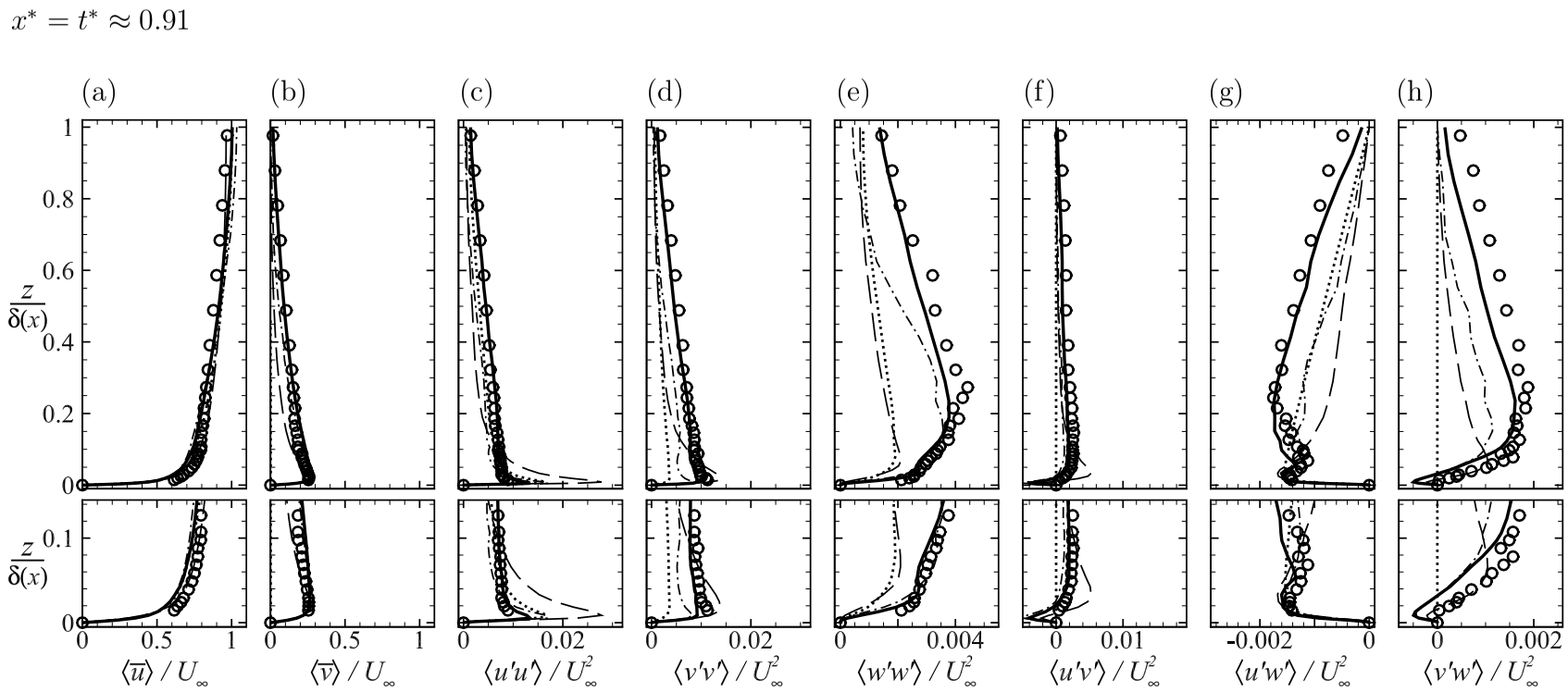

Figure 5.9: Profiles of mean velocities and turbulent stresses in the mid-recovery zone predicted by nested-LES and non-nested LES in non-equilibrium, strained turbulent channel flow, compared to experimental measurements in shear-driven, three-dimensional TBL (*Driver and Hebbar*, 1987, 1991), at $x^* = t^* \approx 0.91$. Lines and symbols as in Figure 5.2.

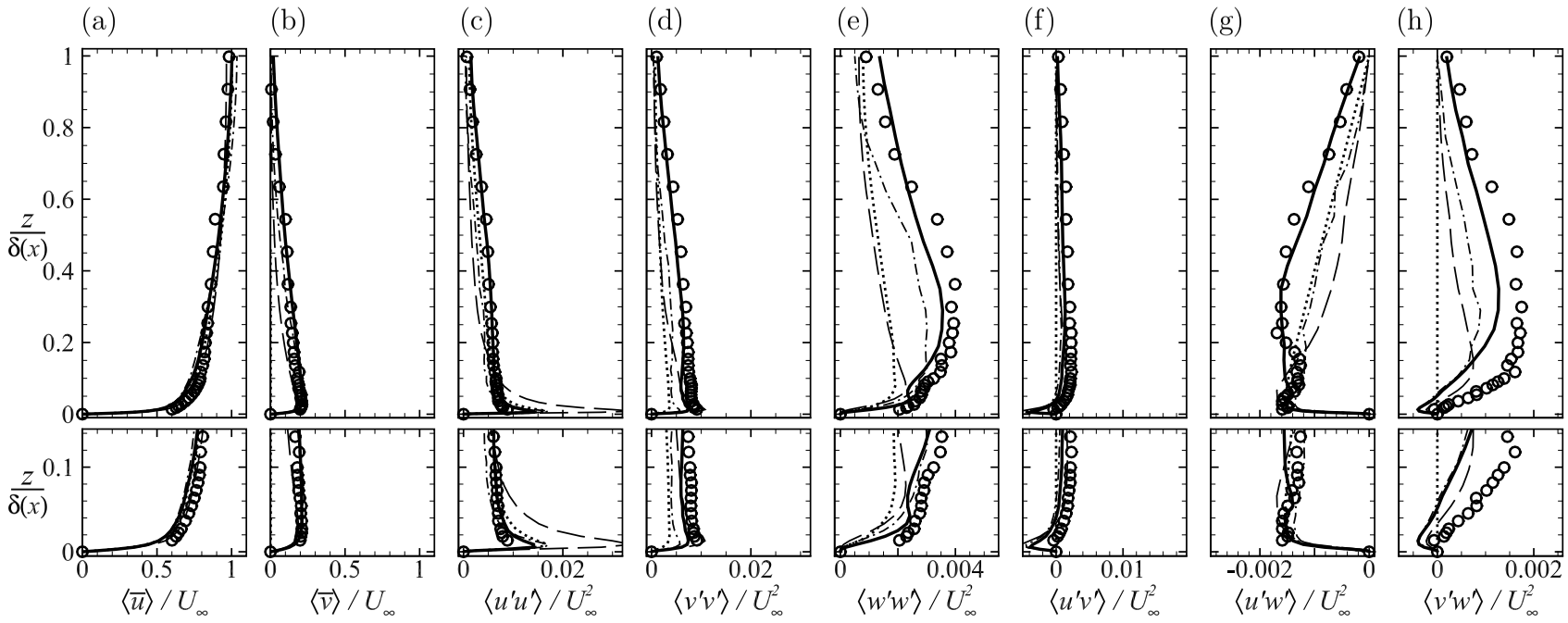

Figure 5.10: Profiles of mean velocities and turbulent stresses in the mid-recovery zone predicted by nested-LES and non-nested LES in non-equilibrium, strained turbulent channel flow, compared to experimental measurements in shear-driven, three-dimensional TBL (*Driver and Hebbar*, 1987, 1991), at $x^* = t^* \approx 1.81$. Lines and symbols as in Figure 5.2.

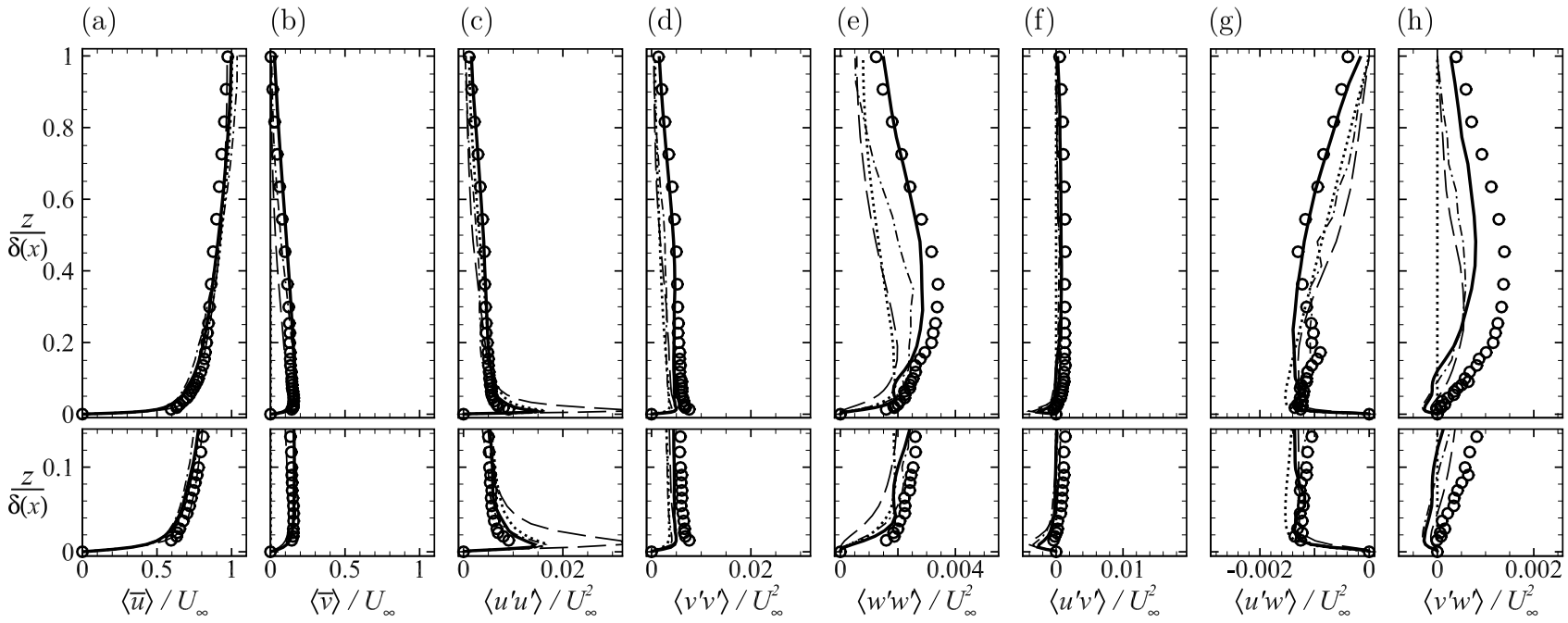

Figure 5.11: Profiles of mean velocities and turbulent stresses in the mid-recovery zone predicted by nested-LES and non-nested LES in non-equilibrium, strained turbulent channel flow, compared to experimental measurements in shear-driven, three-dimensional TBL (*Driver and Hebbar*, 1987, 1991), at $x^* = t^* \approx 3.6$. Lines and symbols as in Figure 5.2.

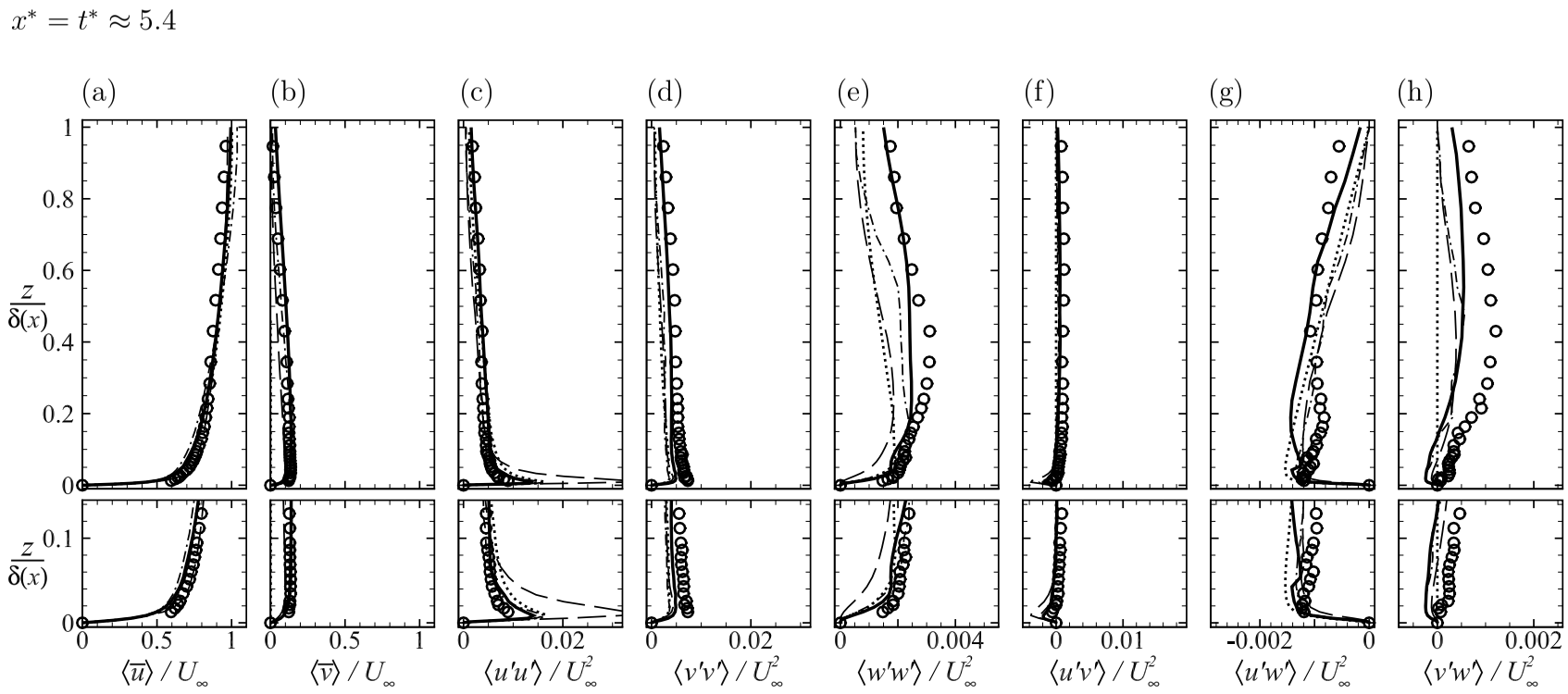

Figure 5.12: Profiles of mean velocities and turbulent stresses in the final recovery zone predicted by nested-LES and non-nested LES in non-equilibrium, strained turbulent channel flow, compared to experimental measurements in shear-driven, three-dimensional TBL (*Driver and Hebbar*, 1987, 1991), at $x^* = t^* \approx 5.4$. Lines and symbols as in Figure 5.2.

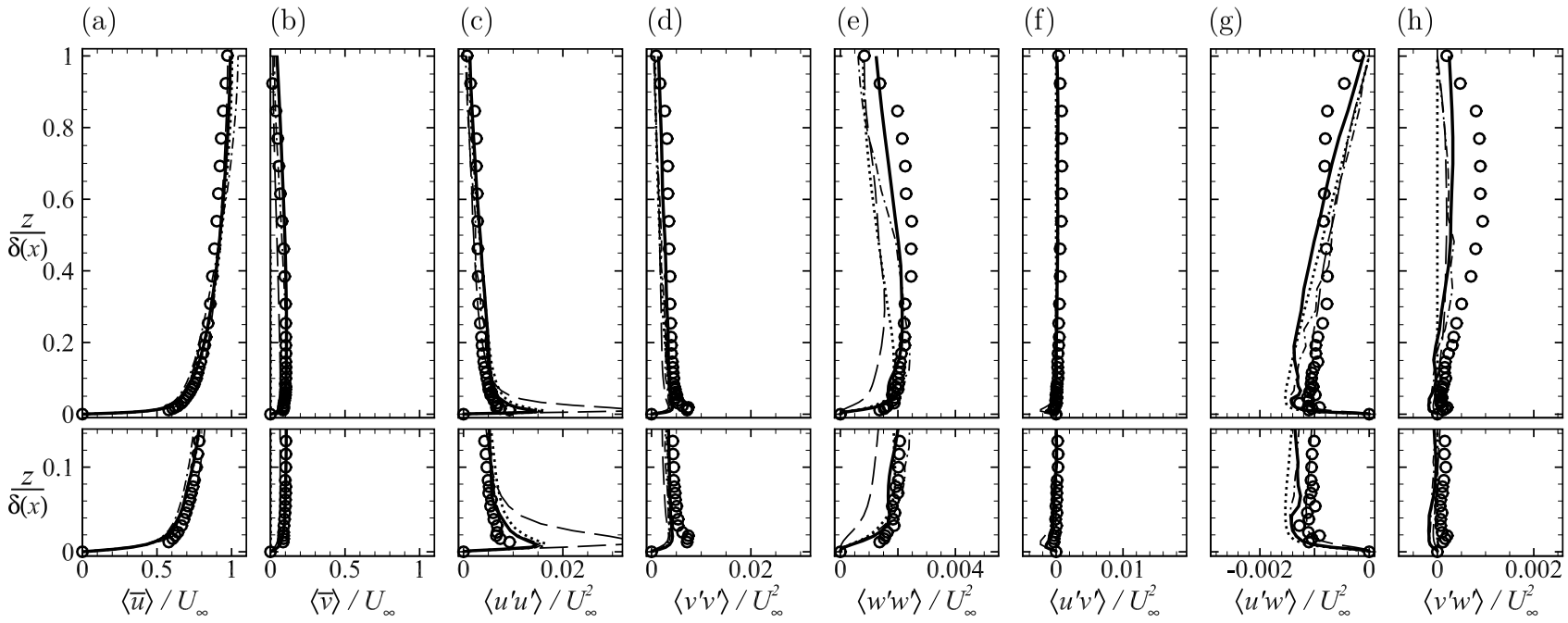

Figure 5.13: Profiles of mean velocities and turbulent stresses in the final recovery zone predicted by nested-LES and non-nested LES in non-equilibrium, strained turbulent channel flow, compared to experimental measurements in shear-driven, three-dimensional TBL (*Driver and Hebbar*, 1987, 1991), at $x^* = t^* \approx 10.9$. Lines and symbols as in Figure 5.2.

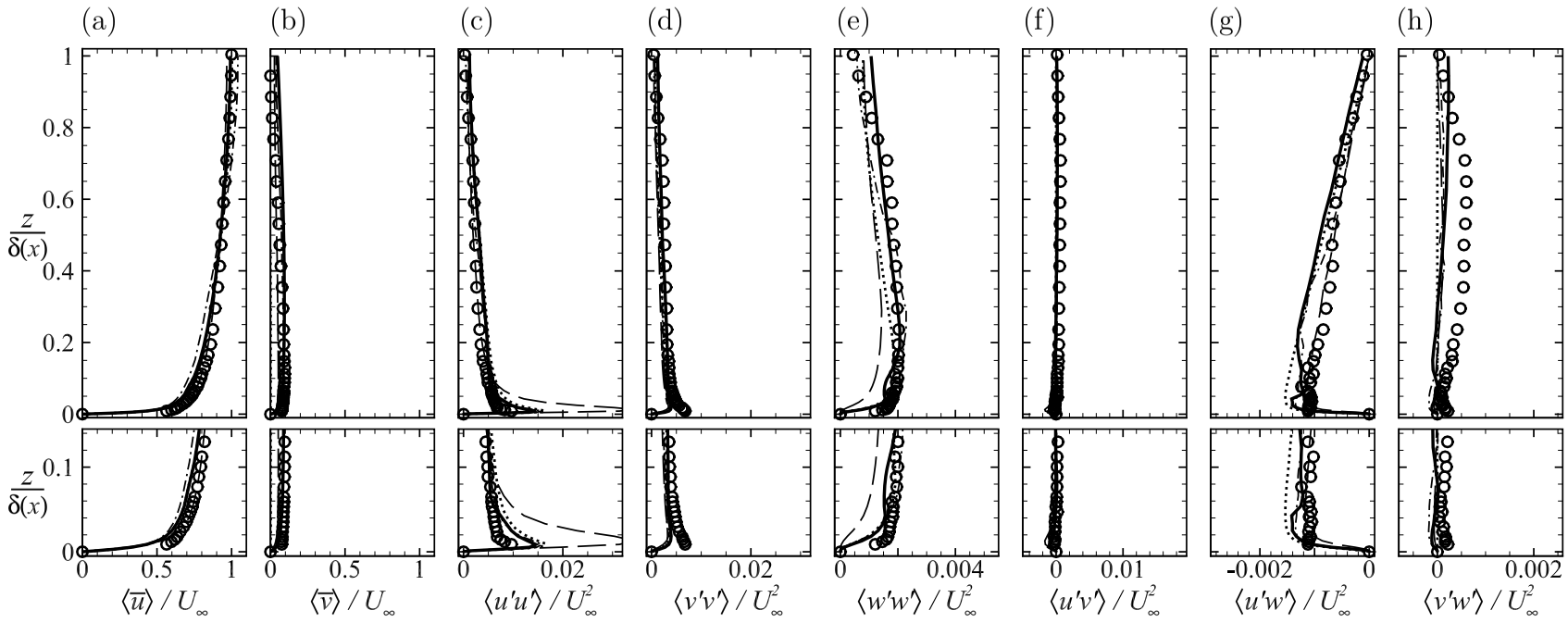

Figure 5.14: Profiles of mean velocities and turbulent stresses in the final recovery zone predicted by nested-LES and non-nested LES in non-equilibrium, strained turbulent channel flow, compared to experimental measurements in shear-driven, three-dimensional TBL (*Driver and Hebbar*, 1987, 1991), at $x^* = t^* \approx 16.3$. Lines and symbols as in Figure 5.2.

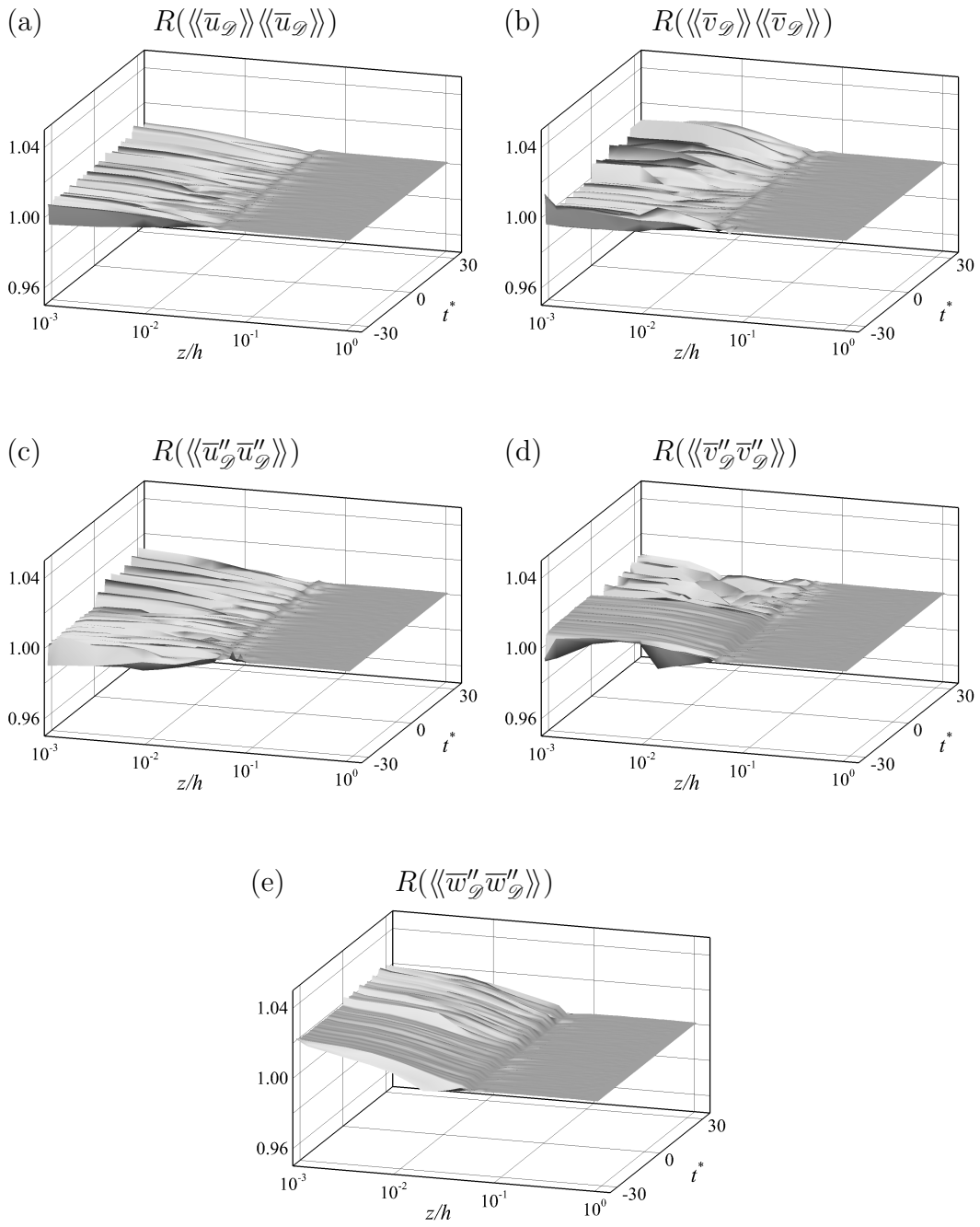

Figure 5.15: Time-history of the renormalization functions, $R(\phi_{\alpha,\mathscr{D}})$, as a function of z/h from nested-LES in non-equilibrium, strained turbulent channel flow for (a) $\langle\langle\overline{u}_{\mathscr{D}}\rangle\rangle\langle\langle\overline{u}_{\mathscr{D}}\rangle\rangle$, (b) $\langle\langle\overline{v}_{\mathscr{D}}\rangle\rangle\langle\langle\overline{v}_{\mathscr{D}}\rangle\rangle$, (c) $\langle\langle\overline{u}''_{\mathscr{D}}\overline{u}''_{\mathscr{D}}\rangle\rangle$, (d) $\langle\langle\overline{v}''_{\mathscr{D}}\overline{v}''_{\mathscr{D}}\rangle\rangle$, and (e) $\langle\langle\overline{w}''_{\mathscr{D}}\overline{w}''_{\mathscr{D}}\rangle\rangle$.

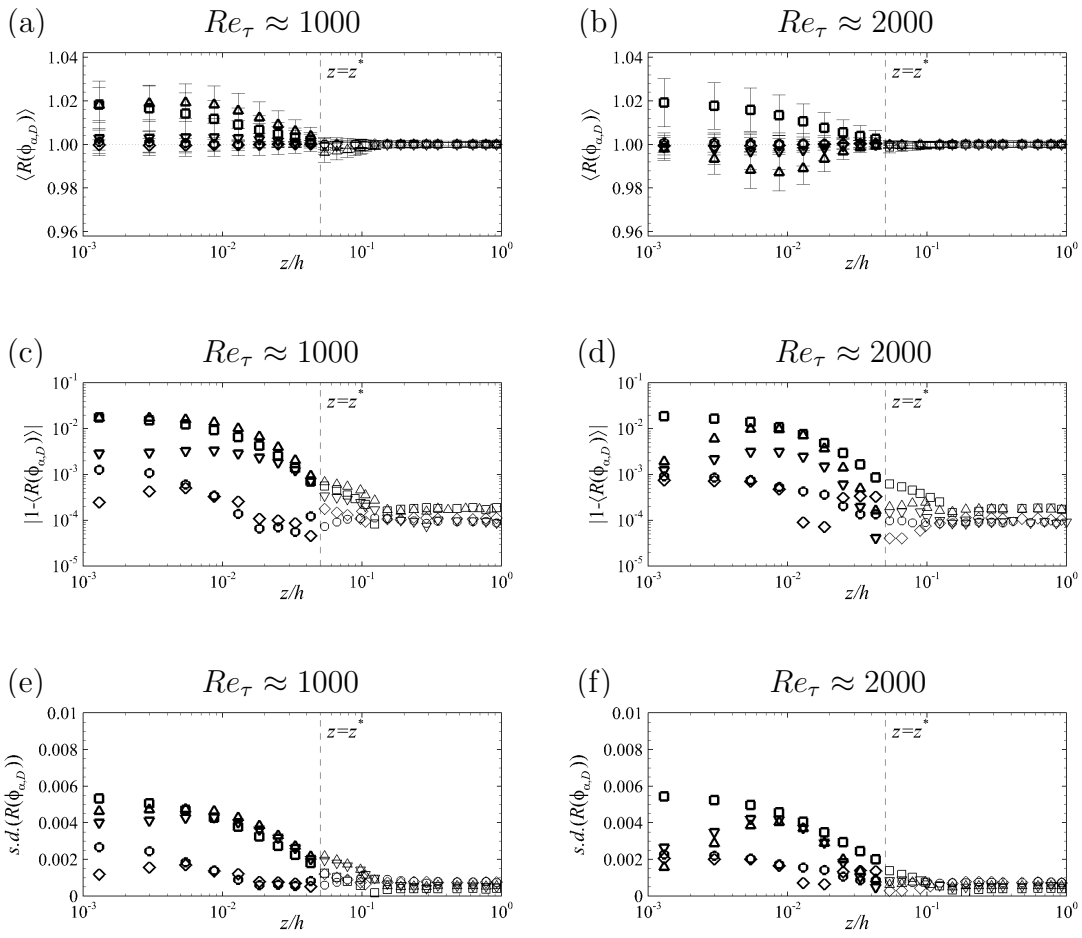

Figure 5.16: (a,b) Time-averaged renormalization functions, $\langle R(\phi_{\alpha,\mathscr{D}})\rangle$, (c,d) deviation of $\langle R(\phi_{\alpha,\mathscr{D}})\rangle$ from unity, and (e,f) standard deviations of $R(\phi_{\alpha,\mathscr{D}})$ in time from nested-LES in non-equilibrium, strained turbulent channel flow in (a,c,e) the straining zone and (b,d,f) the recovery zone: $\triangledown$, $R(\langle\langle\overline{v}_{\mathscr{D}}\rangle\rangle\langle\langle\overline{v}_{\mathscr{D}}\rangle\rangle)$; other symbols as in Figure 4.20.

CHAPTER VI

Summary and Conclusions

- In the present study, a nested-LES approach for computation of high Reynolds number, equilibrium and non-equilibrium, wall-bounded turbulent flows is developed to address the issue of high resolution requirements of conventional LES in the near-wall region, and inability of existing wall models to accurately capture complex physics in the near-wall region.

  This proposed approach couples coarse-resolution LES in the full domain with well-resolved LES in a minimal flow unit to provide high-fidelity simulations of the flow in both the inner and outer layers. The coupling between the minimal flow unit and the full domain of nested-LES is achieved by dynamically renormalizing the velocity fields in each domain at each time-step during the course of the simulation to match the wall-normal profiles of the single-time ensemble-averaged kinetic energies of the components of mean and fluctuating velocities in both domains to those of the minimal flow unit in the inner layer, and to those of the full domain in the outer layer. This 'two-way' coupling corrects the magnitudes and distributions of kinetic energies of all velocity components in both domains, and compensates for the lack of adequate resolution full domain in the inner layer, and the inadequate size of the minimal flow unit in the outer layer.

A unique advantage of the nested-LES approach is its ability to accurately predict the dynamics of turbulence in both the near-wall and outer regions, thus providing a method for computing very high Reynolds number complex flows where the near-wall dynamics plays a critical role.

- The nested-LES approach is applicable to any flows which are 'globally' or 'locally' homogeneous in at least one wall-parallel direction. By a judicious design of grid, nested-LES can reduce the number of required grid points from $O(Re_\tau^2)$ of conventional LES to $O(\log Re_\tau)$ or $O(Re_\tau)$ in flows with two or one locally or globally homogeneous (or nearly homogeneous) directions, respectively.

- To allow meaningful comparison of nested-LES results with DNS and experimental data, a method for reconstructing the true RANS stresses from LES results has been developed.

  The method is based on reconstructing the 1D energy spectra from the filtered 1D spectra computed in LES using an analytical formulation of the 1D energy spectra in wall-bounded flows. The SGS TKE is then recovered by integrating the areas under the reconstructed spectra, and the true RANS stresses are reconstructed using the formulations suggested by *Voelkl et al.* (2000) and *Winckelmans et al.* (2002).

- The performance of the nested-LES approach has been assessed in equilibrium turbulent channel flow at $Re_\tau \approx$1000, 2000, 5000, and 10000, and non-equilibrium, strained turbulent channel flow at $Re_\tau \approx$2000.

  All the simulations were performed, using a patching collocation, spectral-domain decomposition method, in full domains of size $L_x \times L_y \times L_z = 2\pi h \times \pi h \times 2h$ and minimal flow units of size $l_x^+ \approx 3200 - 3900$, and $l_y^+ \approx 1600 - 1950$ wall units, and $l_z = 2h$, and employed resolutions of $64 \times 64 \times 17/33/17$ in both

the full domain and the minimal flow unit, independent of Reynolds number.

In application of nested-LES to equilibrium turbulent channel flows at $1000 \leq Re_\tau \leq 10000$, nested-LES predicts the skin-friction coefficient, first-order turbulence statistics, higher-order moments, two-point correlations, correlation maps, and structural features of the flow in agreement with available DNS and experimental data. In equilibrium turbulent channel flow at $1000 \leq Re_\tau \leq 10000$, nested-LES predicts a skin-friction coefficient within 3% of Deans correlation (*Dean*, 1978). The profiles of the mean velocity and turbulent stresses are in good agreement with available DNS and experimental data. The higher-order moments of the streamwise velocity fluctuations exhibit logarithmic behavior with generalized 'Townsend-Perry' constants in agreement with experimental data in turbulent boundary layers (*Meneveau and Marusic*, 2013). In addition, nested-LES predicts two-point correlations, correlation maps, and structural features of the flow in reasonable with available DNS and experimental data in turbulent channel flow (*Sillero et al.*, 2014; *Wu and Christensen*, 2010).

In application to non-equilibrium, strained turbulent channel flow, nested-LES predicts the evolution of skin-friction coefficients and one-point turbulence statistics in agreement with the experimental data of *Driver and Hebbar* (1987, 1991) in shear-driven, three-dimensional TBL. All the key features in evolution of this shear-driven, non-equilibrium turbulent wall flow are accurately captured by nested-LES.

CHAPTER VII

Future Work

While in the present study, the nested-LES approach has been applied only in channel flows with two globally homogeneous directions, the application of nested-LES to more general and complex flows has been envisioned. This chapter discusses further application of nested-LES and presents recommendations for future work.

One instance of further application of nested-LES is wall-bounded flows at higher Reynolds numbers. Preliminary results have shown that the present implementation of nested-LES in channel flows leads to instability of the simulation at $Re_\tau \geq 20,000$. At the same time, non-nested LES in a minimal flow unit exhibits similar instability at $Re_\tau > 2000$. Therefore, this instability is believed to result from the grid distribution and the patching collocation spectral domain-decomposition method applied in the present study. Identifying the source of instability in the present numerical method, or the application of alternative numerical methods, in order to perform nested-LES in channel flows at higher Reynolds numbers, may be the topic of study in near future. Other high Reynolds number applications, such as super pipe and atmospheric boundary layers, may also be studied using nested-LES and compared to available experimental data.

Application of nested-LES may be further extended to more complex flow conditions, including non-equilibrium flows with only one direction of homogeneity, such as

flow in a decelerating boundary layer, flow over a step or over a two-dimensional hill, flow over a cylinder of any cross-section, and flows with only 'locally' homogeneous directions, such as flow in the mid-section of an airplane wing. Further development and/or adoption of numerical methods capable of handling complex geometries and boundary conditions will be needed for such applications. Investigation of nested-LES in these flows may be the topics of future studies.

Future development of nested-LES may also include alternative ways to couple the solutions in the full-domain and the minimal flow unit. The principle of nested-LES is to allow the LES solutions in the full domain and the minimal flow unit to dynamically 'correct' each other. In the present study, this 'correction' is achieved by coupling the solutions in the two domains through the instantaneous 'mean' and fluctuating velocities. While the results of the present implementation have been satisfactory, it will an interesting topic to explore alternative ways to perform such correction and coupling. Potential alternatives for further investigation include, but are not limited to, coupling based on SGS stresses, and coupling based on eddy sizes and distance from the wall (*Mizuno and Jimenez*, 2013). Searching for a robust and accurate way of coupling the two domains, possibly by taking full advantage of the spectral information available from the LES solutions in the two domains, may be the direction of future development of nested-LES.

APPENDICES

APPENDIX A

Recovery of True RANS Stresses from LES Results

In LES, only the filtered velocity, $\overline{u}_i$, is computed. Consequently, the turbulent stresses, $\langle \overline{u}_i' \overline{u}_j' \rangle$, computed in LES, are not the true RANS stresses, $\langle u_i' u_j' \rangle$. Here, $\overline{u}_i' = \overline{u}_i - \langle \overline{u}_i \rangle$ denotes the fluctuating velocity field in LES, $u_i' = u_i - \langle u_i \rangle$ denotes the RANS fluctuating velocity field, $\overline{u}_i$ is the velocity field resolved in LES, u_i is the full velocity field, and $\langle\ \rangle$ denotes ensemble-averaging in time, and in space, over the homogeneous flow directions. To allow meaningful comparisons between LES results and the RANS turbulence statistics obtained in DNS and experiments, the RANS turbulent stresses were recovered from the turbulent stresses computed in LES, using the formulation suggested by *Voelkl et al.* (2000) and *Winckelmans et al.* (2002), given by

$$\langle u_i' u_j' \rangle \simeq \langle \overline{u}_i' \overline{u}_j' \rangle + \langle \tau_{ij}^* \rangle + \frac{1}{3} \delta_{ij} \langle \tau_{kk} \rangle, \tag{A.1}$$

where $\tau_{ij}^* = \tau_{ij} - \frac{1}{3}\delta_{ij}\tau_{kk}$ denotes the deviatoric part of the SGS stress tensor, and $\langle \tau_{kk} \rangle$ is the SGS turbulent kinetic energy (TKE).

During the course of LES, τ_{kk} can be lumped with the pressure term and solved implicitly, and therefore is not modelled explicitly with most SGS models. With such SGS models, application of equation (A.1) to obtain $\langle u_i' u_j' \rangle$ requires a method

for reconstructing $\langle \tau_{kk} \rangle$. This chapter describes a method for recovering the SGS TKE and hence the true RANS stresses from LES of wall-bounded turbulence. This method is then applied to all the results from nested-LES to obtain the true RANS stresses for comparison with DNS and experimental data.

A.1 Overview

To address the issue of obtaining the true RANS stresses from LES, a number of approaches have been proposed. The most direct approach is to model the full SGS stress, τ_{ij}, instead of τ_{ij}^*, as is done in SGS models such as the stretched vortex model (*Misra and Pullin*, 1997; *Voelkl et al.*, 2000). However, few existing SGS models belong to this category. A second approach is to perform the LES using τ_{ij}^*, but solve additional equations to compute the SGS TKE, $\langle \tau_{kk} \rangle$. These auxiliary equations can be in the form of algebraic expressions developed using dimensional analysis (*Bardina et al.*, 1980; *Yoshizawa*, 1986; *Moin et al.*, 1991; *Wong and Lilly*, 1994), or transport equations which solve for the SGS TKE (*Wong*, 1992; *Ghosal et al.*, 1995; *Kim and Menon*, 1995). The algebraic expressions have the advantage of a simple formulation, but their accuracy is limited by the assumptions in the dimensional arguments, the undetermined model constants, and the approximations needed for different flow types. Approaches based on the solution of additional transport equations for the SGS TKE can be more accurate, but introduce new modelling issues and incur additional computational cost. A third approach is to reconstruct the full energy spectra from the filtered spectra computed in LES using formulations of the energy spectra in the inertial and dissipative ranges, and recover the SGS TKE by integrating the areas under the reconstructed spectra. This approach is low in cost and can be applied at a post-processing stage to any SGS model, but so far has only been applied to homogeneous, isotropic turbulence (*Knaepen et al.*, 2002; *Meyers and Baelmans*, 2004;

Salesky and Chamecki, 2012). In the present study, the latter approach is extended to wall-bounded turbulence.

The SGS TKE is recovered based on reconstructing the full one-dimensional (1D) energy spectra from the filtered 1D spectra computed in LES at each wall-normal location using an analytical formulation of the 1D energy spectra in wall flows. These analytical 1D spectra are used to 'continue' the 1D energy spectra from the smallest scales resolved in LES down to the Kolmogorov scale. The SGS TKE is then recovered by integrating the areas under the reconstructed spectra, and the true RANS stresses are reconstructed using equation (A.1).

In the following sections, an analytical formulation for the 1D energy spectra in wall-bounded turbulence is first developed in Section A.2. The effect of LES filtering on the spectra is then analyzed in Section A.3. The accuracy of the proposed method for recovering the SGS TKE and true RANS stresses is then assessed in Section A.4 using a filtered DNS database and two LES databases of turbulent channel flow.

A.2 The 1D Energy Spectra in Wall-Bounded Turbulence

A.2.1 Universal Representation of the 1D Energy Spectra in Wall-Bounded Turbulence

The most readily available energy spectra in wall-bounded turbulence are the 1D spectra. In the homogeneous flow directions, the 1D spectra can be computed by spectral analysis in space, and averaging in time. In the inhomogeneous flow directions, the 1D spectra are generally obtained by temporal analysis at a given position, and conversion to spatial spectra by invoking the Taylor's hypothesis, assuming the convective velocity is only a function of the position, and not of the size of the scales (*Schlatter et al.*, 2010). Figure A.1 shows the normalized streamwise and spanwise 1D spectra of the total TKE in the outer layer ($z/h = 0.5$) and near-wall region

($z^+ \approx 15$) from DNS databases of turbulent channel flow at $Re_\tau \approx 180$, 550, 950, and 2000 (*del Alamo and Jimenez*, 2003; *del Alamo et al.*, 2004; *Hoyas and Jimenez*, 2006). The 1D energy spectra are normalized as

$$\tilde{E}^{1\mathrm{D}}(\tilde{k}_\alpha) \equiv E^{1\mathrm{D}}(k_\alpha)/(k_d \nu^2) = E^{1\mathrm{D}}(k_\alpha)/((\langle\epsilon\rangle \nu^5)^{\frac{1}{4}}, \tag{A.2}$$

and plotted as a function of the normalized wavenumber

$$\tilde{k}_\alpha \equiv k_\alpha / k_d, \tag{A.3}$$

where $k_d \equiv (\langle\epsilon\rangle/\nu^3)^{\frac{1}{4}}$ is the local Kolmogorov wavenumber, $\epsilon(\boldsymbol{x}, t)$ is the rate of TKE dissipation at location $\boldsymbol{x}$ at time t, and $\langle\ \rangle$ denotes an ensemble-average over the homogeneous flow directions and in time. In the outer layer of the channel, where the turbulence structure is nearly isotropic, the normalized streamwise and spanwise spectra nearly collapse in the inertial and dissipative ranges, as shown in Figure A.1(a). In the inner layer, where the turbulence structure is highly anisotropic, however, the streamwise and spanwise spectra follow separate trends and no longer collapse in the inertial and dissipative ranges, as shown in Figure A.1(b).

The nature of the disparity between the spectra in the different flow directions in Figure A.1(b) suggests the possibility for presence of different Kolmogorov wavenumbers, k_d, in these directions in the inner layer. The different Kolmogorov wavenumbers would reflect the different rates of dissipation of TKE in the different flow directions. Indeed, the total dissipation rate,

$$\epsilon(\boldsymbol{x}, t) = \nu \frac{\partial u_i'}{\partial x_j} \left(\frac{\partial u_i'}{\partial x_j} + \frac{\partial u_j'}{\partial x_i} \right) = \nu \left[\frac{\partial u_i'}{\partial x_j} \frac{\partial u_i'}{\partial x_j} + \frac{\partial}{\partial x_j} \left(u_i' \frac{\partial u_j'}{\partial x_i} \right) \right], \tag{A.4}$$

can be expressed as the sum of contributions from the streamwise, spanwise, and

wall-normal gradients, as

$$\epsilon(\boldsymbol{x},t) = \sum_{\alpha=1}^{3} \epsilon_\alpha(\boldsymbol{x},t), \tag{A.5}$$

where

$$\epsilon_\alpha(\boldsymbol{x},t) = \nu \left[\frac{\partial u_i'}{\partial x_\alpha}\frac{\partial u_i'}{\partial x_\alpha} + \frac{\partial}{\partial x_\alpha}\left(u_i' \frac{\partial u_\alpha'}{\partial x_i} \right) \right], \tag{A.6}$$

and no summation is implied over the index α in equation (A.6). If the turbulence were homogeneous and isotropic, $\langle \epsilon_\alpha \rangle$ would be the same in all directions and $\langle \epsilon \rangle = \langle 3\epsilon_\alpha \rangle$, while $\langle\ \rangle$ would be invariant with the position.

Figure A.2 shows the profiles of $\langle 3\epsilon_\alpha \rangle^+ \equiv 3\langle \epsilon_\alpha \rangle/(u_\tau^4/\nu)$ and $\langle \epsilon \rangle^+ \equiv \langle \epsilon \rangle/(u_\tau^4/\nu)$ as a function of z^+ from the aforementioned DNS databases at $Re_\tau \approx 180$, 550, and 950 (*del Alamo and Jimenez*, 2003; *del Alamo et al.*, 2004). In the outer layer, where the turbulence is nearly isotropic, the profiles of $\langle 3\epsilon_\alpha \rangle^+$ are nearly identical for $\alpha = x, y, z$ and match the profile of $\langle \epsilon \rangle^+$. In the inner layer, where the turbulence is anisotropic, however, the profiles of $\langle 3\epsilon_\alpha \rangle^+$ have different trends for different α and none of them matches the profile of $\langle \epsilon \rangle^+$.

The disparate magnitudes of $\langle 3\epsilon_\alpha \rangle$ in the inner layer suggest that a better collapse of the 1D spectra in wall-bounded turbulence may be obtained if the 1D energy spectra are normalized as

$$\hat{E}^{1\mathrm{D}}(\hat{k}_\alpha) \equiv E^{1\mathrm{D}}(k_\alpha)/(k_{d,\alpha}\nu^2), \tag{A.7}$$

and plotted as a function of

$$\hat{k}_\alpha \equiv k_\alpha/k_{d,\alpha}, \tag{A.8}$$

where $k_{d,\alpha} \equiv (\langle 3\epsilon_\alpha \rangle/\nu^3)^{\frac{1}{4}}$. Figure A.3 shows that this normalization indeed results in a collapse of the streamwise and spanwise spectra in the inertial and dissipative ranges of channel flow, in both the inner and outer layers.

A.2.2 An Analytical Formulation for the 1D Energy Spectra in Wall-Bounded Turbulence

The collapse of the 1D energy spectra in different directions in the inertial and dissipative ranges of wall-bounded turbulence, even in the near-wall region, observed in Figure A.3, suggests that the spectral energy in the inertial and dissipative ranges of wall-bounded turbulence can be mapped into an isotropic space by normalizing the spectra using $k_{d,\alpha}$ and ν, as in equation (A.7).

In homogeneous, isotropic turbulence, the 1D energy spectrum is related to the three-dimensional (3D) spectrum through the relation (*Hinze*, 1975; *Pope*, 2000)

$$\tilde{E}^{1\mathrm{D}}(\tilde{k}_\alpha) = 2\int_{\tilde{k}_\alpha}^{\infty} \frac{\tilde{E}^{3\mathrm{D}}(\tilde{k})}{\tilde{k}} d\tilde{k}, \tag{A.9}$$

where $\tilde{E}^{1\mathrm{D}}(\tilde{k}_\alpha)$ and $\tilde{k}_\alpha$ are defined in equations (A.2) and (A.3), respectively, and $\tilde{E}^{3\mathrm{D}}(\tilde{k}_\alpha)$ is any of the classical formulations (*Hinze*, 1975; *Pope*, 2000) of the 3D energy spectrum in homogeneous, isotropic turbulence, which can be broadly represented as

$$\tilde{E}^{3\mathrm{D}}(\tilde{k}) = C_K \tilde{k}^{-5/3} F(\tilde{k}), \tag{A.10}$$

where C_K is the Kolmogorov constant, and $F(\hat{k})$ is the dissipation-range correction to the Kolmogorov spectrum.

This suggests that, similar to equation (A.9), it may be possible to represent the normalized 1D energy spectra, $\hat{E}^{1\mathrm{D}}(\hat{k}_\alpha)$, in the inertial and dissipative ranges of wall-bounded turbulence as

$$\hat{E}^{1\mathrm{D}}(\hat{k}_\alpha) = 2\int_{\hat{k}_\alpha}^{\infty} \frac{\hat{E}^{3\mathrm{D}}(\hat{k})}{\hat{k}} d\hat{k}, \tag{A.11}$$

where

$$\hat{E}^{3D}(\hat{k}) = C_K \hat{k}^{-5/3} F(\hat{k}). \tag{A.12}$$

In the present study, two formulations for $\hat{E}^{3D}(\hat{k})$ have been considered, one corresponding to the classical formulation of *Pao* (1965), and the other to the formulation of *Meyers and Meneveau* (2008), which was derived from a formulation suggested by *Kraichnan* (1959). In the formulation of *Pao* (1965), $\hat{E}^{3D}(\hat{k})$ is expressed as

$$\hat{E}^{3D}(\hat{k}) = C_K \hat{k}^{-5/3} \exp\left(-\frac{3}{2}\alpha_1 \hat{k}^{4/3}\right), \tag{A.13}$$

where α_1 is a model parameter. In the formulation of *Meyers and Meneveau* (2008), $\hat{E}^{3D}(\hat{k})$ is expressed as

$$\hat{E}^{3D}(\hat{k}) = C_K \hat{k}^{-5/3} \exp(-\alpha_1 \hat{k}) B(\hat{k}), \tag{A.14}$$

where α_1 is a model parameter, and

$$B(\hat{k}) = \left[1 + \frac{\alpha_2 (\hat{k}/\alpha_4)^{\alpha_3}}{1 + (\hat{k}/\alpha_4)^{\alpha_3}}\right], \tag{A.15}$$

with $\alpha_2 \approx 2.4$, $\alpha_3 \approx 2.4$ and $\alpha_4 \approx 0.12$ (*Meyers and Meneveau*, 2008).

The two unknown parameters, C_K and α_1, in both formulations are found in the present study by applying the constraints

$$\int_{\hat{k}_{\min}}^{\hat{k}_{\max}} \hat{E}^{1D}_{\text{model}}(\hat{k}_\alpha, C_K, \alpha_1) d\hat{k}_\alpha = \int_{\hat{k}_{\min}}^{\hat{k}_{\max}} \hat{E}^{1D}_{\text{simulation}}(\hat{k}_\alpha) d\hat{k}_\alpha, \tag{A.16a}$$

$$\int_{\hat{k}_{\min}}^{\hat{k}_{\max}} \left[\frac{\hat{E}^{1D}_{\text{model}}(\hat{k}_\alpha, C_K, \alpha_1) - \hat{E}^{1D}_{\text{simulation}}(\hat{k}_\alpha)}{\hat{E}^{1D}_{\text{simulation}}(\hat{k}_\alpha)}\right]^2 d\hat{k}_\alpha = \text{minimal}, \tag{A.16b}$$

where $\hat{k}_{\min}$ is a wavenumber in the inertial range, and $\hat{k}_{\max}$ is the highest wavenumber resolved in the simulations. Equation (A.16a) requires that the total TKE be the same in the modelled and computed 1D spectra over the range of $\hat{k}_{\min} < \hat{k} < \hat{k}_{\max}$, while equation (A.16b) requires that the L^2-norm of the relative error between the modelled and computed spectra be minimized over the range of $\hat{k}_{\min} < \hat{k} < \hat{k}_{\max}$.

Figure A.3 shows the comparison between the $\hat{E}^{1D}(\hat{k})$ obtained from DNS (*del Alamo and Jimenez*, 2003; *del Alamo et al.*, 2004; *Hoyas and Jimenez*, 2006) and the $\hat{E}^{1D}(\hat{k})$ computed using equation (A.11) with $\hat{E}^{3D}(\hat{k})$ given by equation (A.13) or equation (A.14), and C_K and α_1 determined using equations (A.16a) and (A.16b), respectively, with $\hat{k}_{\min}$ set to $\hat{k}_{\min} = 0.07$. The modelled 1D spectra closely match the DNS spectra in the inertial and dissipative ranges, verifying the applicability of equations (A.11-A.16) to wall-bounded turbulence.

The values of C_K and α_1 resulting from application of equations (A.11–A.16) to these DNS data (*del Alamo and Jimenez*, 2003; *del Alamo et al.*, 2004; *Hoyas and Jimenez*, 2006) are shown in Figure A.4 and tabulated in Tables A.1–A.2 for each of the formulations of *Pao* (1965) and *Meyers and Meneveau* (2008). In the outer region ($z^+ > 100$) the profiles of C_K and α_1 obtained from DNS databases at different Reynolds numbers collapse when plotted as a function of the outer variable z/h, as shown in Figures A.4(b,d). In this region, the values of C_K and α_1 are nearly constant for both formulations, and vary between $2.6 \lesssim C_K \lesssim 2.8$ and $2.5 \lesssim \alpha_1 \lesssim 2.6$ for Pao's spectrum (*Pao*, 1965), and between $1.5 \lesssim C_K \lesssim 1.6$ and $4.3 \lesssim \alpha_1 \lesssim 4.6$ for Meyers & Meneveau's spectrum (*Meyers and Meneveau*, 2008). The former are higher than the values of $C_K = \alpha_1 \simeq 1.7$ suggested by *Pao* (1965) for high Reynolds number, isotropic turbulence, while the latter are comparable with the generally accepted values of $C_K \approx 1.5$ for the Kolmogorov constant and the range of $\alpha_1 \approx 4.18 - 4.97$ suggested by *Meyers and Meneveau* (2008). In the near-wall region ($z^+ \leq 100$), the profiles

of C_K and α_1 obtained from DNS databases at different Reynolds numbers collapse when plotted as a function of the inner variable z^+, as shown in Figures A.4(a,c). Near-wall peaks of C_K and α_1 are observed at $z^+ \approx 10$ for both the formulations of *Pao* (1965) and *Meyers and Meneveau* (2008).

A.3 The Filtered 1D Energy Spectra in Wall-Bounded Turbulence

The 1D energy spectra obtained in LES are affected by the filtering operations employed in LES. As such, they cannot be directly represented by equation (A.11). In this section, the extension of equation (A.11) to filtered 1D spectra, as would be obtained from LES, is discussed. The discussion will focus on spectral cut-off filters, which will be applied in all the simulations performed in the present study. For any graded filters of known shape, the LES velocity field can be reconstructed up to a spectral cut-off filter by deconvolution (*Stolz and Adams*, 1999; *Stolz et al.*, 2001), and the methods described below can then be applied to reconstruct the SGS TKE of the deconvolved velocity field.

A.3.1 An Analytical Formulation for the Filtered 1D Energy Spectra in Wall-Bounded Turbulence

We begin by considering a geometric interpretation of equation (A.9) or (A.11). For an unfiltered velocity field, the quantity $\hat{E}^{1\mathrm{D}}(\hat{k}_\alpha)d\hat{k}_\alpha$ represents the normalized TKE arising from all wavenumbers which have an α-component between $\hat{k}_\alpha$ and $(\hat{k}_\alpha + d\hat{k}_\alpha)$ or between $-\hat{k}_\alpha$ and $-(\hat{k}_\alpha + d\hat{k}_\alpha)$. In isotropic turbulence, or in any normalization for which the turbulence is isotropic, such as that given by equations (A.7–A.8) in wall-bounded turbulence, $\hat{E}^{1\mathrm{D}}(\hat{k}_\alpha)d\hat{k}_\alpha$ can be geometrically represented as the volume occupied by the shaded disks shown in Figure A.5. This geometric

representation gives a relation between $\hat{E}^{1D}(\hat{k}_\alpha)$ and $\hat{E}^{3D}(\hat{k})$ given by

$$\hat{E}^{1D}(\hat{k}_\alpha)d\hat{k}_\alpha = \left[2\int_{\hat{k}_\alpha}^{\infty} 2\ \frac{\hat{E}^{3D}(\hat{k})}{4\pi\hat{k}^2}\ 2\pi\hat{k}\sin\theta\ \frac{d\hat{k}}{\sin\theta}\right] d\hat{k}_\alpha = \left[2\int_{\hat{k}_\alpha}^{\infty} \frac{\hat{E}^{3D}(\hat{k})}{\hat{k}}\ d\hat{k}\right] d\hat{k}_\alpha, \tag{A.17}$$

where $\hat{E}^{3D}(\hat{k})/(4\pi\hat{k}^2)$ is the spectral energy density on the sphere of radius $\hat{k}$, the quantity $2\pi\hat{k}\sin\theta$ represents the circumference of the shaded disk at its cross-section with the sphere of radius $\hat{k}$, $d\hat{k}/\sin\theta$ is the projection of $d\hat{k}$ in the direction of the radius of the shaded disk, and the angle θ is given by $\theta = \cos^{-1}(\hat{k}_\alpha/\hat{k})$. The first factor of 2 in equation (A.17) accounts for the fact that $\hat{E}^{1D}(\hat{k}_\alpha)$ represents the spectral energy arising from both $\pm\hat{k}_\alpha$, while the second factor of 2 accounts for the fact that, by convention, $(k_{d,\alpha}\nu)^2\int_0^\infty \hat{E}^{1D}(\hat{k}_\alpha)d\hat{k}_\alpha = \langle u_i' u_i'\rangle$, while $(k_{d,\alpha}\nu)^2\int_0^\infty \hat{E}^{3D}(\hat{k})d\hat{k} = \frac{1}{2}\langle u_i' u_i'\rangle$.

When the velocity field is filtered in the $\hat{k}_\beta$- or $\hat{k}_\gamma$-directions at cutoff wavenumber $\hat{k}_{c\beta}$ or $\hat{k}_{c\gamma}$, respectively, part of the spectral energy on the disk is removed, corresponding to the cross-section of the disk and the shaded dome in Figure A.6. In this case, the normalized TKE arising from the filtered disk is given by

$$\hat{E}_F^{1D}(\hat{k}_\alpha \mid \hat{k}_{c\beta}, \hat{k}_{c\gamma})\ d\hat{k}_\alpha = \left[2\int_{\hat{k}_\alpha}^{\infty} 2\ \frac{\hat{E}^{3D}(\hat{k})}{4\pi\hat{k}^2}\ (2\pi - 4\varphi_\beta - 4\varphi_\gamma)\ \hat{k}\sin\theta\ \frac{d\hat{k}}{\sin\theta}\right] d\hat{k}_\alpha, \tag{A.18}$$

where $2\varphi_\beta$ and $2\varphi_\gamma$ are the included angles corresponding to the cross-section of the disk and the shaded dome, as shown in Figure A.6, and are given by

$$\varphi_\sigma(\hat{k}, \hat{k}_\alpha, \hat{k}_{c\sigma}) = \tan^{-1}[\sqrt{\hat{k}^2 - (\hat{k}_\alpha^2 + \hat{k}_{c\sigma}^2)}/\hat{k}_{c\sigma}] \quad , \text{ if } \hat{k}^2 > \hat{k}_\alpha^2 + \hat{k}_{c\sigma}^2, \tag{A.19a}$$

$$= 0 \quad , \text{ if } \hat{k}^2 < \hat{k}_\alpha^2 + \hat{k}_{c\sigma}^2, \tag{A.19b}$$

for $\sigma = \beta$ or γ and it is required that the quantity $2\pi - 4\varphi_\beta(\hat{k}, \hat{k}_\alpha, \hat{k}_{c\beta}) - 4\varphi_\gamma(\hat{k}, \hat{k}_\alpha, \hat{k}_{c\gamma}) \geq$

0 for all $\hat{k}$, $\hat{k}_\alpha$, $\hat{k}_{c\beta}$, and $\hat{k}_{c\gamma}$ to ensure that the filtered energy spectrum remains positive. Equation (A.18) can be rewritten as

$$\hat{E}_{\mathrm{F}}^{1\mathrm{D}}(\hat{k}_\alpha \mid \hat{k}_{c\beta}, \hat{k}_{c\gamma}) = 2 \int_{\hat{k}_\alpha}^{\infty} [1 - F(\hat{k}, \hat{k}_\alpha, \hat{k}_{c\beta}) - F(\hat{k}, \hat{k}_\alpha, \hat{k}_{c\gamma})] \frac{\hat{E}^{3\mathrm{D}}(\hat{k})}{\hat{k}} \, d\hat{k}, \qquad \text{(A.20)}$$

where

$$F(\hat{k}, \hat{k}_\alpha, \hat{k}_{c\sigma}) = 2\varphi_\sigma(\hat{k}, \hat{k}_\alpha, \hat{k}_{c\sigma})/\pi \quad \text{for} \quad \sigma = \beta \text{ or } \gamma, \qquad \text{(A.21)}$$

and, similar to equation (A.18), it is required that $1 - F(\hat{k}, \hat{k}_\alpha, \hat{k}_{c\beta}) - F(\hat{k}, \hat{k}_\alpha, \hat{k}_{c\gamma}) \geq 0$ for all $\hat{k}$, $\hat{k}_\alpha$, $\hat{k}_{c\beta}$, and $\hat{k}_{c\gamma}$.

Equations (A.20–A.21) provide an analytical formulation of the filtered 1D energy spectra in wall-bounded turbulence. The SGS TKE can then be obtained by continuation of the LES spectra using equations (A.20–A.21) and numerical integration of the area under the continued spectra in the subgrid-scales. For a velocity field filtered in all three spatial directions, the spectral space can be partitioned into eight regions, as shown in Figure A.7(a). Region A represents the wavenumbers resolved in LES. Region B_α corresponds to wavenumbers $\hat{k}_\alpha > \hat{k}_{c\alpha}$, $\hat{k}_\beta \leq \hat{k}_{c\beta}$, and $\hat{k}_\gamma \leq \hat{k}_{c\gamma}$. Region $\mathrm{C}_{\alpha\beta}$ corresponds to wavenumbers $\hat{k}_\alpha > \hat{k}_{c\alpha}$, $\hat{k}_\beta > \hat{k}_{c\beta}$, and $\hat{k}_\gamma \leq \hat{k}_{c\gamma}$. Region $\mathrm{D}_{\alpha\beta\gamma}$ corresponds to wavenumbers $\hat{k}_\alpha > \hat{k}_{c\alpha}$, $\hat{k}_\beta > \hat{k}_{c\beta}$, and $\hat{k}_\gamma > \hat{k}_{c\gamma}$. The contribution of each spectral region to the 1D energy spectrum is shown schematically in Figure A.7(b). Thus, the SGS TKE can be evaluated by summing the TKE in each spectral region as

$$\begin{aligned} \langle \tau_{kk} \rangle \; = \langle u_i' u_i' \rangle_{\mathrm{SGS}} \;\; &= \;\; \langle u_i' u_i' \rangle_{\mathrm{B}_\alpha} \; + \langle u_i' u_i' \rangle_{\mathrm{B}_\beta} \; + \langle u_i' u_i' \rangle_{\mathrm{B}_\gamma} \\ &+ \;\; \langle u_i' u_i' \rangle_{\mathrm{C}_{\alpha\beta}} + \langle u_i' u_i' \rangle_{\mathrm{C}_{\beta\gamma}} + \langle u_i' u_i' \rangle_{\mathrm{C}_{\gamma\alpha}} + \langle u_i' u_i' \rangle_{\mathrm{D}_{\alpha\beta\gamma}}, \end{aligned} \qquad \text{(A.22)}$$

where

$$\langle u_i' u_i' \rangle_{\mathrm{B}_\alpha} = (k_{d,\alpha}\nu)^2 \int_{\hat{k}_{c\alpha}}^{\infty} \hat{E}_{\mathrm{F}}^{1\mathrm{D}}(\hat{k}_\alpha|\ \hat{k}_{c\beta}, \hat{k}_{c\gamma})\ d\hat{k}_\alpha, \tag{A.23a}$$

$$\langle u_i' u_i' \rangle_{\mathrm{C}_{\alpha\beta}} = (k_{d,\alpha}\nu)^2 \int_{\hat{k}_{c\alpha}}^{\infty} \hat{E}_{\mathrm{F}}^{1\mathrm{D}}(\hat{k}_\alpha|\ \hat{k}_{\infty\beta}, \hat{k}_{c\gamma})\ d\hat{k}_\alpha - \langle u_i' u_i' \rangle_{\mathrm{B}_\alpha}, \tag{A.23b}$$

$$\begin{aligned} \langle u_i' u_i' \rangle_{\mathrm{D}_{\alpha\beta\gamma}} &= (k_{d,\alpha}\nu)^2 \int_{\hat{k}_{c\alpha}}^{\infty} \hat{E}_{\mathrm{F}}^{1\mathrm{D}}(\hat{k}_\alpha|\ \hat{k}_{\infty\beta}, \hat{k}_{\infty\gamma})\ d\hat{k}_\alpha \\ &- \langle u_i' u_i' \rangle_{\mathrm{B}_\alpha} - \langle u_i' u_i' \rangle_{\mathrm{C}_{\alpha\beta}} - \langle u_i' u_i' \rangle_{\mathrm{C}_{\alpha\gamma}}, \end{aligned} \tag{A.23c}$$

where α can be x, y, or z, and $\alpha \neq \beta \neq \gamma$, and $\langle u_i' u_i' \rangle_{\mathrm{C}_{\alpha\beta}}$ is the same as $\langle u_i' u_i' \rangle_{\mathrm{C}_{\beta\alpha}}$, and $\langle u_i' u_i' \rangle_{\mathrm{D}_{\alpha\beta\gamma}}$ is the same regardless of the permutation of α, β and γ. Here $\hat{k}_{\infty\beta}$ or $\hat{k}_{\infty\gamma}$ indicates that no filtering has been applied in direction β or γ, respectively, and $\hat{E}_{\mathrm{F}}^{1\mathrm{D}}(\hat{k}_\alpha|\ \hat{k}_{\infty\beta}, \hat{k}_{\infty\gamma}) = \hat{E}^{1\mathrm{D}}(\hat{k}_\alpha)$ is the unfiltered 1D spectrum. As such, equation (A.22) can be simplified as

$$\begin{aligned} \langle \tau_{kk} \rangle = \langle u_i' u_i' \rangle_{\mathrm{SGS}} &= (k_{d,\alpha}\nu)^2 \int_{\hat{k}_{c\alpha}}^{\infty} \hat{E}_{\mathrm{F}}^{1\mathrm{D}}(\hat{k}_\alpha|\ \hat{k}_{\infty\beta}, \hat{k}_{\infty\gamma})\ d\hat{k}_\alpha \\ &+ (k_{d,\beta}\nu)^2 \int_{\hat{k}_{c\beta}}^{\infty} \hat{E}_{\mathrm{F}}^{1\mathrm{D}}(\hat{k}_\beta|\ \hat{k}_{\infty\gamma}, \hat{k}_{c\alpha})\ d\hat{k}_\beta \\ &+ (k_{d,\gamma}\nu)^2 \int_{\hat{k}_{c\gamma}}^{\infty} \hat{E}_{\mathrm{F}}^{1\mathrm{D}}(\hat{k}_\gamma|\ \hat{k}_{c\alpha}, \hat{k}_{c\beta})\ d\hat{k}_\gamma, \end{aligned} \tag{A.24}$$

which gives the same results regardless of permutation of α, β and γ. The first term of the RHS of equation (A.24) represents the sum of TKE in regions B_α, $\mathrm{C}_{\alpha\beta}$, $\mathrm{C}_{\gamma\alpha}$, and $\mathrm{D}_{\alpha\beta\gamma}$, the second term represents the sum of TKE in regions B_β and $\mathrm{C}_{\beta\gamma}$, and the third term represents the TKE in region B_γ.

When filtering is applied only in the the streamwise (k_x) and spanwise (k_y) direc-

tions, as in the present study, the filtering operation divides the spectral space into four regions, as shown in Figure A.7(c) , where α and β denote the streamwise and spanwise direction, respectively, and γ denotes the wall-normal direction, for which no filtering is applied. As no explicit filtering is applied in the wall-normal (k_z) direction, $\hat{k}_{c\gamma}$ would be replaced by $\hat{k}_{\infty\gamma}$ in equation (A.23), and the B_γ, $\mathrm{C}_{\beta\gamma}$, $\mathrm{C}_{\gamma\alpha}$ and $\mathrm{D}_{\alpha\beta\gamma}$ terms in equation (A.22) all vanish. The SGS TKE in the remaining regions B_α, B_β, and $\mathrm{C}_{\alpha\beta}$ can be obtained using equations (A.23a–A.23b) as

$$\langle u_i' u_i' \rangle_{\mathrm{B}_\alpha} = (k_{d,\alpha}\nu)^2 \int_{\hat{k}_{c\alpha}}^{\infty} \hat{E}_{\mathrm{F}}^{1\mathrm{D}}(\hat{k}_\alpha |\ \hat{k}_{c\beta}, \hat{k}_{\infty\gamma})\ d\hat{k}_\alpha, \tag{A.25a}$$

$$\langle u_i' u_i' \rangle_{\mathrm{B}_\beta} = (k_{d,\beta}\nu)^2 \int_{\hat{k}_{c\beta}}^{\infty} \hat{E}_{\mathrm{F}}^{1\mathrm{D}}(\hat{k}_\beta |\ \hat{k}_{c\alpha}, \hat{k}_{\infty\gamma})\ d\hat{k}_\beta, \tag{A.25b}$$

$$\begin{aligned} \langle u_i' u_i' \rangle_{\mathrm{C}_{\alpha\beta}} &= (k_{d,\alpha}\nu)^2 \int_{\hat{k}_{c\alpha}}^{\infty} \hat{E}_{\mathrm{F}}^{1\mathrm{D}}(\hat{k}_\alpha |\ \hat{k}_{\infty\beta}, \hat{k}_{\infty\gamma})\ d\hat{k}_\alpha - \langle u_i' u_i' \rangle_{\mathrm{B}_\alpha}, \\ &= (k_{d,\beta}\nu)^2 \int_{\hat{k}_{c\beta}}^{\infty} \hat{E}_{\mathrm{F}}^{1\mathrm{D}}(\hat{k}_\beta |\ \hat{k}_{\infty\alpha}, \hat{k}_{\infty\gamma})\ d\hat{k}_\beta - \langle u_i' u_i' \rangle_{\mathrm{B}_\beta}. \end{aligned} \tag{A.25c}$$

The contribution from each region to the 1D energy spectrum is shown schematically

in Figure A.7(d). The total SGS TKE can then be evaluated as

$$\langle \tau_{kk} \rangle = \langle u_i' u_i' \rangle_{\mathrm{SGS}} = \langle u_i' u_i' \rangle_{\mathrm{B}_\alpha} + \langle u_i' u_i' \rangle_{\mathrm{B}_\beta} + \langle u_i' u_i' \rangle_{\mathrm{C}_{\alpha\beta}} \tag{A.26a}$$

$$= (k_{d,\alpha}\nu)^2 \int_{\hat{k}_{c\alpha}}^{\infty} \hat{E}_{\mathrm{F}}^{1\mathrm{D}}(\hat{k}_\alpha |\ \hat{k}_{\infty\beta}, \hat{k}_{\infty\gamma})\ d\hat{k}_\alpha$$

$$+ (k_{d,\beta}\nu)^2 \int_{\hat{k}_{c\beta}}^{\infty} \hat{E}_{\mathrm{F}}^{1\mathrm{D}}(\hat{k}_\beta |\ \hat{k}_{c\alpha}, \hat{k}_{\infty\gamma})\ d\hat{k}_\beta, \tag{A.26b}$$

$$= (k_{d,\beta}\nu)^2 \int_{\hat{k}_{c\beta}}^{\infty} \hat{E}_{\mathrm{F}}^{1\mathrm{D}}(\hat{k}_\beta |\ \hat{k}_{\infty\alpha}, \hat{k}_{\infty\gamma})\ d\hat{k}_\beta$$

$$+ (k_{d,\alpha}\nu)^2 \int_{\hat{k}_{c\alpha}}^{\infty} \hat{E}_{\mathrm{F}}^{1\mathrm{D}}(\hat{k}_\alpha |\ \hat{k}_{c\beta}, \hat{k}_{\infty\gamma})\ d\hat{k}_\alpha \tag{A.26c}$$

A.3.2 Evaluation of C_K, α_1, and ϵ_α in LES

Evaluation of the integral (A.20) requires an analytical expression for $\hat{E}^{3\mathrm{D}}(\hat{k})$. In the present study, the formulation (A.13) suggested by *Pao* (1965), or that (A.14–A.15) suggested by *Meyers and Meneveau* (2008) have been employed. The C_K values in either formulation were evaluated by requiring that

$$\int_{\hat{k}_{\min}}^{\hat{k}_{\max}} \hat{E}_{\mathrm{F}}^{1\mathrm{D}}(\hat{k}_\alpha |\ \hat{k}_{c\beta}, \hat{k}_{c\gamma})\ d\hat{k}_\alpha = \int_{\hat{k}_{\min}}^{\hat{k}_{\max}} \hat{E}_{\mathrm{LES}}^{1\mathrm{D}}(\hat{k}_\alpha)\ d\hat{k}_\alpha, \tag{A.27}$$

where $\hat{k}_{\min}$ is in the universal equilibrium range, and $\hat{k}_{\max}$ is the highest wavenumber resolved in LES. Equation (A.27) requires that the normalized TKE in the modelled filtered 1D energy spectra match the 1D energy spectra obtained from LES between the wavenumbers $k_{\min}$ and $k_{\max}$. For the LES cases performed in this study, the value of $\hat{k}_{\min}$ is set either to $\hat{k}_{\min} = 0.07$ or $\hat{k}_{\min} = 0.8\hat{k}_{\max}$, whichever is lower. In general, the former can be used in well-resolved LES, while the latter needs to be used in

coarse-resolution LES.

The spectra obtained from LES, however, do not have a long enough dissipative range to allow calculation of the parameter α_1 in equations (A.13) and (A.14). DNS results, however, show a near-collapse of α_1 at all Reynolds numbers, when plotted as a function of z^+ in the near-wall region ($z^+ \leq 100$), as shown in Figures A.4(a,c), and when plotted as a function of z/h in the outer region ($z^+ > 100$), as shown in Figures A.4(b,d). This Reynolds number independent nature of α_1, allows the values of α_1 in LES at any Reynolds number to be extracted from Figure A.4 and Tables A.1–A.2.

Application of equations (A.20)–(A.26) also requires knowledge of $\langle 3\epsilon_\alpha \rangle$, from which $k_{d,\alpha}$ is determined. In LES, the total rate of TKE dissipation, $\langle \epsilon \rangle$, can be computed using

$$\langle \epsilon \rangle \cong \langle 2\nu \overline{s}'_{ij} \overline{s}'_{ij} + \overline{s}'_{ij} \tau_{ij} \rangle, \tag{A.28}$$

where $\overline{s}'_{ij} = \frac{1}{2}\left(\frac{\partial \overline{u}'_i}{\partial x_j} + \frac{\partial \overline{u}'_j}{\partial x_i}\right)$ is the resolved fluctuating strain rate tensor. However, the breakdown of $\langle \epsilon \rangle$ into $\langle 3\epsilon_\alpha \rangle$ cannot be accurately computed from LES.

The DNS data of turbulent channel flow, shown in Figure A.2, indicate that the profiles of $\langle \epsilon \rangle^+$ and $\langle 3\epsilon_\alpha \rangle^+$ are not universal and display a Reynolds number dependence. However, Figure A.8(a) shows that the profiles of $\langle 3\epsilon_\alpha \rangle / \langle \epsilon \rangle$ collapse for different Reynolds numbers when plotted as function of z^+ in the near-wall region ($z^+ \leq 100$). In the outer region ($z^+ > 100$), the profiles of $\langle 3\epsilon_\alpha \rangle / \langle \epsilon \rangle$ linearly decay from their values at $z^+ = 100$ to their respective centerline values, $[\langle 3\epsilon_\alpha \rangle / \langle \epsilon \rangle]_{CL}$, at each Reynolds number. Thus,

$$G(\langle 3\epsilon_\alpha \rangle / \langle \epsilon \rangle) = \frac{[\langle 3\epsilon_\alpha \rangle / \langle \epsilon \rangle] - [\langle 3\epsilon_\alpha \rangle / \langle \epsilon \rangle]_{\mathrm{CL}}}{[\langle 3\epsilon_\alpha \rangle / \langle \epsilon \rangle]_{z_o^+} - [\langle 3\epsilon_\alpha \rangle / \langle \epsilon \rangle]_{\mathrm{CL}}}\ , \tag{A.29}$$

satisfies

$$G(\langle 3\epsilon_\alpha\rangle/\langle\epsilon\rangle) = \frac{1-z/h}{1-z_o^+/Re_\tau} \tag{A.30}$$

where z_o^+ is the location, $z_o^+ \approx 100$, at which the outer layer behavior begins to manifest.

Figure A.8(b) shows the profiles of $(1-z_o^+/Re_\tau)\ G(\langle 3\epsilon_\alpha\rangle/\langle\epsilon\rangle)$ from DNS databases of turbulent channel flow at $Re_\tau \approx 180$, 550, and 950 (*del Alamo and Jimenez*, 2003; *del Alamo et al.*, 2004). In the outer layer ($z^+ > 100$ or $z/h > 100/Re_\tau$), the profiles of $(1-z_o^+/Re_\tau)\ G(\langle 3\epsilon_\alpha\rangle/\langle\epsilon\rangle)$ at all Reynolds numbers show agreement with the line, $1-z/h$.

Application of equation (A.29) requires knowledge of $[\langle 3\epsilon_\alpha\rangle/\langle\epsilon\rangle]_{CL}$, at the centerline of the channel. Figure A.8(c) shows that the values of $[\langle 3\epsilon_\alpha\rangle/\langle\epsilon\rangle]_{CL}$ show a Reynolds number dependence in DNS databases of turbulent channel flow (*del Alamo and Jimenez*, 2003; *del Alamo et al.*, 2004), as shown in Figure A.8(c), and fit the exponential relation,

$$[\langle 3\epsilon_\alpha\rangle/\langle\epsilon\rangle]_{\mathrm{CL}} = 1 + c_\alpha \exp(-bRe_\tau), \tag{A.31}$$

where $c_x = -0.2828$, $c_y = -0.0775$, $c_z = 0.3603$, and $b = 1.41 \times 10^{-3}$. At high Reynolds numbers, this relation approaches the appropriate limit of $[\langle 3\epsilon_\alpha\rangle/\langle\epsilon\rangle]_{\mathrm{CL}} \to 1$.

Equations (A.28–A.31) allow the profiles of $\langle 3\epsilon_\alpha\rangle/\langle\epsilon\rangle$ to be computed for LES of turbulent channel flow at any Reynolds numbers. In the near-wall region ($z^+ \leq 100$), $\langle 3\epsilon_\alpha\rangle/\langle\epsilon\rangle$ can be obtained from the universal profiles of $\langle 3\epsilon_\alpha\rangle/\langle\epsilon\rangle$ as a function of z^+, as shown in Figure A.8(a) and tabulated in Table A.3. In the outer region ($z^+ > 100$), $\langle 3\epsilon_\alpha\rangle/\langle\epsilon\rangle$ can be obtained from equations (A.29–A.31). Once the profiles of $\langle 3\epsilon_\alpha\rangle/\langle\epsilon\rangle$ are computed, the profiles of $\langle\epsilon_\alpha\rangle$ and $k_{d,\alpha}$ can be computed using the profiles of $\langle\epsilon\rangle$ computed from LES based on equation (A.28).

While the near-wall profile of $\langle 3\epsilon_\alpha \rangle / \langle \epsilon \rangle$, shown in Figure A.8(a) and Table A.3, is expected to be universal for all wall-bounded turbulent flows, the behavior of $\langle 3\epsilon_\alpha \rangle / \langle \epsilon \rangle$ in the outer layer, and specifically the values of the constants c_α in equation (A.31), would probably depend on the type of wall-bounded flow being studied. DNS databases, over a range of Reynolds numbers, will be needed in these other types of flows to derive relations similar to equations (A.30) and (A.31) for these flows.

A.4 Application to Filtered DNS and LES Databases

The accuracy of the SGS TKE recovery procedures described in Section A.3 has been verified by applying these methods to filtered DNS and LES databases. These results are discussed in the present section.

A.4.1 Application to a Filtered DNS Database

Filtered DNS databases represent an 'ideal' case for assessment of accuracy of the SGS TKE recovery procedures described in Section A.3. To this end, ten single-time velocity fields from DNS database of turbulent channel flow at $Re_\tau \approx 550$, performed in a domain size of $L_x \times L_y \times L_z = 8\pi h \times 4\pi h \times 2h$ with resolution $1536 \times 1536 \times 257$ (*del Alamo and Jimenez*, 2003), were filtered in the streamwise and spanwise directions using spectral cut-off filters at 1/12 and 1/8 of the full DNS resolutions, respectively, to obtain a filtered DNS database with a resolution of $\Delta x^+ \approx 107$ and $\Delta y^+ \approx 36$. While these grid spacings would be considered coarse by well-resolved LES standards, the filtering was performed down to these coarse level to provide a more stringent test of the SGS TKE recovery procedures proposed in the present study. The accuracy of the proposed SGS TKE recovery method was examined by comparing the filtered 1D spectra, and the SGS TKE and the RANS stresses recovered from filtered DNS with the corresponding quantities obtained from DNS.

Figure A.9 shows the filtered 1D spectra obtained using equations (A.20–A.21) with $\hat{E}^{3D}(\hat{k})$ formulated using either Pao's spectrum (*Pao*, 1965), or Meyers & Meneveau's spectrum (*Meyers and Meneveau*, 2008), compared to the 1D energy spectra obtained from filtered DNS. The filtered DNS spectra shown in each of the streamwise and spanwise directions include the effect of filtering the other direction. Note that because the DNS velocity field is filtered at different cutoff wavenumbers in the streamwise and spanwise directions, the filtered streamwise and spanwise spectra no longer collapse in the universal equilibrium range, as in Figure A.3. Good agreement is observed between the modelled filtered 1D spectra and the filtered DNS spectra for $k_\alpha/k_{d,\alpha} \geq 0.07$ in both the outer layer (Figure A.9a) and near-wall region (Figure A.9b), verifying the accuracy of the formulations of the filtered 1D energy spectra given by equations (A.20–A.21). The modelled filtered 1D spectra obtained based on Pao's spectrum and Meyers & Meneveau's spectrum nearly overlap in the inertial and dissipation ranges, and both correctly capture the discrepancy between the filtered spectra in the streamwise and spanwise directions in the universal equilibrium range.

Figure A.10 shows the total recovered SGS TKE, $\langle \tau_{kk} \rangle$, computed from equation (A.26), along with its breakdown into regions B_x, B_y, and C_{xy}, computed from equation (A.25a–c), with $\hat{E}^{1D}_F(\hat{k}_\alpha |\ \hat{k}_{c\beta}, \hat{k}_{\infty\gamma})$ evaluated from equations (A.20–A.21) using $\hat{E}^{3D}(\hat{k})$ formulated based on either Pao's spectrum (*Pao*, 1965) or Meyers & Meneveau's spectrum (*Meyers and Meneveau*, 2008), compared to the 'exact' values of each quantity computed from DNS. Nearly identical results are obtained with Paos spectrum and Meyers & Meneveaus spectrum, except for the slightly more accurate recovered total SGS TKE and SGS TKE in region B_x with the latter for $z^+ > 10$. The recovered total SGS TKE is within 10% of DNS values, while the TKE in each of the regions B_x, B_y, and C_{xy} is within 12%, 15%, and 12% of the DNS values, with both Pao's spectrum and Meyers & Meneveau's spectrum, throughout the cross-section of

the channel, as shown in Figure A.10(b).

Once the total SGS TKE, $\langle \tau_{kk} \rangle$, is recovered, the true RANS stresses can be evaluated using equation (A.1), with $\langle \tau_{ij}^* \rangle$ computed exactly from DNS as

$$\langle \tau_{ij}^* \rangle \equiv \langle \overline{u_i u_j} \rangle^* - \langle \overline{u}_i \overline{u}_j \rangle^* \simeq \langle u_i' u_j' \rangle - \langle \overline{u}_i' \overline{u}_j' \rangle - \frac{1}{3} \delta_{ij} (\langle u_k' u_k' \rangle - \langle \overline{u}_k' \overline{u}_k' \rangle), \tag{A.32}$$

where u_i' and $\overline{u}_i'$ denote the fluctuating velocity fields in DNS and filtered DNS, respectively. Figure A.11 shows the RANS turbulence intensities, u_{rms}, v_{rms}, w_{rms}, recovered from filtered DNS using the above procedures. The RANS turbulence intensities are recovered to within 1% of the RANS turbulence intensities in the original DNS database, verifying the accuracy of the proposed methods for recovery of true RANS stresses in this 'ideal' case of filtered DNS.

A.4.2 Results in LES Database

The proposed method for recovery of true RANS stresses is next applied to LES of turbulent channel flow at $Re_\tau \approx 550$ and $Re_\tau \approx 1000$. To this end, two single-domain, conventional LES were performed in channel flows of domain size $L_x = \frac{8}{3}\pi h$ and $L_y = \frac{4}{3}\pi h$. Both channel flows were driven at constant flow rate, with bulk Reynolds numbers, $Re_b \equiv U_b h/\nu$, of 10000 and 20000, corresponding to Re_τ of 554 and 1016, based on the Deans correlation (*Dean*, 1978), respectively. The velocity field was discretized using Fourier series in the streamwise and spanwise directions, and Chebyshev polynomials in the wall-normal direction. The LES equations were advanced in time using a two-step Green's function method, with explicit treatment of the nonlinear and eddy-viscosity terms using a second-order Adams-Bashforth scheme, and implicit treatment of the pressure and viscous terms using a second-order Crank-Nicolson scheme. All the simulations were de-aliased using the so-called 2/3 rule (*Canuto et al.*, 2006). Large eddy simulations were performed with resolu-

tions of $128 \times 128 \times 65$ at $Re_\tau \approx 550$ and $256 \times 256 \times 129$ at $Re_\tau \approx 1000$, resulting in grid spacings of $\Delta_x^+ \approx 36$ and $\Delta_y^+ \approx 18$ at $Re_\tau \approx 550$ and $\Delta_x^+ \approx 32$ and $\Delta_y^+ \approx 16$ at $Re_\tau \approx 1000$. The Dynamic Smagorinsky Model (DSM) (*Germano et al.*, 1991; *Lilly*, 1992), was employed as the SGS model in both simulations. Following the original formulation by *Germano et al.* (1991) and *Lilly* (1992), filtering was performed only in the streamwise and spanwise directions, using spectral, cutoff filters. The implicit spectral cutoff filters were placed at the de-aliased grid filter location, while the test filters were placed at one-half the implicit LES filter locations.

The accuracy of the LES and the proposed methods for recovery of true RANS stresses were assessed by comparisons of the skin-friction coefficient to Dean's correlation (*Dean*, 1978), and comparisons of the turbulent stresses computed in LES and the RANS stresses recovered from LES with filtered and full DNS data in turbulent channel flow at $Re_\tau \approx 550$ (*del Alamo and Jimenez*, 2003) and $Re_\tau \approx 950$ (*del Alamo et al.*, 2004). To obtain the filtered DNS data for comparison with the turbulence statistics obtained in LES, the DNS velocity fields were filtered to resolutions of $\Delta_x^+ \approx 36$ and $\Delta_y^+ \approx 18$ at $Re_\tau \approx 550$, and $\Delta x^+ \approx 32$ and $\Delta y^+ \approx 16$ at $Re_\tau \approx 950$, employed in LES.

The mean velocity profiles predicted in LES are shown in Figures A.12(a,b). Good agreement with DNS is observed at both Reynolds numbers. The corresponding skin-friction coefficients were within 3.8% and 3.3% of the predictions of Dean's correlation (*Dean*, 1978) at $Re_\tau \approx 550$ and $Re_\tau \approx 1000$, respectively. Figures A.12(c,d) show the turbulence intensities, $\langle \overline{u}'_\alpha \overline{u}'_\alpha \rangle^{1/2}$, resolved in LES, and the turbulence intensities, $\langle u'_\alpha u'_\alpha \rangle^{1/2}$, recovered from LES using equation (A.1), with $\hat{E}^{3D}(\hat{k})$ formulated based on Pao's spectrum (*Pao*, 1965) or Meyers & Meneveau's spectrum (*Meyers and Meneveau*, 2008), compared to filtered and full turbulence intensities from DNS. The different formulations of $\hat{E}^{3D}(\hat{k})$ based on Pao's spectrum (*Pao*, 1965) and Meyers

& Meneveau's spectrum (*Meyers and Meneveau*, 2008) gives nearly identical results. The recovered SGS stresses accounts for up to 6%, 8%, and 15% of the total turbulence intensity in the streamwise, spanwise, and wall-normal directions, respectively. Figures A.12(e,f) show the percentage errors in the turbulence intensities predicted in LES, compared to filtered DNS, as well as the percentage errors in the recovered RANS turbulence intensities from LES, compared to full DNS. The percentage errors between the RANS turbulence intensities recovered from LES and DNS results are nearly identical to the errors between LES and filtered DNS results, demonstrating that the SGS TKE recovery procedures do not introduce additional errors. Therefore, the present method for recovery of true RANS stresses can be used as a tool to evaluate the success of LES when only unfiltered reference data is available.

Figure A.13 shows the 1D energy spectra resolved in LES of turbulent channel flow at $Re_\tau \approx 550$ and 1000, and the modelled 1D spectra which extend these spectra into the subgrid scales, compared to the 1D spectra obtained from filtered DNS at $Re_\tau \approx 550$ and 950. The extended modelled 1D spectra show good agreement with the filtered DNS spectra in the subgrid scales. Since the model parameter, C_K, is obtained from the spectra resolved in LES, the extended 1D spectra also reflect the accuracy of the spectra predicted in LES. For example, at both Reynolds numbers, the streamwise and spanwise spectra in the near-wall region ($z^+ \approx 15$), are slightly over-predicted in LES near the highest resolved wavenumbers, and this over-prediction is extended into the subgrid scales by the modelled 1D spectra, as shown in Figures A.13(b,d).

A.5 Summary

In summary, we have developed a method for recovering the SGS TKE and reconstructing the true RANS stresses from LES of wall-bounded turbulence. The

method is based on reconstructing the full one-dimensional (1D) energy spectra from the filtered 1D spectra computed in LES using an analytical formulation of the filtered 1D energy spectra in wall-bounded flows and integrating the areas under the reconstructed spectra to recover the SGS TKE. The accuracy of the method has been demonstrated by application to filtered DNS and LES databases of turbulent channel flow. The proposed methods for recovery of the true RANS stresses allow for meaningful assessment of the capabilities of LES in cases where only unfiltered turbulent stresses are available, as for example, in high Reynolds number flows where DNS data is unavailable and LES need to be assessed based on experimental data.

z^+	C_K^{Pao}	α_1^{Pao}	C_K^{MM}	α_1^{MM}
1	2.003	2.987	1.027	4.864
2	2.531	3.096	1.514	5.151
3	2.806	3.131	1.643	5.178
4	3.101	3.239	1.874	5.228
5	3.227	3.259	2.008	5.351
6	3.548	3.488	2.288	5.554
8	4.002	3.811	2.644	6.265
10	4.275	4.023	2.896	6.465
15	3.961	3.770	2.627	6.067
20	3.566	3.354	2.273	5.550
25	3.264	3.049	2.072	5.064
30	3.016	2.801	1.906	4.799
35	2.889	2.677	1.781	4.550
40	2.822	2.577	1.748	4.442
45	2.795	2.528	1.707	4.378
50	2.778	2.532	1.631	4.394
60	2.751	2.528	1.629	4.385
70	2.755	2.531	1.626	4.387
80	2.758	2.532	1.625	4.388
90	2.759	2.528	1.623	4.385
100	2.761	2.527	1.619	4.384

Table A.1: Model parameters C_K and α_1 in equations (A.13) and (A.14) for Pao's (*Pao*, 1965) and Meyers & Meneveau's (*Meyers and Meneveau*, 2008) spectra as a function of z^+.

z^+	C_K^{Pao}	α_1^{Pao}	C_K^{MM}	α_1^{MM}
0.1	2.825	2.589	1.645	4.559
0.2	2.832	2.635	1.675	4.565
0.3	2.826	2.659	1.681	4.572
0.4	2.824	2.672	1.685	4.594
0.5	2.806	2.651	1.667	4.561
0.6	2.772	2.613	1.638	4.503
0.7	2.725	2.575	1.605	4.451
0.8	2.683	2.537	1.572	4.393
0.9	2.644	2.501	1.544	4.342
1.0	2.618	2.475	1.526	4.307

Table A.2: Model parameters C_K and α_1 in equations (A.13) and (A.14) for Pao's (*Pao*, 1965) and Meyers & Meneveau's (*Meyers and Meneveau*, 2008) spectra as a function of z/h.

z^+	$\langle 3\epsilon_x \rangle / \langle \epsilon \rangle$	$\langle 3\epsilon_y \rangle / \langle \epsilon \rangle$	$\langle 3\epsilon_z \rangle / \langle \epsilon \rangle$
1	0.0014	0.0255	2.9731
2	0.0036	0.0881	2.9083
3	0.0076	0.1833	2.8091
4	0.0292	0.3014	2.6694
5	0.0185	0.4290	2.5525
6	0.0384	0.5624	2.3992
8	0.0429	0.7519	2.2052
10	0.0626	0.8604	2.0770
15	0.1004	1.0254	1.8742
20	0.1360	1.0869	1.7771
25	0.1651	1.1559	1.6790
30	0.2160	1.1714	1.6126
35	0.2440	1.1869	1.5691
40	0.3029	1.1901	1.5070
45	0.3558	1.1776	1.4666
50	0.4039	1.1659	1.4302
60	0.4831	1.1528	1.3641
70	0.5422	1.1341	1.3237
80	0.5801	1.1211	1.2988
90	0.6385	1.0875	1.2740
100	0.6655	1.0819	1.2526

Table A.3: Universal profiles of $\langle 3\epsilon_\alpha \rangle / \langle \epsilon \rangle$ in the inner layer ($z^+ \leq 100$), as a function of z^+.

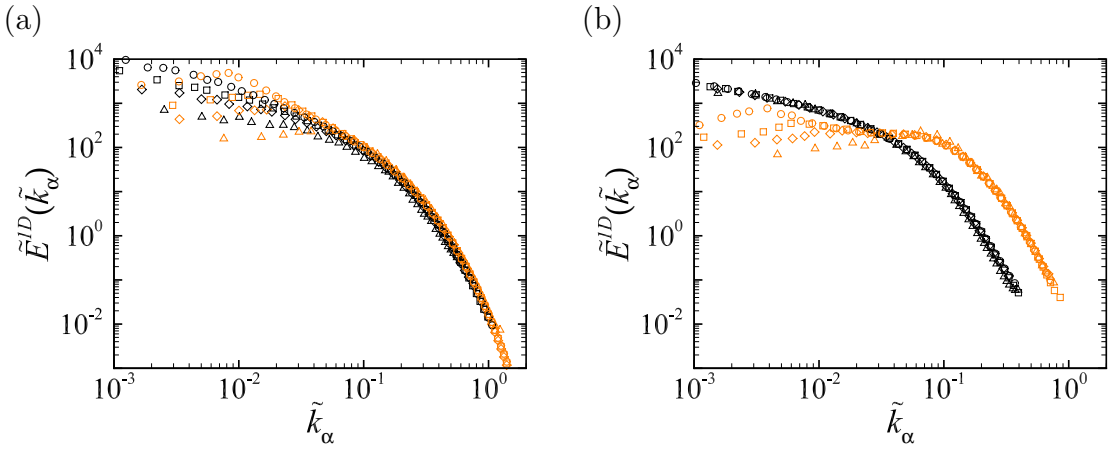

Figure A.1: Normalized one-dimensional energy spectra, $\tilde{E}^{1\mathrm{D}}(\tilde{k}_\alpha)\equiv E^{1\mathrm{D}}(k_\alpha)/(k_d\nu^2)$, in the streamwise and spanwise directions as a function of the normalized wavenumber, $\tilde{k}_\alpha\equiv k_\alpha/k_d\equiv k_\alpha/(\langle\epsilon\rangle/\nu^3)^{\frac{1}{4}}$, from DNS of turbulent channel flow in (a) the outer region ($z/h = 0.5$); (b) the near-wall region ($z^+ \approx 15$). $\triangle$, DNS at $Re_\tau \approx 180$ (*del Alamo and Jimenez*, 2003); $\diamond$, DNS at $Re_\tau \approx 550$ (*del Alamo and Jimenez*, 2003); $\square$, DNS at $Re_\tau \approx 950$ (*del Alamo et al.*, 2004); $\circ$, DNS at $Re_\tau \approx 2000$ (*Hoyas and Jimenez*, 2006); black symbols, streamwise spectra; color (grey) symbols, spanwise spectra.

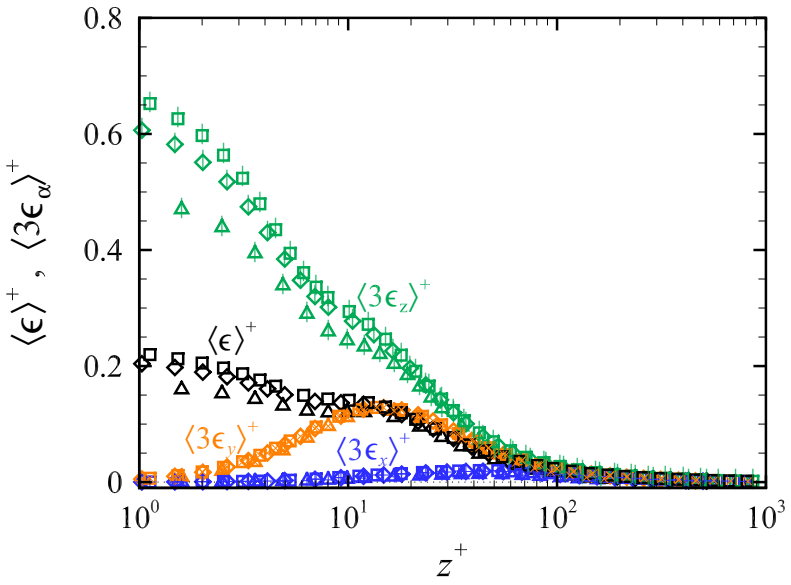

Figure A.2: Profiles of $\langle\epsilon\rangle^+$ and $\langle 3\epsilon_\alpha\rangle^+$ from DNS of turbulent channel flow at $180 \leq Re_\tau \leq 950$. △, $\langle\epsilon\rangle^+$, ⟁, $\langle 3\epsilon_x\rangle^+$, ⟁, $\langle 3\epsilon_y\rangle^+$, ⟁, $\langle 3\epsilon_z\rangle^+$, from DNS at $Re_\tau \approx 180$ (*del Alamo and Jimenez*, 2003); ◇, $\langle\epsilon\rangle^+$, ⟐, $\langle 3\epsilon_x\rangle^+$, ⟐, $\langle 3\epsilon_y\rangle^+$, ⟐, $\langle 3\epsilon_z\rangle^+$, from DNS at $Re_\tau \approx 550$ (*del Alamo and Jimenez*, 2003); □, $\langle\epsilon\rangle^+$, ⊞, $\langle 3\epsilon_x\rangle^+$, ⊠, $\langle 3\epsilon_y\rangle^+$, ⊞, $\langle 3\epsilon_z\rangle^+$, from DNS at $Re_\tau \approx 950$ (*del Alamo et al.*, 2004).

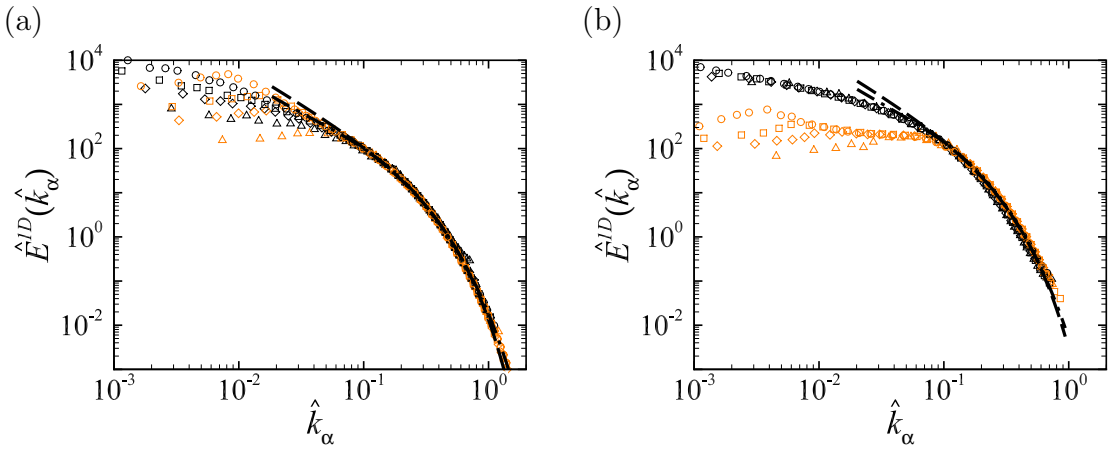

Figure A.3: Normalized one-dimensional energy spectra, $\hat{E}^{1\mathrm{D}}(\hat{k}_\alpha) \equiv E^{1\mathrm{D}}(k_\alpha)/(k_{d,\alpha}\nu^2)$, in the streamwise and spanwise directions as a function of the normalized wavenumber, $\hat{k}_\alpha \equiv k_\alpha/k_{d,\alpha} \equiv k_\alpha/(\langle 3\epsilon_\alpha \rangle/\nu^3)^{\frac{1}{4}}$, from DNS of turbulent channel flow: (a) spectra in the outer region ($z/h = 0.5$); (b) spectra in the near-wall region ($z^+ \approx 15$). — —, $\hat{E}^{1\mathrm{D}}(\hat{k}_\alpha)$ computed from equations (A.11) and (A.16), using $\hat{E}^{3\mathrm{D}}(\hat{k})$ formulated based on Pao's spectrum (*Pao*, 1965); – · –, $\hat{E}^{1\mathrm{D}}(\hat{k}_\alpha)$ computed from equations (A.11) and (A.16), using $\hat{E}^{3\mathrm{D}}(\hat{k})$ formulated based on Meyers & Meneveau's spectrum (*Meyers and Meneveau*, 2008); Symbols as in Figure A.1.

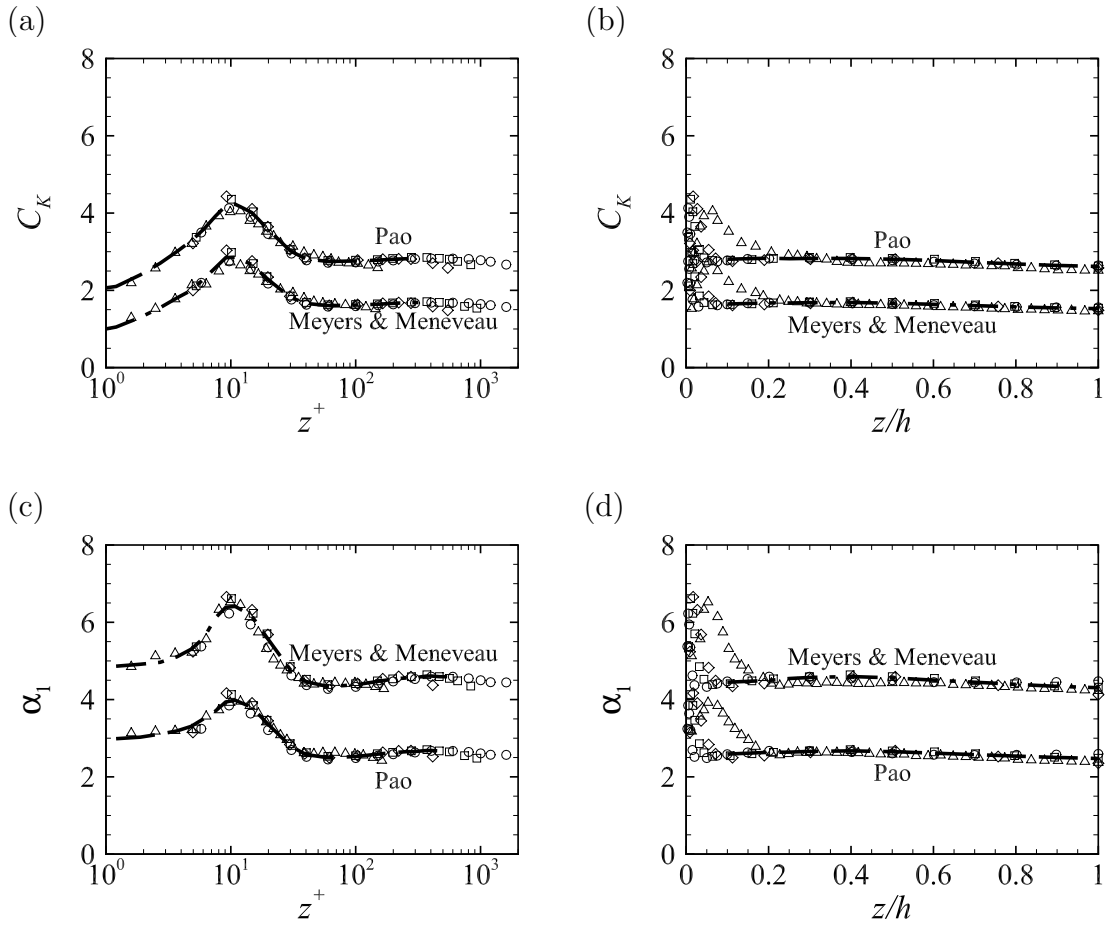

Figure A.4: Model parameters C_K and α_1 in equations (A.13) and (A.14) for Pao's (*Pao*, 1965) and Meyers & Meneveau's (*Meyers and Meneveau*, 2008) spectra obtained from DNS databases of turbulent channel flow with $180 \leq Re_\tau \leq 2000$ (*del Alamo and Jimenez*, 2003; *del Alamo et al.*, 2004; *Hoyas and Jimenez*, 2006) as a function of z^+ and z/h. Symbols as in Figure A.1, lines, least-squares fits to C_K and α_1 from DNS.

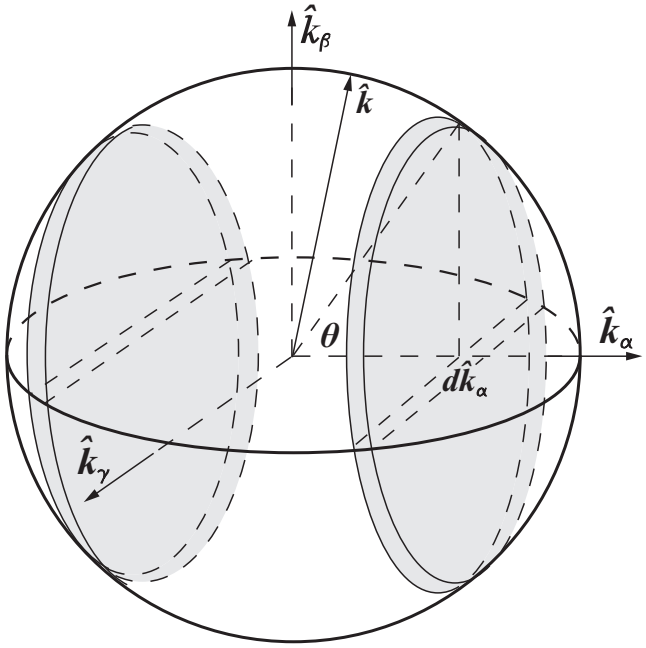

Figure A.5: Geometric interpretation of the relation between 3D spectrum and 1D spectrum given by equation (A.11).

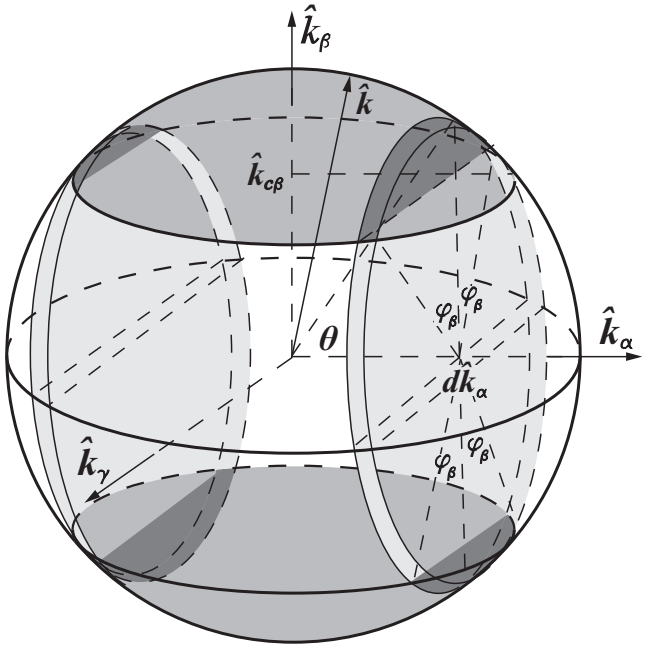

Figure A.6: Effect of spectral cut-off filter in the $\hat{k}_\beta$-direction on the spectral energy contained in the 1D spectrum in the $\hat{k}_\alpha$ direction; the effect of filtering in the $\hat{k}_\gamma$-direction is not included for graphic clarity.

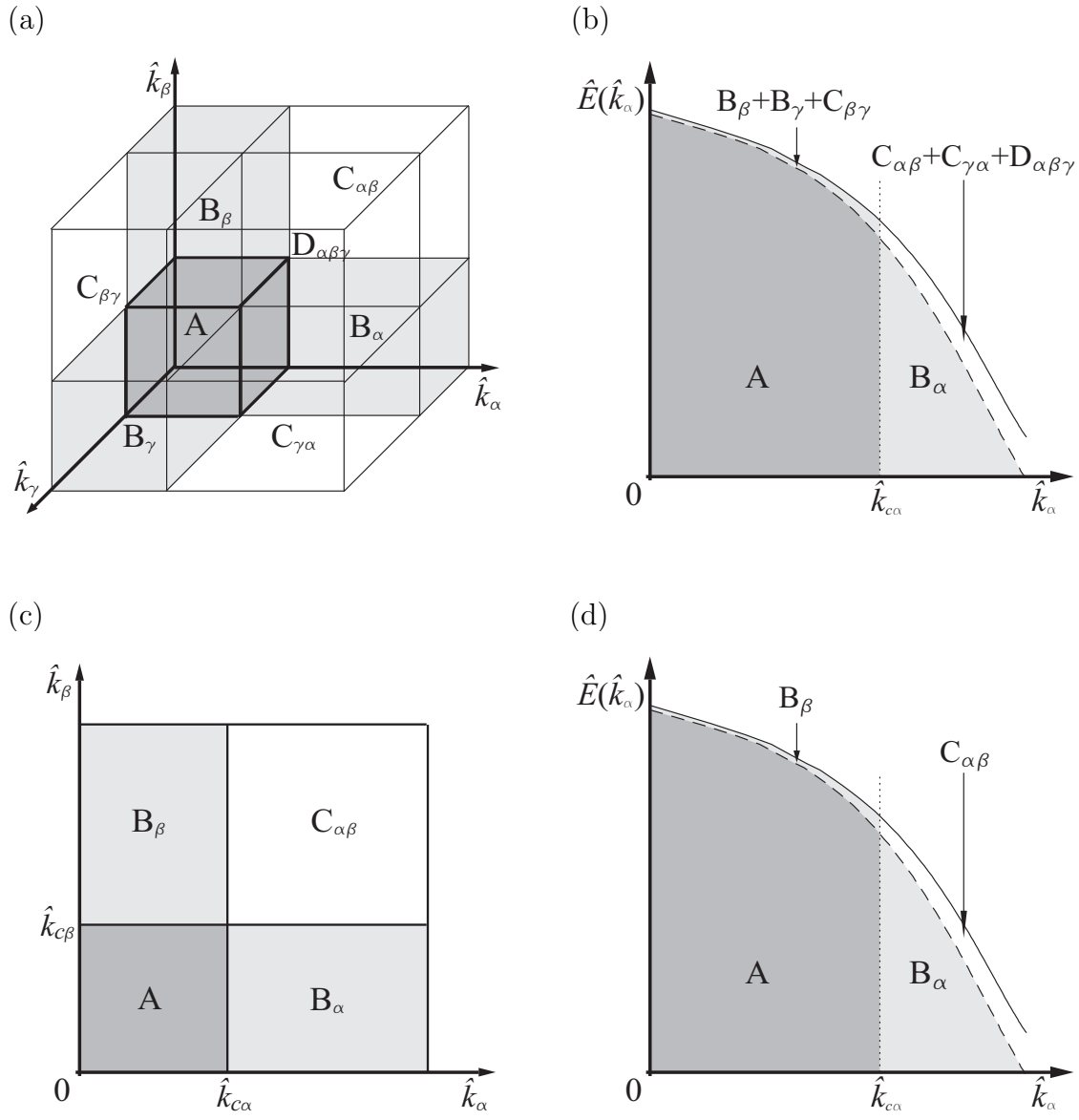

Figure A.7: (a) Partitioning of the spectral space when the flow field is filtered in all three directions; (b) the effect of filtering in the $\hat{k}_\beta$-and $\hat{k}_\gamma$-directions on the 1D spectrum in the $\hat{k}_\alpha$ direction; (c) partitioning of the spectral space when the flow field is filtered in two directions; (d) the effect of the filtering in the $\hat{k}_\beta$-direction on the 1D spectrum in the $\hat{k}_\alpha$ direction. Lines in (b,d): ——, unfiltered 1D spectrum; – – –, filtered 1D spectrum.

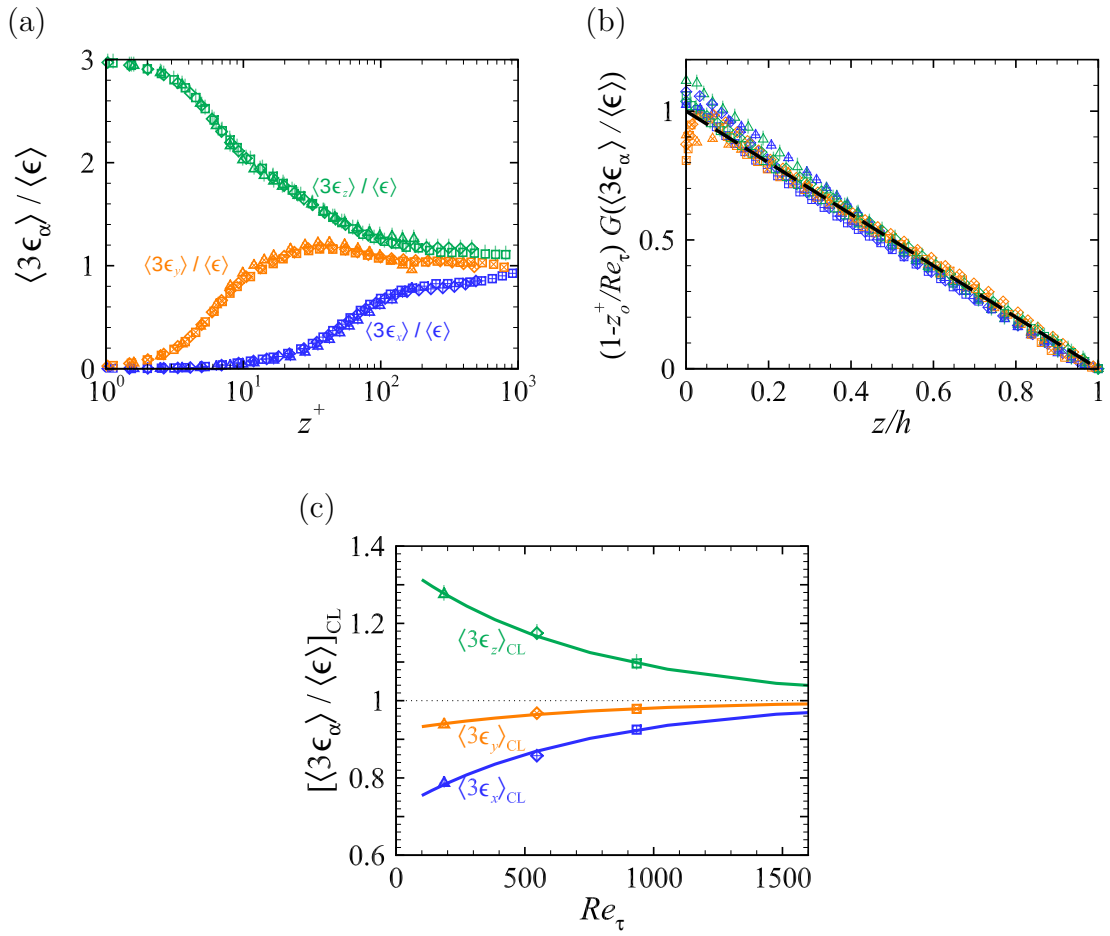

Figure A.8: (a) Profiles of $\langle 3\epsilon_\alpha \rangle / \langle \epsilon \rangle$ as a function of z^+; (b) profiles of $(1 - z_o^+/Re_\tau)\, G(\langle 3\epsilon_\alpha \rangle / \langle \epsilon \rangle)$ as a function of z/h; (c) centerline values of $\langle 3\epsilon_\alpha \rangle / \langle \epsilon \rangle$ as a function of Re_τ. Symbols as in Figure A.2; – – –, high Reynolds number asymptote of $(1 - z_o^+/Re_\tau)\, G(\langle 3\epsilon_\alpha \rangle / \langle \epsilon \rangle)$ in the outer layer; ——, analytical fit to the centerline values of $\langle 3\epsilon_\alpha \rangle / \langle \epsilon \rangle$ given by equation (A.31).

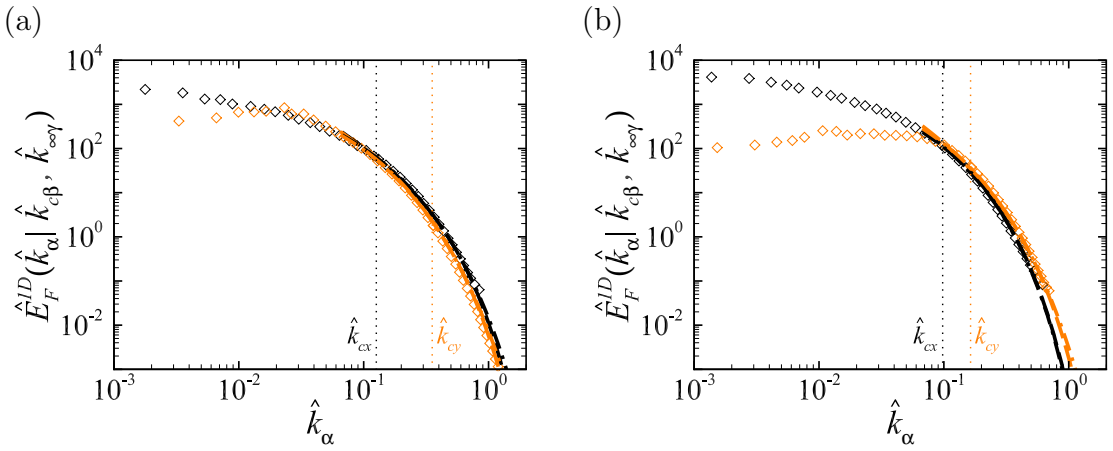

Figure A.9: Modelled filtered 1D energy spectra obtained from equations (A.20-A.21), compared to filtered DNS spectra in turbulent channel flow: (a) spectra in the outer region ($z/h = 0.5$); (b) spectra in the near-wall region ($z^+ \approx 15$). black symbol and lines, spectra in the streamwise direction; color symbol and lines, spectra in the spanwise direction; — —, $\hat{E}_{\mathrm{F}}^{1\mathrm{D}}(\hat{k}_\alpha|\ \hat{k}_{c\beta},\hat{k}_{\infty\gamma})$ obtained using $\hat{E}^{3\mathrm{D}}(\hat{k})$ formulated based on Pao's spectrum (*Pao*, 1965); $-\cdot-$, $\hat{E}_{\mathrm{F}}^{1\mathrm{D}}(\hat{k}_\alpha|\ \hat{k}_{c\beta},\hat{k}_{\infty\gamma})$ obtained using $\hat{E}^{3\mathrm{D}}(\hat{k})$ formulated based on Meyers & Meneveau's spectrum (*Meyers and Meneveau*, 2008); $\diamond$, filtered DNS at $Re_\tau \approx 550$ (*del Alamo and Jimenez*, 2003). Note that the spectra in the streamwise and spanwise directions no longer overlap in the dissipative range due to the different filtering levels employed in $\hat{k}_x$- and $\hat{k}_y$-directions.

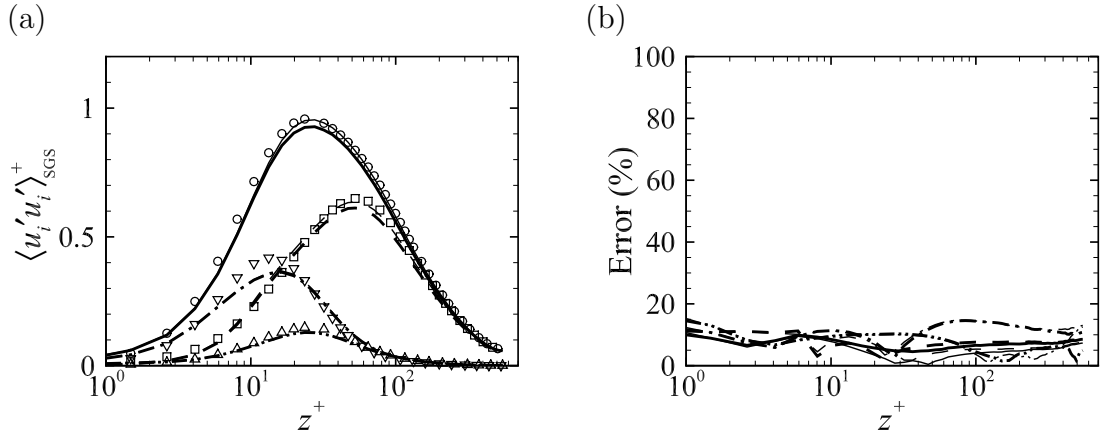

Figure A.10: (a) Total recovered SGS TKE and its breakdown in regions B_x, B_y, and C_{xy}, compared to exact values from DNS of turbulent channel flow at $Re_\tau \approx 550$ (*del Alamo and Jimenez*, 2003); (b) percentage errors in recovery of total SGS TKE, and the SGS TKE in each of regions B_x, B_y, and C_{xy}, compared to the exact DNS values. Thick lines, SGS TKE recovered from integration of equations (A.20) and (A.25–A.26) with $\hat{E}^{3D}(\hat{k})$ formulated based on Pao's spectrum (*Pao*, 1965); thin lines, SGS TKE recovered from integration of equations (A.20) and (A.25–A.26) with $\hat{E}^{3D}(\hat{k})$ formulated based on Meyers & Meneveau's spectrum (*Meyers and Meneveau*, 2008); symbols, quantities as computed from DNS; ——, ○, total recovered SGS TKE; − − −, □, SGS TKE recovered in region B_x; −·−, ▽, SGS TKE recovered in region B_y; −··−, △, SGS TKE recovered in region C_{xy}.

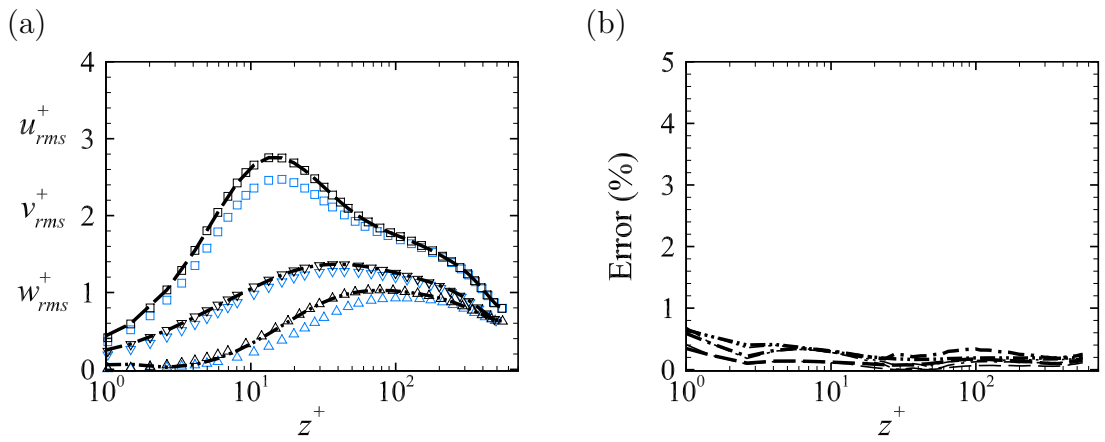

Figure A.11: (a) Profiles of RANS turbulence intensities recovered from filtered DNS at $Re_\tau \approx 550$ (*del Alamo and Jimenez*, 2003), compared to DNS; (b) percentage errors in the recovered RANS turbulence intensities compared to DNS. $--$, $\square$, streamwise turbulence intensity; $-\cdot-$, $\triangledown$, spanwise turbulence intensity; $-\cdot\cdot-$, $\triangle$, wall-normal turbulence intensity; black symbols, DNS; color (grey) symbols, filtered DNS; thick lines, turbulence intensities recovered based on the formulation of $\hat{E}^{3D}(\hat{k})$ suggested by *Pao* (1965); thin lines, turbulence intensities recovered based on the formulation of $\hat{E}^{3D}(\hat{k})$ suggested by *Meyers and Meneveau* (2008).

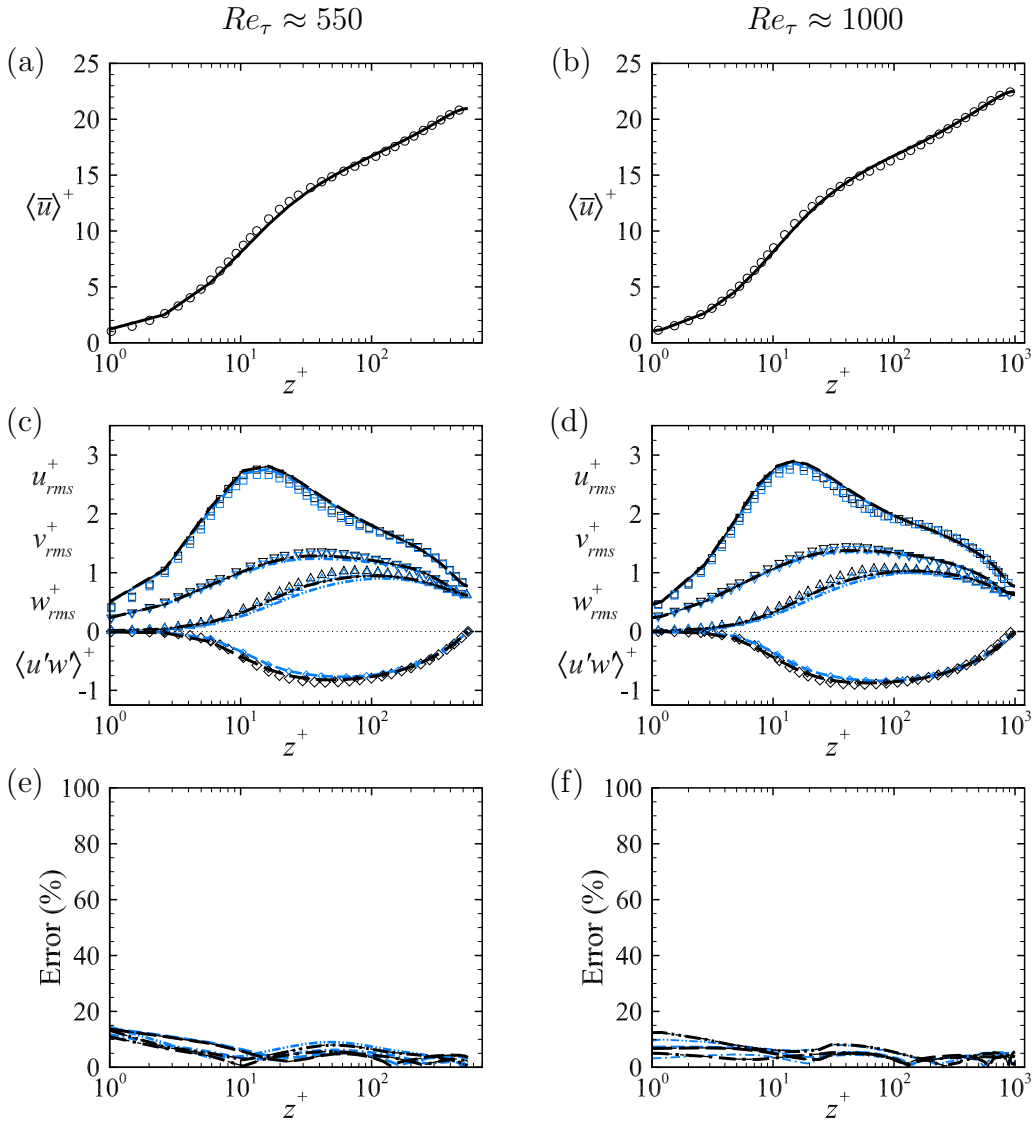

Figure A.12: Profiles of (a,b) mean velocity, (c,d) turbulence intensities and the Reynolds shear stress, (e,f) percentage errors in turbulence intensities computed in LES and RANS turbulence intensities recovered from LES, compared to filtered and full DNS, respectively: (a,c,e) $Re_\tau \approx 550$, (b,d,f) $Re_\tau \approx 1000$. ——, – – –, – · –, – ·· –, – ◇ –, mean velocity, turbulence intensities, $\langle \overline{u}'\overline{u}' \rangle^{1/2}$, $\langle \overline{v}'\overline{v}' \rangle^{1/2}$, $\langle \overline{w}'\overline{w}' \rangle^{1/2}$, and the Reynolds shear stress, $\langle \overline{u}'\overline{w}' \rangle$, computed in LES, respectively; — —, — · —, — ·· —, — ◇ —, RANS turbulence intensities, $\langle u'^2 \rangle^{1/2}$, $\langle v'^2 \rangle^{1/2}$, $\langle w'^2 \rangle^{1/2}$, and the Reynolds shear stress, $\langle u'w' \rangle$, recovered from LES using either Pao's (*Pao*, 1965) formulation (thick lines) or Meyers and Meneveau's (*Meyers and Meneveau*, 2008) formulation (thin lines) for $\hat{E}^{3D}(\hat{k})$; ○, □, ▽, △, ◇, mean velocity, turbulence intensities, $\langle u'^2 \rangle^{1/2}$, $\langle v'^2 \rangle^{1/2}$, $\langle w'^2 \rangle^{1/2}$, and the Reynolds shear stress, $\langle u'w' \rangle$, respectively, from DNS at $Re_\tau \approx 550$ (*del Alamo and Jimenez*, 2003) and $Re_\tau \approx 950$ (*del Alamo et al.*, 2004); □, ▽, △, ◇, turbulence intensities, $\langle \overline{u}'\overline{u}' \rangle^{1/2}$, $\langle \overline{v}'\overline{v}' \rangle^{1/2}$, $\langle \overline{w}'\overline{w}' \rangle^{1/2}$, and the Reynolds shear stress, $\langle \overline{u}'\overline{w}' \rangle$, from filtered DNS.

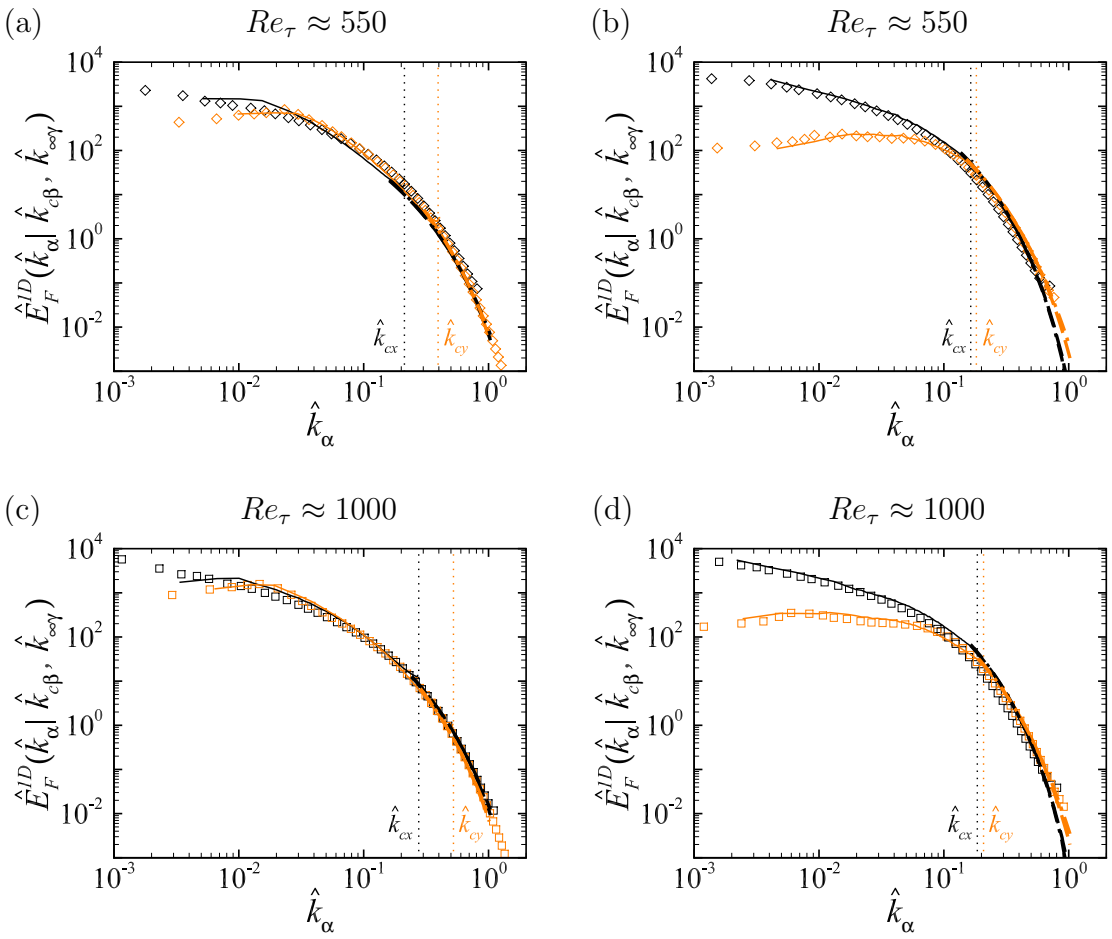

Figure A.13: Modelled filtered 1D energy spectra from LES turbulent channel flow at $Re_\tau \approx 550$ and $Re_\tau \approx 1000$ extended into subgrid scales down to the Kolmogorov scale, compared to filtered DNS (*del Alamo and Jimenez*, 2003; *del Alamo et al.*, 2004): (a,b) spectra at $Re_\tau \approx 550$ in the outer region ($z/h = 0.5$) and near-wall region ($z^+ \approx 15$), respectively; (c,d) spectra at $Re_\tau \approx 1000$ in the outer region ($z/h = 0.5$) and near-wall region ($z^+ \approx 15$), respectively. black symbols and lines, spectra in the streamwise direction; color (grey) symbols and lines, spectra in the spanwise direction; ——, 1D energy spectra resolved in LES; — —, $\hat{E}_{\mathrm{F}}^{1\mathrm{D}}(\hat{k}_\alpha|\ \hat{k}_{c\beta}, \hat{k}_{\infty\gamma})$ obtained using $\hat{E}^{3\mathrm{D}}(\hat{k})$ formulated using Pao's spectrum (*Pao*, 1965); –·–, $\hat{E}_{\mathrm{F}}^{1\mathrm{D}}(\hat{k}_\alpha|\ \hat{k}_{c\beta}, \hat{k}_{\infty\gamma})$ obtained using $\hat{E}^{3\mathrm{D}}(\hat{k})$ formulated using Meyers & Meneveau's spectrum (*Meyers and Meneveau*, 2008); ◇, filtered DNS at $Re_\tau \approx 550$; □, filtered DNS at $Re_\tau \approx 950$.

BIBLIOGRAPHY

BIBLIOGRAPHY

Adrian, R. J. (2007), Hairpin vortex organization in wall turbulence, *Phys. Fluids*, *19*(4), 041 301.

Balakumar, B. J., and R. J. Adrian (2007), Large- and very-large-scale motions in channel and boundary-layer flows, *Philos. T. Roy. Soc. B*, *365*(1852), 665–681.

Balaras, E., C. Benocci, and U. Piomelli (1996), Two-layer approximate boundary conditions for large-eddy simulations, *AIAA J.*, *34*(6), 1111–1119.

Bardina, J., J. H. Ferziger, and W. C. Reynolds (1980), Improved subgrid-scale models for large-eddy simulation, *AIAA P.*, pp. 80–1357.

Blackburn, H. M., and S. Schmidt (2003), Spectral element filtering techniques for large eddy simulation with dynamic estimation, *J. Comput. Phys.*, *186*(2), 610–629.

Cabot, W., and P. Moin (1999), Approximate wall boundary conditions in the large-eddy simulation of high Reynolds number flow, *Flow Turbul. Combust.*, *63*(1), 269–291.

Canuto, C., M. Y. Hussaini, A. Quarteroni, and T. A. Zang (2007), *Spectral methods: evolution to complex geometries and applications to fluid dynamics*, Scientific computation, Springer.

Canuto, C. G., M. Y. Hussaini, A. Quarteroni, and T. A. Zang (2006), *Spectral methods: fundamentals in single domains*, Scientific computation, Springer.

Chapman, D. R. (1979), Computational aerodynamics, development and outlook, *AIAA J.*, *17*(12), 1293–1313.

Chung, D., and D. I. Pullin (2009), Large-eddy simulation and wall modelling of turbulent channel flow, *J. Fluid Mech.*, *631*, 281–309.

Coleman, G. N., J. Kim, and A. T. Le (1996), A numerical study of three-dimensional wall-bounded flows, *Int. J. Heat Fluid Fl.*, *17*(3), 333–342.

Comte-Bellot, G. (1963), Turbulent flow between two parallel walls, Ph.D. thesis, University of Grenoble.

Dean, R. B. (1978), Reynolds number dependence of skin friction and other bulk flow variables in two-dimensional rectangular duct flow, *J. Fluid. Eng.-T. ASME*, *100*(2), 215–223.

Deardorff, J. W. (1970), A numerical study of three-dimensional turbulent channel flow at large Reynolds numbers, *J. Fluid Mech.*, *41*, 453.

del Alamo, J. C., and J. Jimenez (2003), Spectra of the very large anisotropic scales in turbulent channels, *Phys. Fluids*, *15*(6), L41–L44.

del Alamo, J. C., and J. Jimenez (2009), Estimation of turbulent convection velocities and corrections to Taylor's approximation, *J. Fluid Mech.*, *640*, 5–26.

del Alamo, J. C., J. Jimenez, P. Zandonade, and R. D. Moser (2004), Scaling of the energy spectra of turbulent channels, *J. Fluid Mech.*, *500*, 135–144.

Driver, D. M., and S. K. Hebbar (1987), Experimental study of a three-dimensional, shear-driven, turbulent boundary layer, *AIAA J.*, *25*(1), 35–42.

Driver, D. M., and S. K. Hebbar (1991), Three-dimensional turbulent boundary layer flow over a spinning cylinder, *Tech. Rep. NASA-TM-102240*, NASA, AMES Research Center.

Egorov, Y., F. R. Menter, R. Lechner, and D. Cokljat (2010), The Scale-Adaptive Simulation Method for Unsteady Turbulent Flow Predictions. Part 2: Application to Complex Flows, *Flow Turbul. Combust.*, *85*(1), 139–165.

Flores, O., and J. Jimenez (2010), Hierarchy of minimal flow units in the logarithmic layer, *Phys. Fluids*, *22*(7), 071 704.

Frohlich, J., and D. von Terzi (2008), Hybrid LES/RANS methods for the simulation of turbulent flows, *Prog. Aerosp. Sci.*, *44*(5), 349–377.

Funaro, D., A. Quarteroni, and P. Zanolli (1988), An iterative procedure with interface relaxation for domain decomposition methods, *SIAM J. Numer. Anal.*, *25*(6), 1213–1236.

Georgiadis, N. J., D. P. Rizzetta, and C. Fureby (2010), Large-eddy simulation: current capabilities, recommended practices, and future research, *AIAA J.*, *48*(8), 1772–1784.

Germano, M., U. Piomelli, P. Moin, and W. H. Cabot (1991), A dynamic subgrid-scale eddy viscosity model, *Phys. Fluids A-Fluid*, *3*(7), 1760–1765.

Ghosal, S., T. S. Lund, P. Moin, and K. Akselvoll (1995), A dynamic localization model for large-eddy simulation of turbulent flows, *J. Fluid Mech.*, *286*, 229–255.

Guala, M., S. E. Hommema, and R. J. Adrian (2006), Large-scale and very-large-scale motions in turbulent pipe flow, *J. Fluid Mech.*, *554*, 521–542.

Gungor, A. G., and S. Menon (2006), Direct simulation of subgrid turbulence in high-Re, wall-bounded flows, *AIAA P.*, pp. 2006–3538.

Gungor, A. G., and S. Menon (2010), A new two-scale model for large eddy simulation of wall-bounded flows, *Prog. Aerosp. Sci.*, *46*(1), 28–45.

Haidvogel, D. B., and T. Zang (1979), The accurate solution of poisson's equation by expansion in chebyshev polynomials, *J. Comput. Phys.*, *30*(2), 167–180.

Haliloglu, M. U. (2007), A multi-scale, multi-domain approach to wall-modelling for LES of high Reynolds number wall-bounded turbulent flows, Ph.D. thesis, University of Michigan.

Hamba, F. (2006), A hybrid RANS/LES simulation of high-Reynolds-number channel flow using additional filtering at the interface, *Theor. Comp. Fluid Dyn.*, *20*(2), 89–101.

Hinze, J. O. (1975), *Turbulence*, McGraw-Hill series in mechanical engineering, 2nd ed., McGraw-Hill.

Hoffmann, G., and C. Benocci (1995), Approximate wall boundary conditions for large eddy simulations, in *"Advances in turbulence V"*, edited by R. Benzi, pp. 222–228, Kluwer.

Hoyas, S., and J. Jimenez (2006), Scaling of the velocity fluctuations in turbulent channels up to Re-tau=2003, *Phys. Fluids*, *18*(1), 011 702.

Hultmark, M., M. Vallikivi, S. C. C. Bailey, and A. J. Smits (2013), Logarithmic scaling of turbulence in smooth- and rough-wall pipe flow, *J. Fluid Mech.*, *728*, 376–395.

Hutchins, N., and I. Marusic (2007a), Evidence of very long meandering features in the logarithmic region of turbulent boundary layers, *J. Fluid Mech.*, *579*, 1–28.

Hutchins, N., and I. Marusic (2007b), Large-scale influences in near-wall turbulence, *Philos. T. Roy. Soc. B*, *365*(1852), 647–664.

Hwang, Y. Y. (2013), Near-wall turbulent fluctuations in the absence of wide outer motions, *J. Fluid Mech.*, *723*, 264–288.

Inoue, M., and D. I. Pullin (2011), Large-eddy simulation of the zero-pressure-gradient turbulent boundary layer up to Re-theta = O(10(12)), *J. Fluid Mech.*, *686*, 507–533.

Israeli, M., L. Vozovoi, and A. Averbuch (1993), Spectral multidomain technique with Local Fourier Basis, *J. Sci. Comput.*, *8*(2), 135–149.

Jimenez, J. (2003), Computing high-Reynolds-number turbulence: will simulations ever replace experiments?, *J. Turbul.*, *4*, N22.

Jimenez, J., and S. Hoyas (2008), Turbulent fluctuations above the buffer layer of wall-bounded flows, *J. Fluid Mech.*, *611*, 215–236.

Jimenez, J., and P. Moin (1991), The minimal flow unit in near-wall turbulence, *J. Fluid Mech.*, *225*, 213–240.

Jimenez, J., and A. Pinelli (1999), The autonomous cycle of near-wall turbulence, *J. Fluid Mech.*, *389*, 335–359.

Jimenez, J., S. Hoyas, M. P. Simens, and Y. Mizuno (2010), Turbulent boundary layers and channels at moderate Reynolds numbers, *J. Fluid Mech.*, *657*, 335–360.

Kallinderis, Y. (1992), Numerical treatment of grid interfaces for viscous flows, *J. Comput. Phys.*, *98*(1), 129–144.

Kang, S. (1996), Spectral domain-decomposition methods for LES of turbulence in wall-bounded flows, Ph.D. thesis, University of Michigan.

Kannepalli, C., and U. Piomelli (2000), Large-eddy simulation of a three-dimensional shear-driven turbulent boundary layer, *J. Fluid Mech.*, *423*, 175–203.

Keating, A., and U. Piomelli (2006), A dynamic stochastic forcing method as a wall-layer model for large-eddy simulation, *J. Turbul.*, *7*(12), 1–24.

Kemenov, K., and S. Menon (2003), Two level simulation of high-Reynolds number non-homogeneous turbulent flows, *AIAA P.*, pp. 2003–0084.

Kiesow, R. O., and M. W. Plesniak (2003), Near-wall physics of a shear-driven three-dimensional turbulent boundary layer with varying crossflow, *J. Fluid Mech.*, *484*, 1–39.

Kim, W.-W., and S. Menon (1995), A new dynamic one-equation subgrid-scale model for large eddy simulations, *AIAA P.*, pp. 95–0356.

Knaepen, B., O. Debliquy, and D. Carati (2002), Subgrid-scale energy and pseudo pressure in large-eddy simulation, *Phys. Fluids*, *14*(12), 4235–4241.

Kosloff, D., and H. Talezer (1993), A modified Chebyshev pseudospectral method with an O(1/N) time step restriction, *J. Comput. Phys.*, *104*(2), 457–469.

Kraichnan, R. H. (1959), The structure of isotropic turbulence at very high Reynolds numbers, *J. Fluid Mech.*, *5*(4), 497–543.

Kravchenko, A. G., P. Moin, and R. Moser (1996), Zonal embedded grids for numerical simulations of wall-bounded turbulent flows, *J. Comput. Phys.*, *127*(2), 412–423.

Lee, M., and R. D. Moser (2015), Direct numerical simulation of turbulent channel flow up to $Re_\tau = 5200$, *J. Fluid Mech.*, (Submitted).

Lilly, D. K. (1992), A proposed modification of the Germano subgrid-scale closure method, *Phys. Fluids A-Fluid*, *4*(3), 633–635.

Marusic, I., and W. D. C. Heuer (2007), Reynolds number invariance of the structure inclination angle in wall turbulence, *Phys. Rev. Lett.*, *99*(11).

Marusic, I., R. Mathis, and N. Hutchins (2010a), High Reynolds number effects in wall turbulence, *Int. J. Heat Fluid Fl.*, *31*(3), 418–428.

Marusic, I., R. Mathis, and N. Hutchins (2010b), Predictive model for wall-bounded turbulent flow, *Science*, *329*(5988), 193–196.

Marusic, I., B. J. McKeon, P. A. Monkewitz, H. M. Nagib, A. J. Smits, and K. R. Sreenivasan (2010c), Wall-bounded turbulent flows at high Reynolds numbers: recent advances and key issues, *Phys. Fluids*, *22*(6), 065 103.

Marusic, I., J. P. Monty, M. Hultmark, and A. J. Smits (2013), On the logarithmic region in wall turbulence, *J. Fluid Mech.*, *716*.

Mason, P. J., and N. S. Callen (1986), On the magnitude of the subgrid-scale eddy coefficient in large-eddy simulations of turbulent channel flow, *J. Fluid Mech.*, *162*, 439–462.

Mathis, R., N. Hutchins, and I. Marusic (2009), Large-scale amplitude modulation of the small-scale structures in turbulent boundary layers, *J. Fluid Mech.*, *628*, 311–337.

Mathis, R., N. Hutchins, and I. Marusic (2011), A predictive inner-outer model for streamwise turbulence statistics in wall-bounded flows, *J. Fluid Mech.*, *681*, 537–566.

Mathis, R., I. Marusic, S. I. Chernyshenko, and N. Hutchins (2013), Estimating wall-shear-stress fluctuations given an outer region input, *J. Fluid Mech.*, *715*, 163–180.

Meneveau, C., and I. Marusic (2013), Generalized logarithmic law for high-order moments in turbulent boundary layers, *J. Fluid Mech.*, *719*.

Menter, F., A. Garbaruk, P. Smirnov, D. Cokljat, and F. Mathey (2010a), Scale-adaptive simulation with artificial forcing, in *"Progress in Hybrid RANS-LES Modelling"*, pp. 235–246, Springer.

Menter, F., A. Garbaruk, P. Smirnov, D. Cokljat, and F. Mathey (2010b), Scale-Adaptive Simulation with Artificial Forcing, in *"Progress in Hybrid RANS-LES Modelling"*, *Notes on Numerical Fluid Mechanics and Multidisciplinary Design*, vol. 111, edited by S.-H. Peng, P. Doerffer, and W. Haase, pp. 235–246, Springer.

Menter, F. R., and Y. Egorov (2005), A scale-adaptive simulation model using two-equation models, *AIAA P.*, pp. 2005–1095.

Menter, F. R., and Y. Egorov (2010), The Scale-Adaptive Simulation Method for Unsteady Turbulent Flow Predictions. Part 1: Theory and Model Description, *Flow Turbul. Combust.*, *85*(1), 113–138.

Menter, F. R., M. Kuntz, and R. Bender (2003), A scale-adaptive simulation model for turbulent flow predictions, *AIAA P.*, pp. 2003–0767.

Meyers, J., and M. Baelmans (2004), Determination of subfilter energy in large-eddy simulations, *J. Turbul.*, *5*, N26.

Meyers, J., and C. Meneveau (2008), A functional form for the energy spectrum parametrizing bottleneck and intermittency effects, *Phys. Fluids*, *20*(6), 065 109.

Misra, A., and D. I. Pullin (1997), A vortex-based subgrid stress model for large-eddy simulation, *Phys. Fluids*, *9*(8), 2443–2454.

Mizuno, Y., and J. Jimenez (2013), Wall turbulence without walls, *J. Fluid Mech.*, *723*, 429–455.

Moin, P., K. Squires, W. Cabot, and S. Lee (1991), A dynamic subgrid-scale model for compressible turbulence and scalar transport, *Phys. Fluids A-Fluid*, *3*(11), 2746–2757.

Orszag, S. A. (1980), Spectral methods for problems in complex geometries, *J. Comput. Phys.*, *37*(1), 70–92.

Pao, Y. H. (1965), Structure of turbulent velocity and scalar fields at large wavenumbers, *Phys. Fluids*, *8*(6), 1063–1075.

Pascarelli, A., U. Piomelli, and G. V. Candler (2000), Multi-block large-eddy simulations of turbulent boundary layers, *J. Comput. Phys.*, *157*(1), 256–279.

Perry, A. E., S. Henbest, and M. S. Chong (1986), A theoretical and experimental-study of wall turbulence, *J. Fluid Mech.*, *165*, 163–199.

Piomelli, U. (2008), Wall-layer models for large-eddy simulations, *Prog. Aerosp. Sci.*, *44*(6), 437–446.

Piomelli, U., and E. Balaras (2002), Wall-layer models for large-eddy simulations, *Annu. Rev. Fluid Mech.*, *34*, 349–374.

Piomelli, U., J. Ferziger, P. Moin, and J. Kim (1989), New approximate boundary-conditions for large eddy simulations of wall-bounded flows, *Phys. Fluids A-Fluid*, *1*(6), 1061–1068.

Piomelli, U., S. Radhakrishnan, L. Zhong, and M. Li (2007), Wall-layer models for large-eddy simulations of high Reynolds number non-equilibrium flows, in *"Advances in Turbulence XI"*, *Springer Proceedings Physics*, vol. 117, edited by J. M. L. M. Palma and A. S. Lopes, pp. 47–54, Springer.

Pope, S. B. (2000), *Turbulent flows*, 1st ed., Cambridge University Press.

Radhakrishnan, S., U. Piomelli, A. Keating, and A. S. Lopes (2006), Reynolds-averaged and large-eddy simulations of turbulent non-equilibrium flows, *J. Turbul.*, *7*(63), 1–30.

Robinson, S. K. (1991), Coherent motions in the turbulent boundary layer, *Annu. Rev. Fluid Mech.*, *23*, 601–639.

Sagaut, P. (2006), *Large eddy simulation for incompressible flows: an introduction*, Scientific computation, 3rd ed., Springer.

Sagaut, P., and S. Deck (2009), Large eddy simulation for aerodynamics: status and perspectives, *Philos. T. Roy. Soc. B*, *367*(1899), 2849–2860.

Salesky, S., and M. Chamecki (2012), A Similarity Model of Subfilter-Scale Energy for Large-Eddy Simulations of the Atmospheric Boundary Layer, *Bound.-Lay. Meteorol.*, *145*(1), 69–91.

Schlatter, P., Q. Li, G. Brethouwer, A. V. Johansson, and D. S. Henningson (2010), Simulations of spatially evolving turbulent boundary layers up to Re[theta]=4300, *Int. J. Heat Fluid Fl.*, *31*(3), 251–261.

Schumann, U. (1975), Subgrid scale model for finite difference simulations of turbulent flows in plane channels and annuli, *J. Comput. Phys.*, *18*(4), 376–404.

Shariff, K., and R. D. Moser (1998), Two-dimensional mesh embedding for B-spline methods, *J. Comput. Phys.*, *145*(2), 471–488.

Sillero, J. A., J. Jimenez, and R. D. Moser (2014), Two-point statistics for turbulent boundary layers and channels at Reynolds numbers up to delta(+) approximate to 2000, *Phys. Fluids*, *26*(10).

Smits, A. J., B. J. McKeon, and I. Marusic (2011), High-Reynolds number wall turbulence, *Annu. Rev. Fluid Mech.*, *43*, 353–375.

Spalart, P. R. (2009), Detached-eddy simulation, *Annu. Rev. Fluid Mech.*, *41*, 181–202.

Spalart, P. R., W.-H. Jou, M. Strelets, and S. R. Allmaras (1997), Comments on the feasibility of LES for wings, and on a hybrid RANS/LES approach, in *"Advances in DNS/LES"*, edited by C. Liu, Z. Liu, and L. Sakell, pp. 137–147, Greyden Press.

Spalart, P. R., S. Deck, M. L. Shur, K. D. Squires, M. K. Strelets, and A. Travin (2006), A new version of detached-eddy simulation, resistant to ambiguous grid densities, *Theor. Comp. Fluid Dyn.*, *20*(3), 181–195.

Stevens, R., M. Wilczek, and C. Meneveau (2014), Large-eddy simulation study of the logarithmic law for second- and higher-order moments in turbulent wall-bounded flow, *J. Fluid Mech.*, *757*, 888–907.

Stolz, S., and N. A. Adams (1999), An approximate deconvolution procedure for large-eddy simulation, *Phys. Fluids*, *11*(7), 1699–1701.

Stolz, S., N. A. Adams, and L. Kleiser (2001), An approximate deconvolution model for large-eddy simulation with application to incompressible wall-bounded flows, *Phys. Fluids*, *13*(4), 997–1015.

Talluru, K. M., R. Baidya, N. Hutchins, and I. Marusic (2014), Amplitude modulation of all three velocity components in turbulent boundary layers, *J. Fluid Mech.*, *746*.

Temmerman, L., M. Hadziabdic, M. A. Leschziner, and K. Hanjalic (2005), A hybrid two-layer URANS-LES approach for large eddy simulation at high Reynolds numbers, *Int. J. Heat Fluid Fl.*, *26*(2), 173–190.

Townsend, A. A. (1958), The turbulent boundary layer, in *"Boundary Layer Research"*, edited by H. Grtler, Internationale Union fr theoretische und angewandte Mechanik / International Union of Theoretical and Applied Mechanics, pp. 1–15, Springer.

Townsend, A. A. (1976), *The structure of turbulent shear flow*, Cambridge monographs on mechanics and applied mathematics, 2d ed., Cambridge University Press.

Voelkl, T., D. I. Pullin, and D. C. Chan (2000), A physical-space version of the stretched-vortex subgrid-stress model for large-eddy simulation, *Phys. Fluids*, *12*(7), 1810–1825.

Wang, M., and P. Moin (2002), Dynamic wall modeling for large-eddy simulation of complex turbulent flows, *Phys. Fluids*, *14*(7), 2043–2051.

Winckelmans, G. S., H. Jeanmart, and D. Carati (2002), On the comparison of turbulence intensities from large-eddy simulation with those from experiment or direct numerical simulation, *Phys. Fluids*, *14*(5), 1809–1811.

Wong, V. C. (1992), A proposed statistical-dynamic closure method for the linear or nonlinear subgrid-scale stresses, *Phys. Fluids A-Fluid*, *4*(5), 1080–1082.

Wong, V. C., and D. K. Lilly (1994), A comparison of two dynamic subgrid closure methods for turbulent thermal-convection, *Phys. Fluids*, *6*(2), 1016–1023.

Wu, Y., and K. T. Christensen (2010), Spatial structure of a turbulent boundary layer with irregular surface roughness, *J. Fluid Mech.*, *655*, 380–418.

Yakhot, A., S. A. Orszag, V. Yakhot, and M. Israeli (1989), Renormalization group formulation of large-eddy simulations, *J. Sci. Comput.*, *4*(2), 139–158.

Yoshizawa, A. (1986), Statistical-theory for compressible turbulent shear flows, with the application to subgrid modeling, *Phys. Fluids*, *29*(7), 2152–2164.